DESIGN OF ZINC OXIDE BASED SOLID-STATE EXCITONIC SOLAR CELL

WITH IMPROVED EFFICIENCY

A Dissertation

by

TAO-HUA LEE

Submitted to the Office of Graduate Studies of
Texas A&M University
in partial fulfillment of the requirements for the degree of

DOCTOR OF PHILOSOPHY

December 2011

Major Subject: Electrical Engineering

DESIGN OF ZINC OXIDE BASED SOLID-STATE EXCITONIC SOLAR CELL

WITH IMPROVED EFFICIENCY

A Dissertation

by

TAO-HUA LEE

Submitted to the Office of Graduate Studies of
Texas A&M University
in partial fulfillment of the requirements for the degree of

DOCTOR OF PHILOSOPHY

Approved by:

Co-Chairs of Committee,	Xing Cheng
	Jung-Jue Sue
Committee Members,	Kamran Entesari
	Chin B. Su
Head of Department,	Costas N. Georghiades

December 2011

Major Subject: Electrical Engineering

ABSTRACT

Design of Zinc Oxide Based Solid-State Excitonic Solar Cell with Improved Efficiency.

(December 2011)

Tao-Hua Lee, B.S., Iowa State University;

M.S., Iowa State University

Co-Chairs of Advisory Committee,   Dr. Xing Cheng
                                                        Dr. Hung-Jue Sue

Excitonic photovoltaic devices, including organic, hybrid organic/inorganic, and dye-sensitized solar cells, are attractive alternatives to conventional inorganic solar cells due to their potential for low cost and low temperature solution-based processing on flexible substrates in large scale. Though encouraging, they are currently limited by the efficiency from not yet optimized structural and material parameters and poor overall knowledge regarding the fundamental details. This dissertation aims to achieve improved performance of hybrid solar cells by enhancing material property and designing new device architecture.

The study begins with the addition of XD-grade single-walled carbon nanotube (XDSWNT) into poly(3-hexylthiophene) (P3HT) to improve the current density. By having a weight ratio of XDSWNT and P3HT equaled to 0.1:1, short-circuit current was quadrupled from 0.12 mA cm^{-2} to 0.48 mA cm^{-2} and solar cell efficiency was tripled from 0.023% to 0.07%, compared to devices with pure P3HT as a hole transport material. Secondly, a significant improvement in device efficiency with 250 nm long ZnO nanorod arrays as photoanodes has been achieved by filling the interstitial voids of the

nanorod arrays with ZnO nanoparticles. The overall power conversion efficiency increased from 0.13% for a nanorod-only device to 0.34% for a device with combined nanoparticles and nanorod arrays. The higher device efficiency in solid-state DSSCs with hybrid nanorod/nanoparticle photoanodes is originated from both large surface area provided by nanoparticles for dye adsorption and efficient charge transport provided by the nanorod arrays to reduce the recombinations of photogenerated carriers. Followed by the novel layer-by-layer self-assembly deposition process, the hybrid photoanode study was extended to the longer ZnO nanorod arrays. The best performance, 0.64%, was achieved when the thickness of the photoanodes equaled to 1.2 μm. Finally, the photovoltaic devices were modified by adding ZnO nanoarpticles into P3HT to increase interfacial area between ZnO and P3HT. The efficiency was enhanced from 0.18% to 0.45% when the ZnO nanorod arrays were 625 nm in length. Our successful design of the device morphology significantly contributes to the performance of solid-state hybrid solar cells.

DEDICATION

To My Parents, and Brother

ACKNOWLEDGEMENTS

TABLE OF CONTENTS

Page

LIST OF FIGURES

FIGURE   Page

LIST OF TABLES

1. INTRODUCTION

1.1 Overview

The rapidly increasing fossil fuel consumption and excessive greenhouse gas emissions have put significant pressure on the already-exhaustive global energy demand and needs for environmental protection. The global growing demand for energy and for protecting our environment can potentially be met by solar cell technology. Although the solar cell technology has not yet been in large-scale utilization because of its high cost and insufficient conversion efficiencies in the past, recent advances in nanomaterial and device technologies have offered new opportunities for it to become competitive to fossil fuels. Among various photovoltaic devices, the excitonic solar cells (XSCs) technology has made enormous progresses and is highly competitive for large scale commercial fabrication. The aim of the research on XSCs is to develop photovoltaic technology which allows solar cells to be produced on flexible substrate by using high throughput roll-to-roll method at low cost. Ideally, all of the fabrication process could be done using low-temperature, low power-consumption, low cost, and solution-based process.

This dissertation follows the style of *Nanotechnology*.

In XSCs, conjugated polymers, small molecules, or quantum dots are utilized as the light absorbing materials. Upon light absorption, excitons (bound electron-hole pairs) are generated. If they are not formed at the interface between constituent semiconductors, it is necessary for these excitons to diffuse to the interface without recombination. So long as the offset of energy levels at the junction is greater than the exciton binding energy, free charge carriers can be created [1-3]. For this reason, the majority of the carriers are present at the interface and the interfacial property becomes crucial. In addition, exciton diffusion length also has a significant impact on the performance of XSCs. Only those excitons generated within the order of the exciton diffusion length from the interface have chances to reach interface and separate into free charges. In other words, it is beneficial to fabricate excitonic devices with interface everywhere in the material. For conductive polymers, diffusion length ranges from 4 nm to 20 nm [4]; for high quality small molecule thin films, it's up to a micrometer [5]. Oppositely, in conventional photovoltaic devices, free electron-hole pairs are produced everywhere in the bulk semiconductor, and subsequently separate when they arrive at the junction. Therefore, the charge generation and separation are different between XSCs and conventional solar cells and result in fundamental difference in device behavior.

Excitonic photovoltaic devices include organic solar cells (OSCs), hybrid organic/inorganic solar cells (HSCs), and dye-sensitized solar cells (DSSCs). The most efficient XSCs reported are Grätzel's DSSCs with efficiencies of 11% [6-8]. Despite the high efficiency, DSSCs based on liquid electrolyte have reliability issues caused by the liquid redox electrolyte. Device instability and the need for good device packaging have

become major hurdles for commercial application of DSSCs [9]. Furthermore, liquid electrolyte based solar cells cannot be easily fabricated into multi-cell modules [10]. One way to address this manufacturing difficulty is to replace the liquid redox electrolyte by a solid-state hole transport material, typically a p-type conjugated polymer. Recently, many attempts have been made by using different hole transport materials, such as OMeTAD [11, 12], and poly(3-hexylthiophene) (P3HT) [13], along with dye-loaded porous nanoparticle films. Efficiencies of solid-state DSSCs remain around 4% [12, 14]. Recent progresses in nanotechnologies have led to improved efficiency in OSCs from planar p-n junction cells to bulk heterojunction cells with efficiencies up to 5-7% [15-18].

By modifying the morphology of inorganic constituent in HSCs and DSSCs, the photovoltaic efficiency could be improved. As the key components, many inorganic semiconductors have been applied as nanostructured materials for XSCs, such as TiO_2 [8, 11], ZnO [19-22], CdSe [23], PbS [24, 25], $CuInSe_2$ [26], and many others. Among these electron transport materials, ZnO is an attractive candidate because of its diverse morphologies. ZnO is a II-VI binary compound semiconductor with a large band gap of 3.2 eV, and the conduction band edge of ZnO is at -4.4 V versus vacuum [19]. As a direct and wide band gap material, it draws a lot of interests as the candidate for electronic and short wavelength optoelectronic applications. ZnO has a diverse group of nanostructures, for instance, nanoparticles [27], nanorods [28], vertically aligned nanorods/nanowires [29, 30], core-shell nanorods/nanowires [31, 32], nanotubes [33], nenobelts [34], nanosheets [35], nanoflowers [36], hierarchical structures [21], and branched structures [20]. These nanostructures can be synthesized through sol-gel

synthesis [27, 28], hydrothermal growth [29, 30], chemical bath deposition (CBD) [32], atomic layer deposition (ALD) [31], vapour-liquid-solid (VLS) approach [34], or metal-organic chemical vapor deposition (MOCVD) [20]. The reduction of the structures to nanoscale provides novel electrical, mechanical, and optical properties as the result of surface and quantum confinement effects [37]. Though power conversion efficiency of solar cells based on ZnO is lower than that of TiO_2, ZnO is still regarded as a prominent competitor due to its ease of synthesis and flexibility on the nanostructure morphologies. In addition, the electron mobility of ZnO is higher than that of TiO_2, the charge recombination rate of ZnO is lower than that of TiO_2, and the electron lifetime of ZnO is longer than that of TiO_2 [38, 39]. Those characteristics are beneficial for solar cell applications.

1.2 Organization of the dissertation

This dissertation aims to achieve improved performance of hybrid solar cells by enhancing material property and designing new device architecture. A comprehensive literature review on the recent progresses of ZnO based solid-state XSCs will be given first. One of the major research subjects in this study is to improve hole transporting capability of conjugated polymers. Thus solid-state DSSCs consisting of dye-coated ZnO nanoparticle photoanode and P3HT thin film were fabricated with addition of XD-grade single-walled carbon nanotube (XDSWNT) into P3HT. The amount of the XDSWNT in P3HT and the device performance of the cells were investigated. With the addition of XDSWNT, current density was improved by four times.

Another major research topic is to investigate the relationship between the photoanode morphology and the solar cell performance. Solid-state DSSCs were produced by using ZnO nanoparticles to fill the interstitial voids between ZnO nanorod arrays as the photoanode, hoping to further improve the efficiency of the solid-state DSSC device. The ZnO nanorod arrays serve as direct pathways for fast electron transport and the ZnO nanoparticles filled in the interstitial space of the ZnO nanorods offer a large surface area for dye adsorption. Using this hybrid nanorod-nanoparticle structure, a significant improvement in performance has been achieved. The effects of the ZnO photoanode morphology on the solid-state DSSC's performance are discussed.

The study was then extended to explore the influence of the length of ZnO nanorods on the photovoltaic performance. Solid-state DSSCs were fabricated by filling ZnO nanoparticles into the interstitial space between nanorod arrays from a novel layer-by-layer deposition method. The layer-by-layer deposition technique solves the issue of incomplete filling of deep ZnO nanorod arrays with random orientations, while at the same time provides uniform dye loading throughout the ZnO nanoparticle film.

Lastly, ZnO nanorod arrray/bulk heterojunction solar cells were fabricated at two different nanorod array lengths. The strategy is to use ZnO nanoparticles instead of PCBM due to the ease of ZnO synthesis and also its flexibility on morphology. The current density was significantly increased by using ZnO nanorod arrays and P3HT:ZnO NPs bulk heterojunction together instead of ZnO nanorod arrays and pure P3HT only. It is also been observed that with longer ZnO nanorods, the current density is also enhanced.

2. LITERATURE REVIEW

Many approaches have been explored to investigate and promote device performance of solid-state XSCs. Many of these aim to create large interfacial area between p-type and n-type materials by creating bulk heterojunction structure. In addition, bulk heterojunction structure ensures short exciton diffusion ranges and offers percolation pathways for both electrons and holes to reach relevant electrodes. Morphologies of active layers can be divided into four categories (**Figure 1**):

- Planar metal oxide and conjugated polymer bilayer;

- Filling nanoporous metal oxides with conjugated polymers;

- Metal oxide nanoparticles and conjugated polymer hybrid solar cells, including in-situ growth of metal oxides;

- Vertically-aligned metal oxide nanostructures with conjugated polymers.

In the following sections, a comprehensive review of the solid-state XSCs based on ZnO will be discussed. An attempt has been made to collect solar cell performance reported in the scope of this dissertation (**Table 1**).
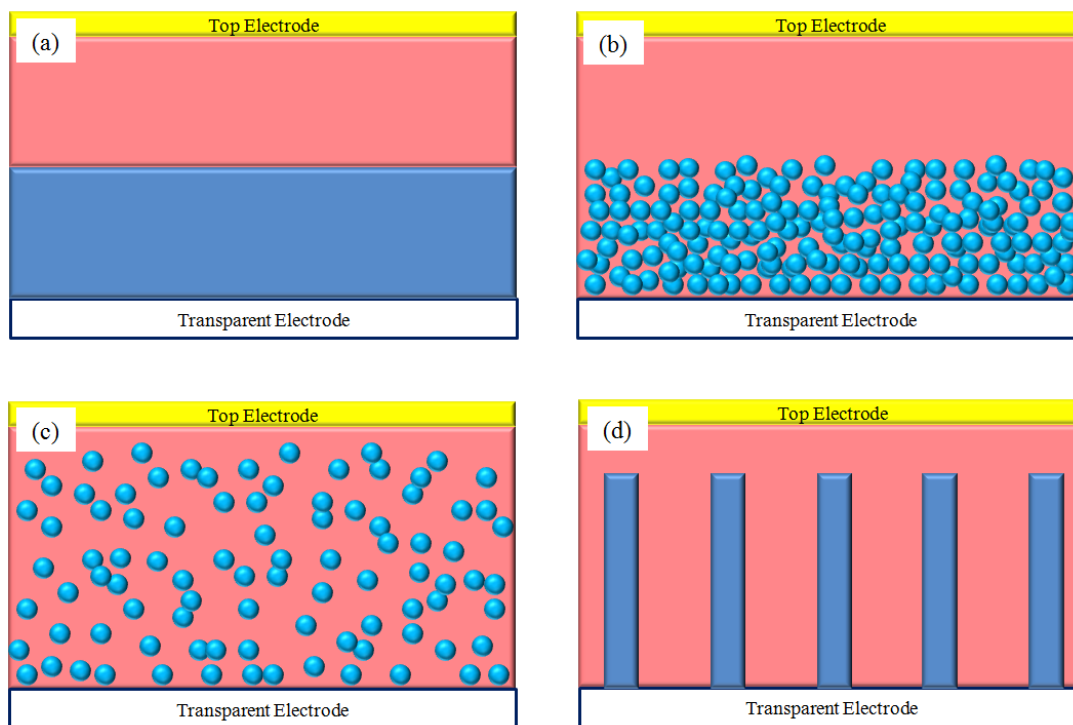
Figure 1. Four morphologies of active layers: (a) planar metal oxide and conjugated polymer bilayer; (b) filling nanoporous metal oxides with conjugated polymers; (c) metal oxide nanoparticles and conjugated polymer hybrid solar cells, including in-situ growth of metal oxides; (d) vertically-aligned metal oxide nanostructures with conjugated polymers.

2.1 Determination of solar cell performance

Before starting the discussion on solar cell performance, several terms used in the field are needed to be introduced briefly. **Figure 2** shows the typical current density-voltage (J-V) curve of solar cells with open-circuit voltage (V_{oc}), and short-circuit current (J_{sc}). Ideally the open-circuit voltage is determined by the difference between highest occupied molecular orbital (HOMO) level of the electron donor and

conduction band of the electron acceptor. Maximum theoretical current density that can be generated from a photovoltaic device is related to the bandgap of the light absorbing material in the system. Efficiency (η) of solar cells is calculated as (V_{mp} x J_{mp} / P_o) x 100%, where V_{mp} is the voltage at maximum output power, J_{mp} is the current at maximum output power, and P_o is the incident optical power. Fill factor (FF) is also an important indication used in solar cell area, which is defined as (V_{mp} x J_{mp}) / (V_{oc} x J_{sc}) x 100%. In general, the J-V curve is measured under air mass 1.5 (AM 1.5) condition with incident light power equals to 100 mW cm^{-2}. The 1.5 here corresponds to the solar zenith angle of 48 °. The angle is chosen because the solar cell development is concentrated in mid-latitude countries, such as the United States, Europe and Japan.
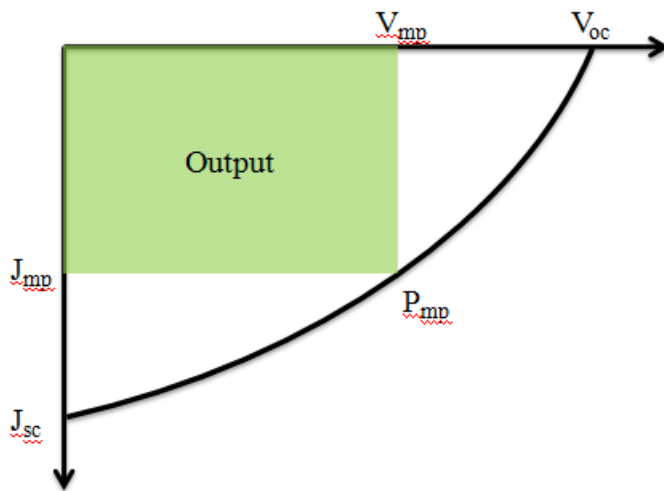
Figure 2. A typical J-V curve of solar cells.

Table 1. Performance of ZnO based solid-state XSCs. (NP= nanoparticle, NR= nanorod, NW= nanowire.)

Cell configuration	J_{sc} (mA cm^{-2})	V_{oc} (V)	FF	η (%)	Power Intensity (mW cm^{-2})	Ref
Bilayer						
ITO/ZnO/MEH-PPV/Ag	0.11	0.39	0.37	0.016	100	[40]
ITO/50-80 nm Zn$_{1-x}$Mg$_x$O/200 nm P3HT/Ag, x=0.25	1.27	0.70	0.56	0.49	100	[41]
ITO/ ZnO/80 nm P3HT/Ag	0.28	0.31	0.43	0.037	100	[42]
ITO/ Alkanethiol-modified ZnO/80 nm P3HT/Ag	0.42	0.31	0.40	0.053	100	[42]
ITO/30-50 nm ZnO/P3HT/Au	0.31	0.32	0.42	0.04	100	[43]
Porous film						
ITO/30-50 nm dense ZnO/150-300 nm porous ZnO/P3HT/Au	2.18	0.36	0.44	0.35	100	[43]
FTO/dense ZnO/800 nm porous ZnO/N719/spiro-OMeTAD/Au	2.05	0.535	0.46	0.50	100	[44]
Hybrid						
ITO/PEDOT:PSS/80 nm ZnO NP (67 wt%):MDMO-PPV/Al	2.40	0.814	0.59	1.6	71	[19]
ITO/PEDOT:PSS/80 nm ZnO NP (26 vol%):MDMO-PPV/Al	3.90	0.80	0.50	1.56	50	[45]
ITO/PEDOT:PSS/200 nm ZnO NP (26 vol%):P3HT/Al	2.19	0.69	0.55	0.92	75	[46]
ITO/PEDOT:PSS/ ZnO NP (67 wt%):APFO-3/Al	3.1	0.510	0.36	0.45	100	[47]

Table 1. Continued.

Cell configuration	J_{sc} (mA cm^{-2})	V_{oc} (V)	FF	η (%)	Power Intensity (mW cm^{-2})	Ref
Hybrid						
ITO/PEDOT:PSS/ ZnO NP (67 wt%):APFO-3/Al	0.415	0.475	0.510	0.210	50	[48]
ITO/PEDOT:PSS/ 225 nm ZnO NP (50 wt%):P3HT/Al	5.2	0.75	0.52	2.0	100	[49]
ITO/PEDOT:PSS/ ZnO NP (70 wt%):P3HT/Al	0.16	0.32	0.39	-	100	[50]
ITO/PEDOT:PSS/ ZnO NR (70 wt%):P3HT/Al	0.40	0.22	0.41	-	100	[50]
ITO/PEDOT:PSS/100 nm thick ZnO NP (15 vol%):MDMO-PPV/Al	2.3	1.14	0.42	1.1	100	[51]
ITO/PEDOT:PSS/96 nm thick ZnO NP (15 vol%):MDMO-PPV/Al	2.0	0.73	1.03	-	80	[52]
ITO/PEDOT:PSS/102 nm thick ZnO NP (15 vol%):P3HT/Al	3.5	0.83	0.50	1.4	100	[52]
Vertically aligned nanostucture						
ITO/300 nm ZnO NR/200 nm P3HT/Ag	2.2	0.44	0.56	0.53	100	[22]
ITO/180 nm ZnO NR/P3HT/PEDOT:PSS/Au	0.30	0.34	0.40	0.04	100	[53]
ITO/180 nm ZnO NR/Mercurochrome/P3HT/PEDOT:PSS/Au	0.87	0.45	0.41	0.16	100	[53]
ITO/550 nm ZnO NR/Z907 dye/P3HT/PEDOT:PSS/Au	2	-	-	0.20	100	[54]
ITO/550 nm ZnO NR/Z907 dye/P3HT/PEDOT:PSS/Au	1.73	0.30	0.389	0.20	100	[55]

Table 1. Continued.

Cell configuration	J_{sc} (mA cm^{-2})	V_{oc} (V)	FF	η (%)	Power Intensity (mW cm^{-2})	Ref
Vertically aligned nanostucture						
ITO/550 nm ZnO NR/Z907 dye/TPD(4M)-MEH-M3EH-PPV/PEDOT:PSS/Au	-	-	-	0.15	100	[55]
ITO/200 nm ZnO NR/P3HT/Ag	1.33	0.443	0.484	0.28	100	[56]
ITO/200 nm ZnO NR/P3HT/Ag	1.24	0.438	0.47	0.25	100	[57]
PET/SWNT/300-400 nm ZnO NW/P3HT/Au	-	0.46	-	0.6	100	[58]
ITO/180 nm ZnO NR/P3HT/Ag	1.37	0.45	0.49	0.30	100	[59]
ITO/380 nm ZnO NR/P3HT/Ag	1.64	0.30	0.48	0.24	100	[59]
ITO/300 nm ZnO NR/P3HT/Ag	2.91	0.38	0.50	0.55	100	[59]
Al/a discrete ZnO NR/P3HT/Au	0.32	0.40	0.28	0.036	100	[60]
Al/a discrete ZnO NR/QT/Au	0.29	0.35	0.32	0.033	100	[60]
ITO/300 nm ZnO NR/200 nm P3HT:PCBM/Ag	10.0	0.475	0.43	2.0	100	[22]
ITO/300 nm ZnO NR/P3HT:PCBM/Ag	9.6	0.57	0.50	2.7	100	[61]
ITO/ZnO NP/P3HT:PCBM/Ag	6.22	0.43	0.38	1.0	100	[62]
ITO/ZnO NP/P3HT:PCBM/VO$_x$/Ag	10.64	0.57	0.50	3.0	100	[62]
ITO/115nm ZnO NR/P3HT:PCBM/VO$_x$/Ag	-	-	0.65	3.9	100	[62]
ITO/180 nm ZnO NR/P3HT:TiO$_2$/PEDOT:PSS/Au	1.96	0.38	0.40	0.30	100	[53]
ITO/180 nm ZnO NR/Mercurochrome:TiO$_2$//P3HT/PEDOT:PSS/Au	2.45	0.46	0.46	0.52	100	[53]

2.2 Planar metal oxide and conjugated polymer bilayers

Covering a compact and planar layer of semiconductor oxide as ZnO with a thin layer of polymer is the most direct and simplest method to fabricate HSCs. The advantage of the device architecture is that photogenerated charges can be collected by the electrodes easily due to direct pathways. Oppositely, the relatively small interfacial area between metal oxide and polymer limits the charge carrier generation, especially the exciton diffusion length of conjugated polymers lies between 4-20 nm [4]. Though the efficiency of bilayer solar cells is limited, it is of considerable interest for studying fundamental scientific issues, for example, carrier generation, exciton diffusion length, and interface processes. In addition, the efficiency of bilayer structure can still be optimized by adjusting several parameters. Olson *et al.* reported a simple method to systematically tune the band offset in a metal oxide/conjugated polymer hybrid system in order to maximize the V_{oc} [41]. The band offset between conduction band of ZnO and LUMO level of conjugated polymer, poly(3-hexylthiophene) (P3HT), is reduced with the substitution of magnesium into ZnO and form $Zn_{1-x}Mg_xO$. The V_{oc} increased from 0.5 V at x=0 to more than 0.9 V at x=0.35. Efficiency increased as x increases from 0 to 0.25 with maximum efficiency of 0.49%, J_{sc}= 1.27 mA cm^{-2}, V_{oc}= 0.70 V, and FF= 0.56. To enhance J_{sc} in ZnO/P3HT bilayer structure, Hsu *et al.* modified ZnO surface with alkanethiol self-assembled monolayers (SAMs) [42]. Before modification, J_{sc} = 0.28 mA cm^{-2}, V_{oc}= 0.305 V, FF= 0.427, and η= 0.037%; with modification, J_{sc} increased to 0.42 mA cm^{-2}, V_{oc}= 0.312 V, FF= 0.404, and η= 0.053%. The enhancement on photocurrent attributes to the enhancement of the P3HT crystallinity. Alkanethiol SAMs reduce the

ZnO surface energy dramatically, thus during annealing, P3HT polymers are more mobile on the modified ZnO surface and can rearrange to form larger crystallinity domains [63].

2.3 Filling nanoporous metal oxides with conjugated polymers

The interfacial surface area between p-type and n-type materials can be increased by replacing the compact metal film with a nanoporous one; the porous ZnO films made with spray pyrolysis or doctor blade method have the porosity around 50% [64-66]. By filling these interstitial voids of the porous film with a conjugated polymer, exciton harvesting is improved as more excitons are generated within 4-20 nm of the ZnO/polymer interface, which is within the diffusion length of conjugated polymers. On the other hand, in order to generate carriers efficiently, the optimum pore size is constrained in the similar dimension. This requirement leads to the poor polymer infiltration into porous metal oxide films, reduces the real interfacial surface area between p-type and n-type materials, and is responsible for the low reported efficiencies [67-69]. Therefore, nanostructure pore size and distribution are needed to be refined to harvest more excitons. Boucle *et al.* reported that the device performance is strongly influenced by the shape and size of the initial ZnO nanocrystallites used to deposit the porous ZnO films [43]. The best performance in their porous ZnO/P3HT system came from 8 x 13 nm nanorods as the initial ZnO nanocrystallites with J_{sc}= 2.18 mA cm^{-2}, V_{oc}= 0.36 V, FF= 0.44, and η= 0.35%. The other three initial nanocrystallites used were 5 nm nanoparticles, 24 nm nanoparticles, and 14 x 55 nm nanorods; the worst

performance came from 14 x 55 nm nanorods. This illustrates that fine control of the morphology of the staring ZnO nanocrystals leads to the different nanostructure pore size of the porous nanocrystalline film and can effectively tune the performance of the solar cells.

Moreover, it's logical to introduce solid-state DSSCs here. With dyes as the interface modifiers between ZnO and conjugated polymer, the overall structure of the device keeps the same but dyes take care of the light absorption and semiconducting polymer deals with the hole transport. With appearance of the dyes, V_{oc} increases as a result of the suppression of charge recombination since dye molecules can be regarded as the physical barrier and can reduce the number of the shunt pathways between conductive polymer and ITO substrate caused from the defects in the ZnO. J_{sc} of the cells can also be improved if amphiphilic dyes are used as surface modifiers [54]. With amphiphilic dyes as the surface modifier, ZnO surface is easier to be wetted by conjugated polymer and thus increase the interfacial area, exciton harvesting, and J_{sc}. Most recently, Boucharef et $al.$ reported that by optimization the sintering process, porous ZnO electrodes sensitized by N719 and infiltrated with the 2,2′,7,7′-tetrakis(N,N-di-pmethoxypheny-amine)-9,9′-spirobifluorene (spiro-OMeTAD) gives the efficiency of 0.50% [44].

2.4 Metal oxide nanoparticles and conjugated polymer hybrid solar cells

One way to avoid poor polymer infiltration into porous metal oxide films is to blend nanoparticles of inorganic semiconductors with conjugated polymers. Interfacial

surface area is therefore enlarged throughout the thin film by mixing p-type and n-type materials together. In addition, for solar cells based on bilayer structure and nanoporous films filled with conjugated polymer, ZnO or other inorganic semiconductors need to be grown or synthesized on the substrate before the layer of the conjugated polymer can be deposited. With the hybridization of the metal oxide nanoparticles and the conjugated polymer, the advantages from materials are combined. With the polymer as the matrix, simple, large-scale deposition techniques provide a versatile route toward hybrid solar cell devices [70]. Oppositely, the main challenge for bulk heterojunction photovoltaic devices is to create enough contacts between inorganic materials to maintain pathways for electrons. In other words, the most important factor which determines the device performance is the phase separation [49, 71]. In HSCs, charge generation requires a high interfacial surface area, while charge transport and collection requires the unhindered pathways in the individual component. The other challenge is that further modification on the metal oxide materials or conjugated polymers might be required in order to use a solvent to process both inorganic and organic materials at the same time.

Hybrid bulk heterojunction solar cells have been made by blending ZnO nanocrystals and the conjugated polymer, poly(2-methoxy-5-(3′-7′-dimethyloctyloxy) -1,4-phenylenevinylene) (MDMO-PPV). The thin films can be prepared by spin-coating a blended solution consisting of ZnO nanoparticles and MDMO-PPV from the common solvent, chlorobenzene/methenaol (v/v = 95:5). The device performance of the hybrid ZnO:MDMO-PPV solar cell with 67 wt% ZnO has been measured as J_{sc}= 2.40 mA cm^{-2}, V_{oc}= 0.814 V, FF= 0.59, and η= 1.6% under 0.71 sun [19]. P3HT is another conjugated

polymer of interest to be applied in ZnO/polymer conjugated solar cells due to its high hole mobility ~ 0.1 cm^2 V^{-1} s^1 [72]. The effect of the volume ratio of ZnO in the hybrid thin film affects the device performance significantly. The maximum performance was obtained with the devices containing 26-35 vol% ZnO [45]. Beek *et al.* investigated the impact of thermal annealing on the ZnO: P3HT solar cells. With thermal annealing, the performance of the cell was improved especially when the amount of ZnO is low, that is, the amount of polymer is high. This enhancement of the cell efficiency mainly comes from the increased J$_{sc}$, as a result of the enhanced crystallinity and higher hole mobility in P3HT phase. However, even optimized with thermal annealing with right ratio between ZnO and P3HT, the highest efficiency of ZnO:P3HT blended hybrid solar cell was 0.92% [46]. Compared to ZnO: P3HT samples, ZnO nanoparticles are well dispersed with smoother surface and smaller aggregates in ZnO: MDMO-PPV samples when the amount of ZnO is kept the same. Furthermore, with the increasing of ZnO amount in the ZnO: P3HT mixings, the surface roughness increases severely and the possibility to have shunt films increases. The roughness of ZnO: MDMO-PPV blends also increases with the amount of ZnO in the films, but in a less significant fashion. This enlarges the amount of ZnO which can be loaded in the blends and enhance the charge generation and separation. This is a possible explanation for the unexpected photovoltaic performance from the ZnO: P3HT devices [45]. With a fixed weight ratio between ZnO and P3HT as 1:1, Oosterhout *et al.* varied the thickness of the thin films from 50 nm to 250 nm and investigated the effect of the film thickness on the device performance [49]. A similar conclusion was made that the relatively poor performance of thin ZnO: P3HT

photovoltaic device is due to coarse phase separation. But for thicker films, charge generation is more efficient as a result of a more favorable phase separation. In order to improve the dispersion stability of ZnO nanoaparticles in the polymer, n‑propylamine was added into the blends as a stabilizing ligand. However, the residual ligands improve the film smoothness without enhancing the photovoltaic performance, which is due to the electron transfer over the interface between the inorganic nanoparticle and the polymer is hampered by the surfactants [45]. More detailed investigation on the surfactants used for improving ZnO dispersion in the polymers is reported by Rhodes *et al.* [73]. Other than MDMO-PPV and P3HT, Wong *et al.* reported the use of poly(2,7-(9,9-dioctylfluorene)-*alt*-5,5-(4′,7′-di-2-thienyl-2′,1′,3′-benzothiadiazole)) (APFO-3) as the conjugated polymer in ZnO: polymer blends [47]. The J_{sc}, V_{oc}, FF, and η for the device were 3.1 mA cm^{-2}, 0.510 V, 0.36, and 0.45%, in respect. The non-optimum morphology of the films limits the photovoltaic performance of the cell on the degree of exciton separation and charge transport. Recently, Han *et al.* investigated on a series of ZnO: poly (3-octylthiophene) (POT) hybrid devices with different proportions of ZnO with highest efficiency of 0.210% when the weight ratio of ZnO and POT is 2:1 [48]. The device performance of ZnO: P3HT hybrid solar cells based on different ZnO morphologies was reported [50]. With 70 wt% of ZnO in the blends, the efficiency of device based on ZnO nanorods is higher than that based on ZnO nanoparticles, which agrees with the results based on CdSe from Huynh *et al* [23].

The solar cell performance has been improved from bilayer structures to filling the pores in nanostructured metal oxide films to mix inorganic nanocrtystals with the

conjugated polymer, in consequence. However, even interfacial area between p-type and n-type materials has been enlarged by blending them together and forming the thin films, there are still challenges to create good dispersion of ZnO nanocrystals in the polymer matrix. The relatively low amount of inorganic nanocrystals in the polymer not only lowers the charge carrier generation but also makes it difficult to form percolation pathways for electrons; therefore the achievable performance is limited. To overcome the disadvantages, the use of a precursor of the metal oxide and convert the precursor into inorganic nanocrystals directly in the polymer film is introduced [74]. This method differs from the previous approaches that the inorganic nanocrystals are made after film formation, not before film formation; thus the intimate mixing is ensured. The challenge is still to control the morphology of the mixture, and the crystalline nature of the metal oxide phase after conversion. Furthermore, due to the nature of the conjugated polymer, not all inorganic semiconductors can be well converted from the precursor at low temperature.

Beek *et al.* first introduced in situ ZnO: conjugated polymer bulk heterojunction solar cells by spin-coating a solution containing the precursor of ZnO, diethylzinc, and MDMO-PPV as the active layer [51]. Followed by thermal annealing at appropriate temperature and humidity, a crystalline ZnO network is formed in the polymer phase. The device gave J_{sc}=2.3 mA cm^{-2}, V_{oc}=1.14 V, FF= 0.42, and η= 1.1%; without annealing, the ZnO:MDMO-PPV mixture only gave a poor photovoltaic effect as J_{sc}=0.05 mA cm^{-2}, V_{oc}=1.15 V, and FF= 0.18. The huge difference given from devices

before and after annealing shows the essential of the heat treatment and the importance of obtaining crystalline ZnO for high performance solar cells.

2.5 Vertically-aligned metal oxide nanostructures with conjugated polymers

Creating vertically-aligned metal oxide nanostructures with respect to the substrate is considered to be a potential approach to overcome the problems encountered in the nanoparticle-based hybrid solar cells described in previous sections. Ideally, vertically-aligned metal oxide nanostructures can be synthesized with optimized dimension which is small enough for most of the excitons to reach the junction between inorganic and organic components; at the same time, this small enough dimension does not hinder the filling of the polymer into the nanostructures. By controlling the dimension of the vertically-aligned nanostructure, polymer chains are also allowed to align themselves perpendicular to the substrate. The interchain coupling is thus improved and leads to better exciton diffusion and charge transport in polymer [72, 75, 76]. As for electrons, there is a more direct pathway to reach the electrode in nanorods than in porous nanoparticle thin films; in addition, nanorods provide fewer sites to trap electrons. With a more direct pathway and fewer trapping sites, electron transport in nanorods is tens to hundreds times faster than that in nanoparticle thin films [30, 39, 77]. Efficient electron transport helps minimize electron transit time from the point of generation to the electrode, thus lowering the recombination loss of electrons.

Starting from a nucleation layer of ZnO, Olson *et al.* have hydrothermally grown vertically aligned ZnO nanostructures on the ITO substrate [22]. A 200 nm layer of

P3HT was then spin-coated from solution on top of the ZnO nanofibers, followed by thermal annealing at 200°C for 1 min. The device was finalized with thermal evaporate a layer of Ag top electrode. The best performance based on this device structure gave the photovoltaic effect with J_{sc}= 2.2 mA cm^{-2}, V_{oc}= 440 mV, FF= 0.56, and η=0.53%. Ravirajan *et al.* have studied charge recombination behavior and device performance of devices with different ZnO nanostructures and found charge recombination in cells based ZnO nanorods is over 2 orders of magnitude slower than cells based on ZnO nanoparticles [54]. An amphiphilic dye layer was applied between the ZnO nanostructure and P3HT to optimize interfacial electron transfer and improve the wetting of the ZnO surface by the polymer. The best efficiency based on ITO/ZnO NR/Z907 dye/P3HT/PEDOT:PSS/Au was 0.20% with J_{sc}= 2 mA cm^{-2}. Lin *et al.* applied a different dye layer, mercurochrome ($C_{20}H_8Br_2HgNa_2O$), to coat ZnO nanorods and the results agreed with Ravirajan *et al.* that the efficiency of ZnO NR/P3HT solar cell increased from 0.04% to 0.16% with the mercurochrome on ZnO nanorod surface [53]. Peiro *et al.* compared the power conversion efficiencies of ZnO nanorod based solar cells with two different polymers, P3HT and poly[(1,4-phenylene-(4-methylphenyl)amino-4,4′-diphenylene-(4-methylphenyl)amino-1,4-phenylene-ethenylene-2-methoxy-5-(2-ethylhexyloxy)-1,4-phenylene-ethenylene)-co-(2,5-dimethoxy-1,4-phenylene-ethenylene-2-methoxy-5-(2-ethylhexyloxy)-1,4-phenylene-ethenylene)] (TPD(4M)-MEH-M3EH-PPV) [55]. The efficiencies were 0.20% and 0.15%, respectively. Olson *et al.* have extended the study to device processing parameters [56]. It is reported that thermal annealing condition affects

the device performance. The ZnO NR/P3HT device without annealing gave an efficiency of 0.23%; with thermal annealing at 150°C, device efficiency increased to 0.25%; with 225°C annealing, efficiency was further improved to 0.28% with J_{sc}= 1.33 mA cm^{-2}, V_{oc}= 443 mV, and FF= 0.484. It is also reported that the selection of solvent for P3HT has a significant impact on filtration of the polymer into interstitial space between ZnO nanorods, thus the selection of solvent also influences the performance of the device. By using 1, 2-dichlorobeneze as the solvent without thermal annealing, the device had an efficiency of 0.23%. Under the same condition, efficiency of the device was only 0.17% while using chloroform as the solvent for P3HT. Instead of using rigid ITO glass as the substrate, Unalan *et al.* fabricated ZnO NW/P3HT solar cells on the flexible polyethylene terephthalate (PET) substrate with single walled carbon nanotubes (SWNTs) as electrode and achieved an efficiency of 0.6% [58]. Lee *et al.* measured the surface area of ZnO nanorod with different lengths from 80 nm to 380 nm and quantified the effect of the surface area on the ZnO NR/P3HT devices [59]. It is found that the surface area of ZnO nanorod is linearly proportional to the average length. Thus longer nanorods provide more interfacial area and generally improve performance though the increase in J_{sc} was lower than expected due to incomplete infiltration of P3HT into longer ZnO nanorod arrays and longer distance from the top contact to the P3HT infiltrated into the ZnO nanorod arrays. It is also showed that a subtle difference in the ZnO nanostructure morphology can impact the crystallinity of P3HT and enhance photocurrent. The best device performance was achieved with J_{sc}= 2.91 mA cm^{-2}, V_{oc}= 0.38 V, FF= 0.50, and η= 0.55%. In order to have an improved understanding of the

ZnO/polymer interface, Briseno *et al.* demonstrated basic operation of devices based on single ZnO nanowire wrapped by end-functionalized conjugated polymer [60]. The single nanowire/P3HT device yielded a J_{sc} of ~ 0.32 mA cm^{-2}, V_{oc} ~ 0.40 V, FF~ 0.28, and an efficiency of ~ 0.036% with P3HT thicknesses ranging from 7 to 20 nm. This suggests that when the thickness of P3HT is similar to its own exciton diffusion length, the performance of the nanowire device will not be influenced significantly.

The reported photovoltaic performances of ZnO NR/conjugated polymer (P3HT) cells were not as good as expected. One of the possible reasons is that the electron mobility of the ZnO nanorods is too high, therefore, leads to the excess charge recombination at the ZnO/conjugated polymer interface. Another possible reason could be because the spacing between ZnO nanorods is on the order of 100 nm and therefore larger than the exciton diffusion length of conjugated polymer [22]. In order to overcome the large spacing between ZnO nanorods and dissociate more photogenerated excitons, Olson *et al.* combined PCBM into P3HT. The efficiency of the cell based on ZnO NR and PCBM: P3HT blend was 2.0% with J_{sc}= 10.0 mA cm^{-2}, V_{oc}= 475 mV, and FF= 0.43 [22]. J_{sc} was increased significantly compared to the device with neat P3HT since excitons can be generated not only at the interface between P3HT and ZnO but also at the interface between P3HT and PCBM. With addition of PCBM into P3HT, the large spacing between ZnO nanorods has been overcome; in addition, electrons transfer from PCBM to ZnO efficiently. However, it should be noticed that in this photovoltaic cell configuration, the major active layer is P3HT: PCBM blend. Most of the carriers are generated at the interface between P3HT and PCBM due to the much larger interface

between them. Other than an electron acceptor, the main function of ZnO nanorod is an electron collector and transporter. This conclusion is agreed by Takanezawa *et al.* by studying the dependence of the device performance on the ZnO nanorod length [61]. ZnO NR/P3HT and ZnO NR/P3HT: PCBM cells were fabricated with different ZnO nanorod length from 0 nm to 250 nm. The J_{sc} of device without PCBM increased from 0.17 to 1.2 mA cm^{-2} linearly, while J_{sc} of devices with PCBM remained constant at around 7.5 mA cm^{-2}.   The performance of the best device without ZnO nanorod yielded a J_{sc} of 9.0 mA cm^{-2}, V_{oc} of 0.52 V, FF of 0.38, and an efficiency of 1.8%; the thickness of active layer is about 450 nm. With the appearance of 300 nm long ZnO nanorods, the efficiency was significantly improved to 2.7% with J_{sc}= 9.6 mA cm^{-2}, V_{oc}= 0.57 V, and FF= 0.50. The improved performance supports that ZnO nanorods work as efficient carrier transport path.

3. SOLID-STATE DYE-SENSITIZED SOLAR CELL BASED ON

SEMICONDUCTING NANOMATERIALS

3.1 Introduction

Dye-sensitized solar cell (DSSC) has become an emerging competitor for commercial applications in solar energy harvesting since its invention [8]. The energy conversion efficiency of DSSC can be greater than 10% [78, 79] while its cost is much lower than other photovoltaic technologies due to its low material cost, simple fabrication and ease of scaling up for large area production. However, the prospect of using DSSC for long-term energy harvesting is uncertain mainly due to suspect reliability issues caused by the TiO_2 layer and the liquid redox electrolyte. The strong photocatalytic property of TiO_2 can cause accelerated degradation of dye molecules. With liquid electrolyte, the device stability and the device packaging become major issues for commercial application [9]. In addition, liquid electrolyte makes it difficult to fabricate multi-cell modules [10]. One way to solve this problem is to replace the liquid redox electrolyte by a solid-state p-type semiconductor (SSDSSC). Recently, many attempts have been made by using different hole transport materials: OMeTAD [11, 12], pentacene [80], TPD [81], polythiophene [82], polyaniline [83] and polypyrrole [84].

In this work, we present a SSDSSC device consisting of zinc oxide nanoparticles and poly(3-hexylthiophene) (P3HT) thin film. Specifically, the device is composed of a thin film of ZnO nanoparticles which functions as electron transport material. The ZnO nanoparticles are further coated with light-absorbing dyes to extend light absorption

range from UV range to visible light range. A p-type semiconducting polymer film based on P3HT or P3HT doped with XD-grade singled-walled carbon nanotube (XDSWNT) is then deposited on top of the dye molecules to replenish lost electrons in dye molecules after light absorption and charge transfer.

3.2 Experimental details

3.2.1 ZnO nanoparticle preparation

Colloidal ZnO nanoparticles were prepared by hydrolyzation process. This method has been previously reported elsewhere, only a brief summary is given here [13]. Sixteen mmol of KOH (99.99%, Sigma-Aldrich) was dissolved in 150 ml methanol at $60^{o}C$ with refluxing and stirring for 5 min, followed by addition of 8 mmol of zinc acetate dihydrate $(Zn(Ac)_2 \cdot 2H_2O)$ (99%, Fluka) in 50 ml methanol. This mixture was refluxed and stirred at $60^{o}C$ for 2 hours. The ZnO colloids were then concentrated from 200 ml to 20 ml at $60^{o}C$ by rotary evaporation under vacuum. TEM image shows the average particle size is 5 nm [85].

3.2.2 Device preparation

Fluorine-doped SnO_2 glass (resistivity=$15\Omega/\square$, Solaronix) was cleaned by acetone and isopropyl alcohol (IPA), and then placed in a glass container (100 ml, Pyrex). White ZnO nanoparticles were precipitated after adding methanol, hexane, and IPA at a volume ratio of 1:5:1 into the concentrated ZnO methanol suspension. In order to form a 10-μm thick film, the volume of ZnO methanol suspension was chosen to be 1

ml from previous experiments. The mixture was then kept at 60°C overnight until the ZnO nanoparticles were fully precipitated and settled on the SnO_2 glass. Once ZnO thin film was formed, the sample was taken out of the glass container and dried in air. **Figure 3** shows the SEM image of the ZnO thin film. The porosity of the film provides a large surface area for dye attachment.
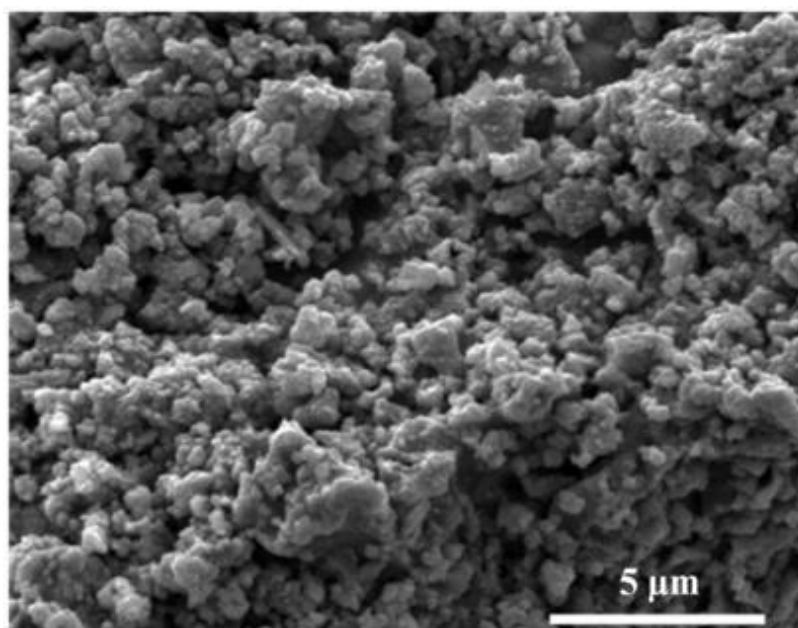
Figure 3. SEM image of ZnO thin film. (Courtesy of Xi Zhang.)

In order to remove residual solvents and residual acetates on ZnO surface, the film was annealed in air at 450°C for 1 hour. XPS spectra (Kratos Axis Ultra Imaging X-ray photoelectron spectrometer) were collected before and after film annealing to compare the impurity level. The binding energies were calibrated with respect to the signal for carbon (binding energy = 284.8 eV). **Figure 4(a)** shows the O1s peak before

and after 450°C annealing. The shoulder peak at about 530 eV is due to acetate impurity at the surface of ZnO nanoparticles. The peak at about 528.7 eV is due to the bonding of zinc and oxygen. After annealing, the peak that represents the acetate impurity dropped significantly (**Figure 4(b)**). The weight concentration of carbon was shown to decrease from 15% to 5% after annealing.

The dye used in this work was $RuL_2(NCS)_2$, L=2,2'-bibyridyl-4, 4'-dicarboxylic acid, also known as the N3 dye (Solaronix). ZnO films were soaked in 0.5mM of dye in ethanol at room temperature for different loading times. Then, the dye-adsorbed ZnO thin film was immersed in ethanol to remove excess dyes.

For optimal device performance, a monolayer of dye loading on ZnO surface is preferred. To determine the appropriate dye loading time, XPS spectra were acquired for samples after soaking ZnO films in dye solution for 5 min, 30 min, 2 h, and 24 h. XPS spectra were also collected for pristine ZnO film and pure N3 dye for comparison. For the 24-h dye-loading sample, the intensity of Zn2p peak dropped significantly. This indicates ZnO nanoparticles were wrapped by more than one layer of dyes. The C1s peak after 24-h dye loading closely resembles the pure N3 dye, which is consistent with Zn2p peak change. Similar trend was also observed in O1s peaks. In all spectra, the 30-min and 2-h dye loading samples show almost the same spectra and are clearly different from the 24-h dye-loading sample. The above finding suggests that a 30-min dye loading time is enough for having a monolayer of dyes adsorbed on the surface of the ZnO nanoparticles.
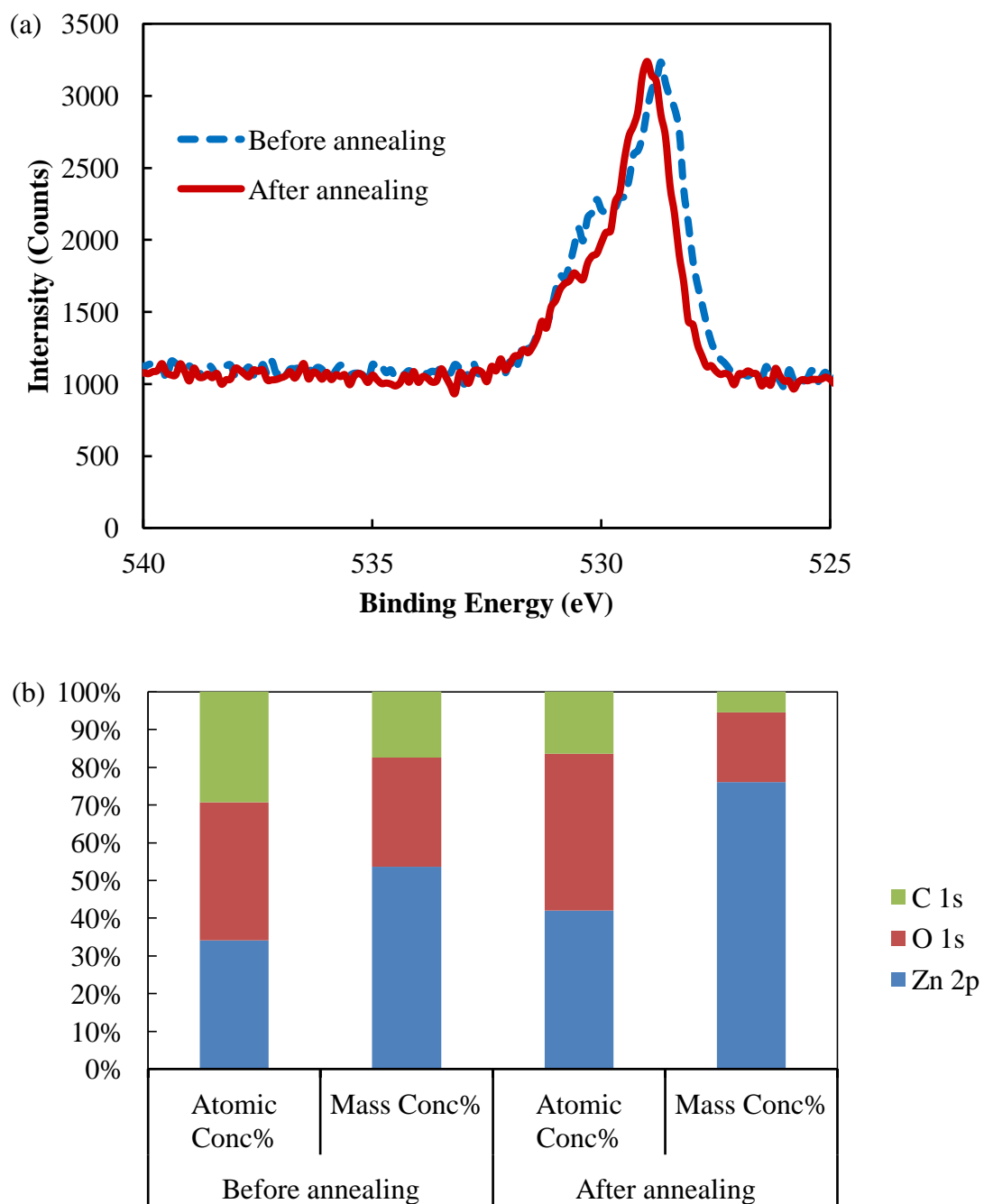
Figure 4. XPS spectra of ZnO thin film: (a) O1s peak of the thin film before and after 450°C annealing; (b) Quantification analysis of C1s, O1s and Zn2p peaks before and after annealing.
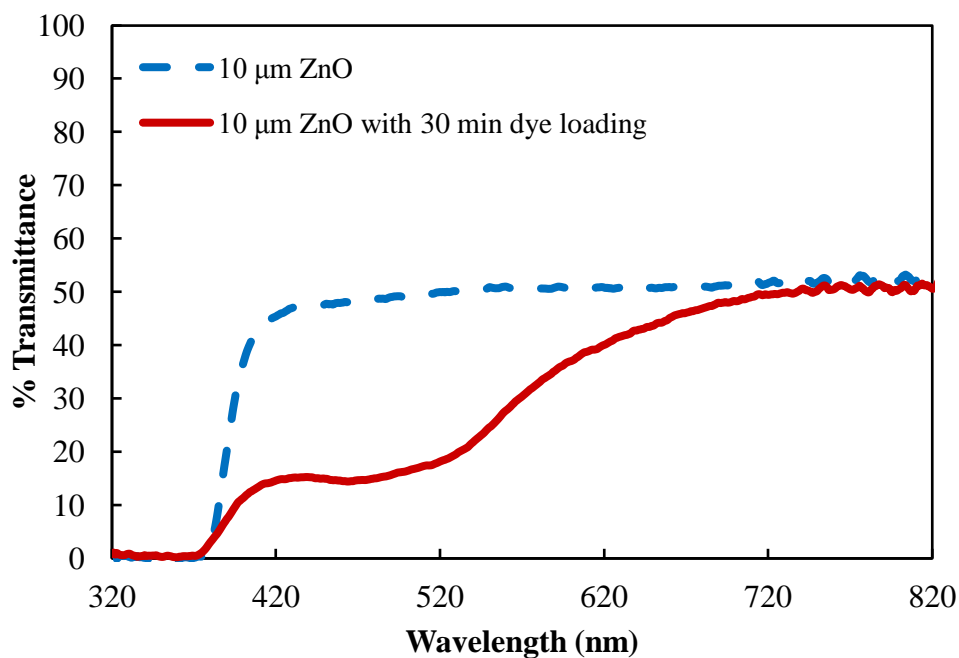
Figure 5. Transmittance spectra of ZnO film before and after 30 min dye loading.

To evaluate the light absorption of the ZnO thin film with 30-min of dye loading, UV-vis-NIR (Hitachi U-4100 UV-vis-NIR spectrophotometer) transmission spectrum was acquired. **Figure 5** shows the transmittance of a 10-μm thick ZnO thin film before and after 30 min of dye loading. The transmission for pure ZnO thin film is around 50% for the visible light. The low transmission in the visible wavelengths is due to the scattering of light by the ZnO nanoparticle aggregates. UV-vis-NIR absorption spectrum of dilute ZnO nanoparticle suspension indicates no absorption in the visible range. It is noteworthy to point out that the light scattering within ZnO film is beneficial for light trapping and absorption. With dye loading, 85% of visible light was absorbed by the film at 520 nm, which is the absorption peak of N3 dye.

Two sets of hole transport material systems were used. The first one is a commonly used p-type semiconducting polymer, poly(3-hexylthiophene) (M_w~64000, Sigma-Aldrich). P3HT was dissolved in 1,2-dichlorobenzene (99%, Sigma-Aldrich) with a concentration of 20 mg ml^{-1}. The second hole transport material was P3HT with addition of XDSWNT. Before mixing with P3HT in 1,2-dichlorobenzene, XDSWNTs were purified by sulfuric and nitric acid in a volume ratio of 3:1, filtered by distilled water, and kept in oven at 80°C until totally dried. The weight ratios of XDSWNT: P3HT were 1:1, 0.1:1, 0.01:1, and 0.001:1 with concentration of P3HT fixed at 20 mg ml^{-1} in 1,2-dicholorobenzene. From the particles on the sidewall of the glass vial, the sample with weight ratio of XDSWNT: P3HT = 1:1 was not fully wrapped by P3HT and was not fully dispersed in 1,2-dichlorobenzene, leading to visible aggregates. For the other three samples, there was no aggregation observed and good dispersion of XDSWNT in P3HT was achieved. P3HT solutions were then dropped on dye-coated ZnO film by volume-adjustable pipette and followed by annealing at specific temperature in vacuum oven for 2 h. To complete the device fabrication, a layer of 100-nm thick Au was thermally evaporated on top of the device through a shadow mask. The active area of the devices was 0.04 cm^2.

3.2.3 Solar cell characterization

To evaluate device performance, the fabricated SSDSSCs were illuminated by a standard solar simulator at AM 1.5G condition (100 mW cm^{-2}). The current density-voltage (J-V) characteristics were acquired by a Keithley 2400 sourcemeter

controlled by a Labview data acquisition program. The short-circuit current density, open-circuit voltage, and device efficiency were extracted from the J-V curves.

3.3 Results and discussion

3.3.1 Effect of P3HT thickness and annealing on device performance

P3HT is a p-type semiconducting polymer with a glass transition temperature (T_g) of around 130°C. The electrical and optical properties of P3HT film are determined by the internal polymer chain conformation. P3HT is a semicrystalline material and thermal annealing can increase the crystallinity of the P3HT thin films for better charge transport. In order to investigate the annealing temperature effect on solar cell efficiency, three different temperatures at below, around, and above T_g of P3HT, i.e., 150 ℃, 180 ℃, and 210 ℃ were chosen. The thickness of P3HT was fixed at 1.5 μm. All samples were annealed in vacuum oven for 2 h. A P3HT thin film was also dried in air for 1 day without annealing for comparison.

Figure 6 shows the measured J-V characteristics of the SSDSSCs. The sample without P3HT annealing was not stable due to residual solvent in P3HT film. For other samples, which were annealed at different temperature, 150°C annealing gave the best result. Then, both open-circuit voltage and short-circuit current decreased with increasing annealing temperature. The result obtained here is contradictory to our expectation, which may be related to interactions between ZnO, dye molecule and P3HT at elevated temperatures. The physical meaning of this unexpected trend is still under investigation.
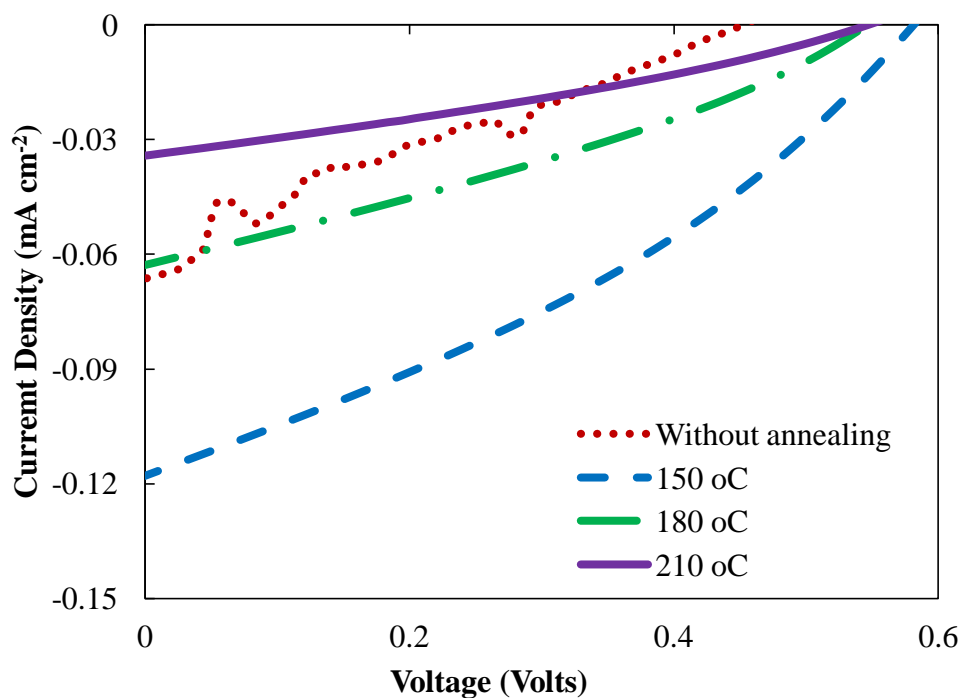
Figure 6. J-V characteristics of SSDSSCs with P3HT annealing temperature at 150°C, 180°C, 210°C.

The ZnO nanoparticle thin film is expected to exhibit a rough surface. To determine the surface roughness of the thin film, a laser confocal microscopy (Keyence VK-9700) was performed on the 10-μm ZnO thin film with 30 min of dye coating. The surface roughness (Ra) was found to be around 1 μm. In order to investigate how the surface roughness of the film affect solar cell efficiency, the J-V curves of four sets of samples with different P3HT thicknesses of 0.5 μm, 1 μm, 1.5 μm, and 2 μm were generated. All samples were annealed at 100°C for 2 h in vacuum oven after P3HT deposition.

Figure 7 shows the J-V curves of the solar cells with different P3HT thickness. Samples with 0.5 μm P3HT failed to work as a photovoltaic device due to internal short circuit. This is likely because gold electrode coating could make direct contact with ZnO if the thickness of P3HT cannot overcome the surface roughness of the ZnO thin film. For the other three samples with P3HT thicknesses of 1.0 μm, 1.5 μm and 2 μm, they gave similar open-circuit voltage and short-circuit current, but the 1.5 μm device has a better fill factor. This result may be explained by the low carrier mobility of P3HT. The carrier transit time and carrier trapping in the P3HT layer will increase when P3HT film becomes thicker. As a result, once the thickness of the hole transport material can compensate the surface roughness of the ZnO thin film, the thinner of the p-type material the better the solar cell will perform.

3.3.2 Effect of XDSWNT doping on device performance

Even though efforts were put on modifying the annealing temperature and varying the P3HT thickness, short-circuit current in all SSDSSC was still low. In order to improve charge transport and enhance short-circuit current, XDSWNTs were added into P3HT at a weight ratio of 1:1, 0.1:1, 0.01:1, and 0.001:1, respectively. **Figure 8(a)** shows the J-V curves for samples of different weight ratios. The sample with a weight ratio of XDSWNT: P3HT = 1:1 was short and cannot be used as a solar cell device. The amount of P3HT was not enough to wrap XDSWNTs by π-π bonding in this weight ratio and the high conductivity of XDSWNTs causes internal short circuit. For the other three samples, the amount of P3HT was enough to wrap all the XDSWNTs and showed no

short circuit. **Figure 8(b)** shows the trend lines of open-circuit voltage and short-circuit current as a function of the XDSWNT/P3HT weight ratio. The trend line shows that short-circuit current went higher with increasing XDSWNT content. By comparing between the neat P3HT to a weight ratio of XDSWNT: P3HT = 0.01:1, the short-circuit current increased by four times. At the same time, open-circuit voltage dropped around 24%.
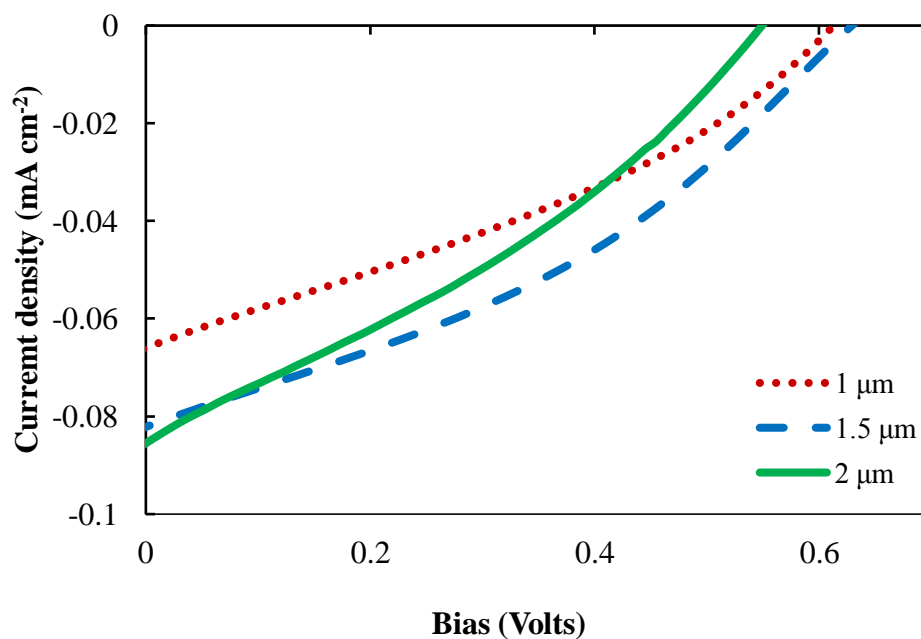
Figure 7. J-V characteristics of SSDSSCs with different P3HT thickness.
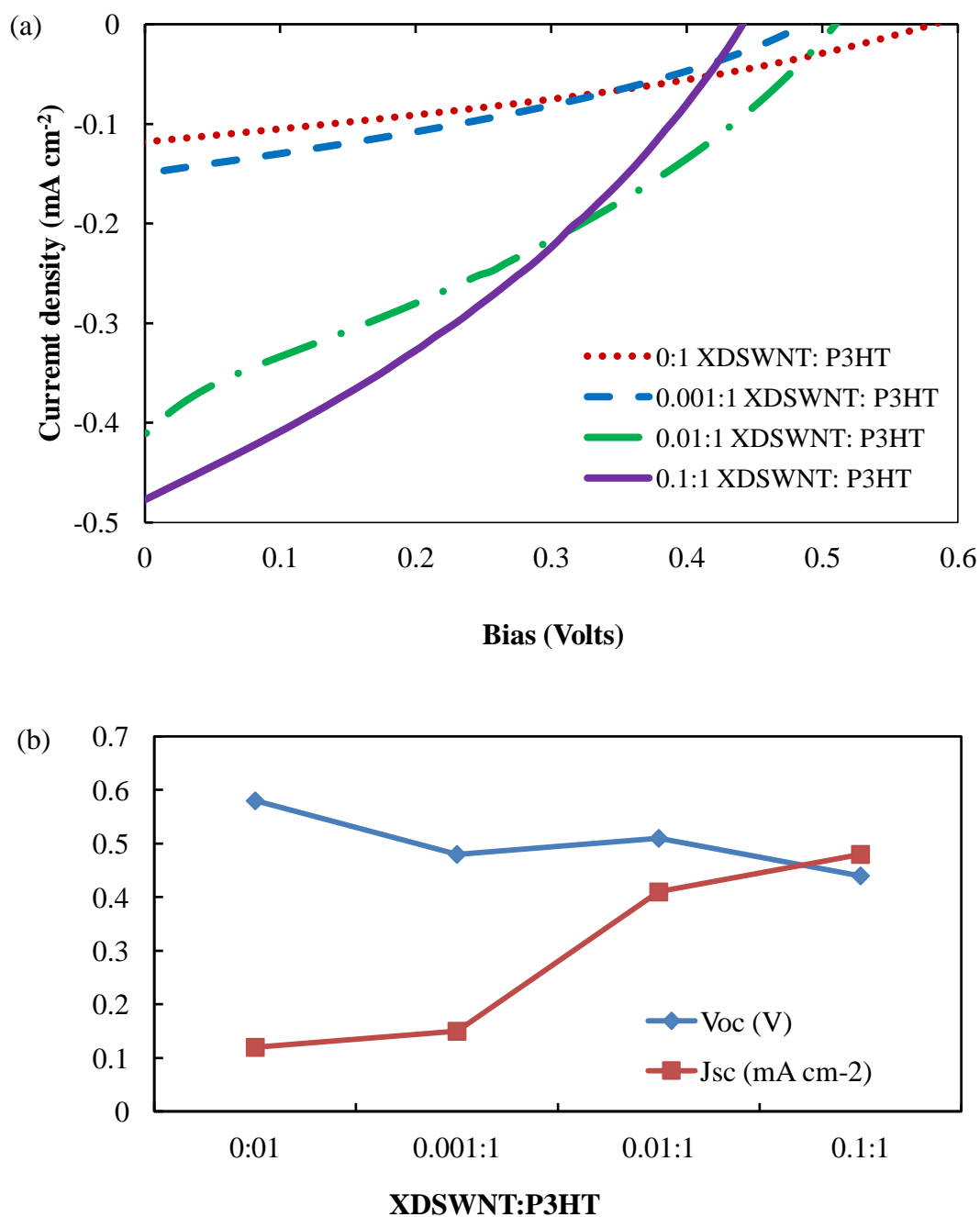
Figure 8. (a) J-V characteristics of SSDSSCs with different weight ratio of XDSWNT and P3HT; (b) The trend line of open-circuit voltage (V_{oc}) and short-circuit current density (J_{sc}) with different weight ratio of XDSWNTs and P3HT.

Table 2 summarizes the results from different weight ratios of XDSWNT and P3HT. Samples with 0.1:1 of XDSWNT: P3HT gave the best efficiency. At this weight ratio, the efficiency of the SSDSSC increased three times compared to that of samples without XDSWNT. In conclusion, as long as the amount of P3HT is enough to wrap all the XDSWNT in the solution, more XDSWNT in the mixture can lead to higher short-circuit current and improves the solar cell efficiency significantly.

Table 2. The device characteristics of SSDSSCs with different weight ratio of XDSWNT and P3HT

	XDCNT : P3HT (in weight ratio)			
	0:1	0.001:1	0.01:1	0.1:1
V_{oc} (V)	0.58	0.48	0.51	0.44
J_{sc} (mA cm^{-2})	0.12	0.15	0.41	0.48
P_{max} (μW)	0.92	0.98	2.60	2.80
FF	0.33	0.34	0.31	0.33
η (%)	0.023	0.025	0.065	0.070

3.4 Summary

In summary, we have successfully fabricated ZnO-based SSDSSC with P3HT as hole transport material. The effect of the P3HT annealing temperature and the P3HT film thickness on device efficiency was investigated. The overall energy conversion efficiency achieved in this work was 0.023% with pristine P3HT. With addition of XDSWNT into P3HT, open-circuit voltage dropped slightly, but short-circuit current

increased by several times. By having weight ratio of XDSWNT and P3HT at 0.1:1, the short-circuit current was quadrupled and the device efficiency was tripled to reach 0.07%, compared to devices without XDSWNT doping. However, the efficiency of ZnO-based SSDSSC is still very low even for device doped with XDSWNT. Compared to reported DSSCs, the major issue in ZnO-based solar cell is its very low short-circuit current density. To improve the efficiency of our SSDSSCs, further investigation on ZnO properties and improvement on device configuration are needed. These include the characterization of the electrical properties of the ZnO nanoparticle thin film, such as carrier mobility and lifetime and charge trap densities, and improvement of carrier mobility of hole transport polymers.

4. SOLID-STATE DYE-SENSITIZED SOLAR CELLS BASED ON ZNO

NANOPARTICLE AND NANOROD ARRAY HYBRID PHOTOANODES

4.1 Introduction

The rapidly increasing fossil fuel consumption and excessive greenhouse gas emissions have put significant pressure on the already-exhaustive global energy demand and needs for environmental protection. The global growing demand for energy and for protecting our environment can potentially be met by solar cell technology. Although the solar cells technology has not yet been in large-scale utilization because of its high cost and insufficient conversion efficiencies in the past, recent advances in nanomaterial and device technologies have offered new opportunities for it to become competitive to fossil fuels. Among the diverse photovoltaic devices, the dye-sensitized solar cells (DSSCs) technology has made enormous progresses and is highly competitive for large-scale commercial fabrication.

DSSCs have emerged as an attractive choice for solar energy harvesting since their invention [8]. The critical component in DSSCs is the photoanode, which is typically composed of a porous TiO_2 or ZnO nanoparticle film with dye molecules adsorbed onto its surface. To achieve high performance, the photoanode needs to possess a large surface area and good electron transport capability. A TiO_2 or ZnO nanoparticle film provides a large enough surface area; however, electron transport is difficult because of the need for electrons to hop across neighboring nanoparticles. Moreover, it is well-known that semiconducting particle surfaces are prone to form defects that can

act as electron trapping centers. The presence of these surface traps is detrimental to electron transport because trapping/detrapping events are unavoidable during electron diffusion through the disordered nanoparticle network [86-88]. By altering the morphology of the photoanode, electron transport pathways may be designed to improve electron collection.

DSSCs based on dense ZnO nanowire/nanorod arrays have been reported to exhibit improved electron transport efficiency [30]. Intensity modulated photovoltage and photocurrent spectroscopies have revealed that photoanode-based on ZnO nanorod arrays exhibit two orders of magnitude faster electron transport while retaining similar electron recombination time compared to photoanodes based on nanoparticles [77]. However, the photocurrents and the efficiencies of the nanowire/nanorod-based DSSCs are limited by insufficient surface area for dye adsorption [30]. To further improve the performance of DSSCs, various ZnO structures, such as branch structure [20], nanoflower [36], and hybrid nanowire/nanoparticle [20, 89, 90] have been employed as the photoanodes to achieve fast electron transport while maintaining a large surface area for dye coating.

Despite their high efficiency, DSSCs based on liquid electrolyte have reliability issues caused by the liquid redox electrolyte. Device instability and the need for good device packaging have become major hurdles for commercial application of DSSCs [9]. Furthermore, liquid electrolyte based solar cells cannot be easily fabricated into multicell modules [10]. One way to address this manufacturing difficulty is to replace the liquid redox electrolyte by a solid-state hole transport material, typically a p-type conjugated

polymer. Recently, many attempts have been made by using different hole transport materials, such as OMeTAD [11, 12], pentacene [80], poly(triphenyldiamine) [81], polythiophene [82], and poly(3-hexylthiophene) (P3HT) [13], along with dye-loaded porous nanoparticle films. Solid-state DSSCs with ZnO nanorod arrays as photoanodes and different conjugated polymers as hole transport material have also been reported with efficiencies of ~0.20% [54, 55].

In this work, we, to the best of our knowledge, for the first time explore the use of ZnO nanorod and ZnO nanoparticle hybrid electrodes for solid-state DSSCs. We fabricated solid-state DSSCs by using ZnO nanoparticles to fill the interstitial voids between ZnO nanorod arrays as the photoanode, hoping to further improve the efficiency of the solid-state DSSC device. The ZnO nanorod arrays serve as direct pathways for fast electron transport, and the ZnO nanoparticles filled in the interstitial space of ZnO nanorods offer a large surface area for dye adsorption. Using this hybrid nanorod-nanoparticle structure, a significant improvement in performance has been achieved. The effects of the ZnO photoanode morphology on the solid-state DSSC's performance are discussed.

4.2 Experimental methods

4.2.1 ZnO nanoparticle synthesis

Colloidal ZnO nanoparticles with nearly uniform diameters of 5 nm were prepared by hydrolyzation process. This method has been previously reported elsewhere [85], only a brief summary is given here. Sixteen mmol of KOH was dissolved in 150 ml

methanol at 60°C with refluxing and stirring for 5 min, followed by addition of 8 mmol of zinc acetate dihydrate ($Zn(Ac)_2 \cdot 2H_2O$) in 50 ml methanol. This mixture was refluxed and stirred at 60°C for 2 h. The ZnO colloids were then concentrated from 200 ml to 20 ml at 60°C by rotary evaporation under vacuum. After adding 100 ml of hexanes and 20 ml of isopropyl alcohol, the mixture was kept at 0°C overnight. ZnO precipitate was then redispersed in methanol with the removal of the supernatant.

4.2.2 Device fabrication

Fluorine-doped tin oxide glass substrates (FTO, 15 Ω/square) were cleaned by acetone and isopropyl alcohol and coated with a thin layer of ZnO nanoparticles by drop-casting in methanol and annealed at 300°C for 10 min. ZnO nanorods were grown by immersing seeded substrates in aqueous solutions containing 0.05 M zinc nitrate hexahydrate ($Zn(NO_3)_2 \cdot 6H_2O$) and 0.05 M methenamine ($C_6H_{12}N_4$) at 95°C for 90 min. Subsequently, the nanorod array thin films were rinsed with deionized water and dried in air at the same temperature. Formation of the ZnO nanoparticles in the interstices of the ZnO nanorod arrays was carried out by drop-casting low concentration ZnO nanoparticles in methanol. For nanoparticle photoanodes, ZnO nanoparticles were drop-casted on the seeded substrates to meet the length of nanorod arrays. After annealing at 300°C for 30 min, zinc oxide photoanodes were sensitized in a 0.5 mM solution of $RuL_2(NCS)_2$, L=2,2'-bibyridyl-4,4'-dicarboxylic acid (N3 dye) in ethanol at room temperature for 30 min. Then, the dye-adsorbed ZnO thin films were immersed in ethanol to remove excess dyes. Regioregular poly(3-hexylthiophene) (P3HT) was

dissolved in 1, 2-dichlorobenzene and used as hole transport material. A thin layer of P3HT was spin-coated onto dye-loaded photoanodes with a concentration of 0.5 mg ml^{-1} at 200 rpm. Another layer of P3HT was then spin-coated onto the films with a concentration of 20 mg ml^{-1} at 800 rpm. After spin-coating, devices were annealed in a vacuum oven at 150°C for 30 min. Finally, 100 nm thick gold contacts were thermally evaporated through a shadow mask. The active area of the devices was 2.25 mm^{2}.

4.2.3 Solar cell characterization

The crystal orientation of nanorod arrays and nanoparticles were recorded by an XRD (Bruker D8 Discover with Cu Kα radiation operated at 40 kV, 40 mA). The morphologies of the photoanodes were characterized using field emission scanning electron microscopy (FE-SEM) (JEOL JSM-7500F operated at 10 KeV). To evaluate the light absorption of the dye-loaded ZnO photoanodes, UV-vis-NIR (Hitachi U-4100 UV-vis-NIR spectrophotometer) spectra were acquired in absorption mode. To evaluate solar cell performance, the fabricated devices were illuminated under a standard solar simulator at AM 1.5 condition (100 mW cm^{-2}) with current density-voltage (J-V) characteristics acquired by a Keithley 2400 sourcemeter.

4.3 Results and discussion

The degree of crystal orientation of ZnO nanorod arrays and nanoparticles were determined by X-ray diffraction (XRD) spectrum as shown in **Figure 9**. The dominant peak for randomly oriented ZnO powders is at 36.2 ° and corresponds to (101) plane. For

nanorod arrays, the strong diffraction peak seen at 34.4 ° corresponds to the ZnO (002) plane. The enhanced (002) peak indicates the ZnO nanorods grow along *c*-axis and perpendicular to the substrate.
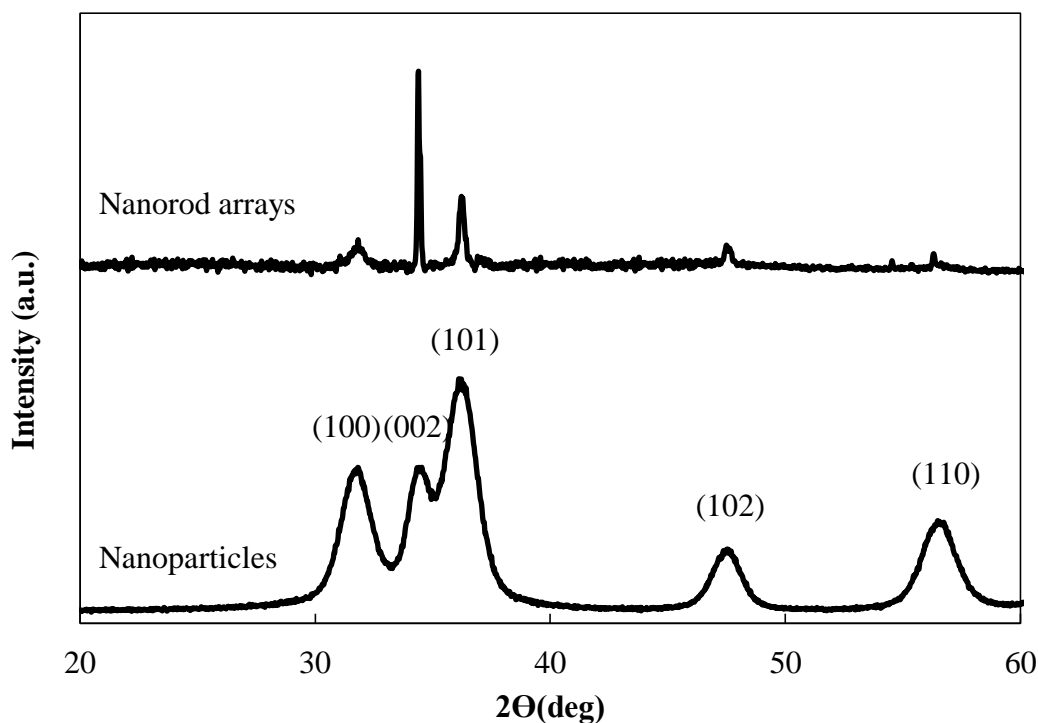
Figure 9. X-ray diffraction patterns of the ZnO nanorod arrays and ZnO nanoparticles.

The schematic and field emission scanning electron microscopy (FE-SEM) images of solid-state DSSCs based on four different ZnO photoanode morphologies are shown in **Figure 10**. **Figure 10(a)** shows the schematic of the solar cell based on ZnO nanorod arrays, denoted as sample 1. Sample 2 contains a hybrid ZnO structure in which ZnO nanorod arrays are partially filled with ZnO nanoparticles (**Figure 10(b)**). Sample 3

possesses a hybrid ZnO structure in which the interstitial voids between nanorod arrays are fully filled by ZnO nanoparticles (**Figure 10(c)**). The difference between sample 2 and sample 3 is the amount of nanoparticles in the interstices between the nanorods. sample 4 is a photovoltaic device based on ZnO nanoparticles alone (**Figure 10(d)**). **Figure 10(e)(f)(g)(h)** shows the corresponding FE-SEM images of ZnO photoanodes before dye loading. The average diameter of ZnO nanoparticles is 5 nm. The thickness of the ZnO seed layer for nanorod growth is about 100 nm. ZnO nanorods have a diameter in the range of 30 to 40 nm, and are about 250 nm in length. The thickness of the ZnO thin film in sample 4 is kept the same as the length of ZnO nanorods in samples 1 to 3. Solar cells with the four photoanode morphologies are investigated to illustrate the factors that affect the solar cell performance.

Electron transport is much more efficient in single crystal nanorods than in particulate thin films. First, there is a direct pathway for electrons to reach the electrode through nanorods. In addition, nanorods have smaller surface-to-volume ratio compared to nanoparticles, thus possessing fewer surface defect states that trap electrons. Therefore, electrons have a much higher mobility and can travel through nanorods tens to hundreds times faster than that through thin films composed of nanoparticles.[30, 39, 77] Efficient electron transport helps shorten the time needed for electron to travel to the electrode, thus lowering probability of the recombination loss of electrons.
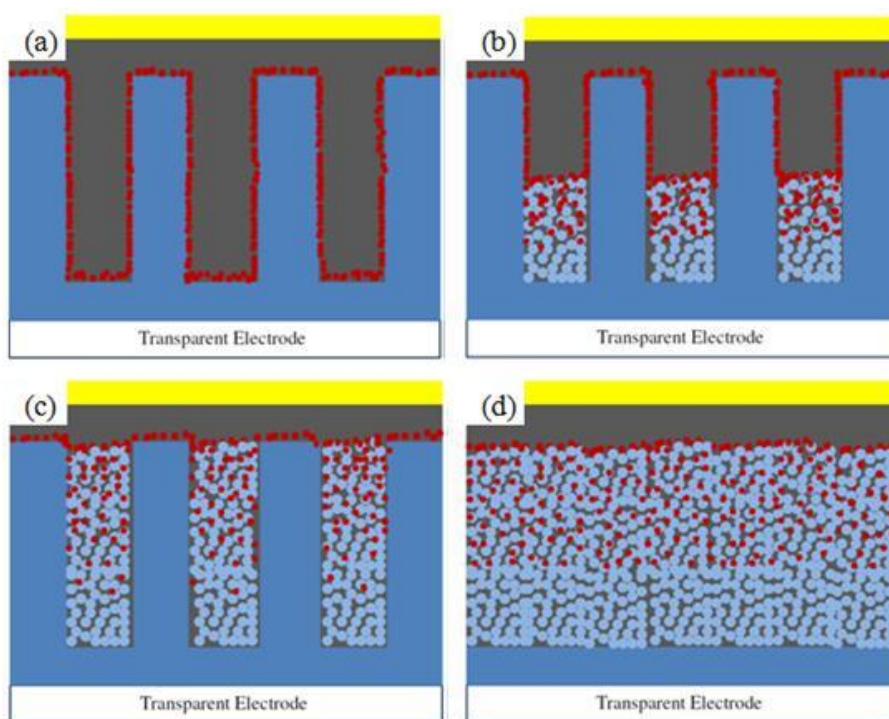
Figure 10. Schematics and FE-SEM images for solid-state DSSCs with different photoanode morphologies. Schematics of device based on (a) nanorod array photoanode (sample 1), (b) nanorod array photoanode with nanoparticles partially filling the interstices (sample 2), (c) nanorod array photoanode with nanoparticles fully filling the interstices (sample 3), (d) nanoparticle photoanode (sample 4). Blue rectangles represent ZnO nanorods, blue dots represent ZnO nanoparticles, red dots represent N3 dyes, the grey film represents P3HT, and the yellow film represents gold. FE-SEM images of photoanodes for (e) sample 1, (f) sample 2, (g) sample 3, (h) sample 4. The scale bar is 100 nm for all SEM images.
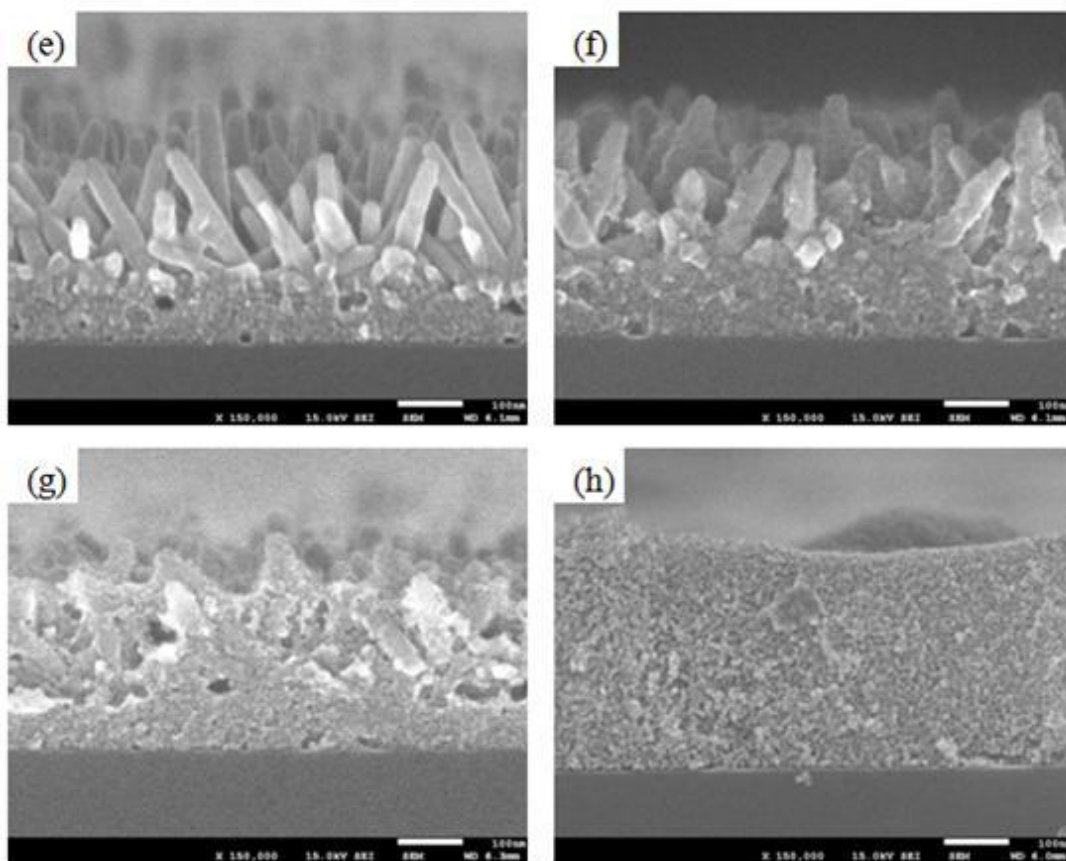
Figure 10. Continued.

However, ZnO photoanodes based on nanorod arrays suffer from limited surface area that can absorb dye molecules for efficient light harvesting when compared to the electrodes based on nanoparticles. By filling the interstitial space between nanorods with 5-nm-size ZnO nanoparticles, the total surface area of ZnO photoanodes can be greatly increased. Light absorption of the device can thus be increased without compromising efficient electron transport of ZnO nanorod arrays. Furthermore, compared to more than thousand times hopping in a particulate thin film, electrons injected from dye molecules

into nanoparticles can reach ZnO nanorods, and then the electrode, just by hopping across a few nanoparticles [20, 91]. By minimizing the number of interparticle hoppings, the carrier recombination can be greatly reduced. Consequently, it is anticipated that, with increasing number of dye molecules on ZnO surfaces and with less recombination of electron-hole pairs by using the hybrid ZnO nanorod-nanoparticle photoanode morphologies shown in **Figure 10(b)** and **Figure 10(c)**, large photocurrents can be generated while maintaining a high open-circuit voltage.

In this study, we use N3 dye as the light-absorbing material for the device. Even though P3HT can also function as the light-absorbing component, its main function is to transport holes in the device. Two layers of P3HT were spin-coated on top of the dye-loaded ZnO photoanode. The first spin-coating with diluted P3HT solution provides good wetting of the ZnO photoanode, while the second spin-coating with concentrated P3HT solution deposits a thick enough film to smooth out the surface irregularity of ZnO photoanode to prevent electrode shorting. Without spin-coating the diluted P3HT as the first layer, voids can be formed between ZnO photoanode. **Figure 11** shows the expected energy levels of the materials from reported values in literature [19, 92, 93]. The conduction band of ZnO is lower than the lowest unoccupied molecular orbital (LUMO) level of N3, enabling electron transfer from N3 to ZnO. Although the LUMO level of the P3HT is similar to that of N3, the difference between the LUMO level of P3HT and the N3 dye is much smaller than the difference between the conduction band of ZnO and the LUMO level of the N3 dye. Accompanied with very low electron mobility in P3HT, majority of electrons are expected to be injected from N3 to ZnO.
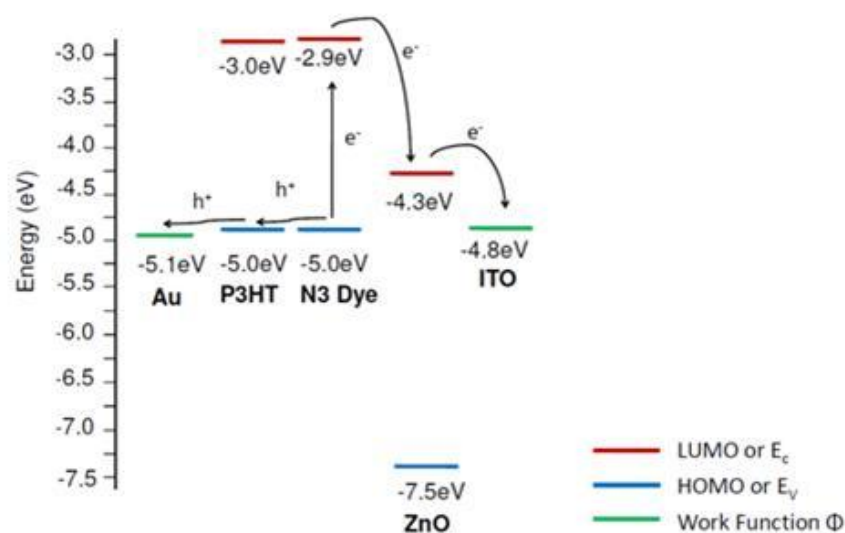
Figure 11. A schematic of the energy level diagram of the FTO/ZnO/N3/P3HT/Au device.

ZnO solar cells with structures described in **Figure 10** were characterized by measuring the current density-voltage (J-V) behavior under air mass (AM) 1.5 condition. **Figure 12** shows typical J-V curves of the devices with different morphologies. **Table 3** summarizes short-circuit currents (J_{sc}), open-circuit voltages (V_{oc}), fill factors (FF), and overall energy conversion efficiencies (η) for devices based on various photoanode morphologies.
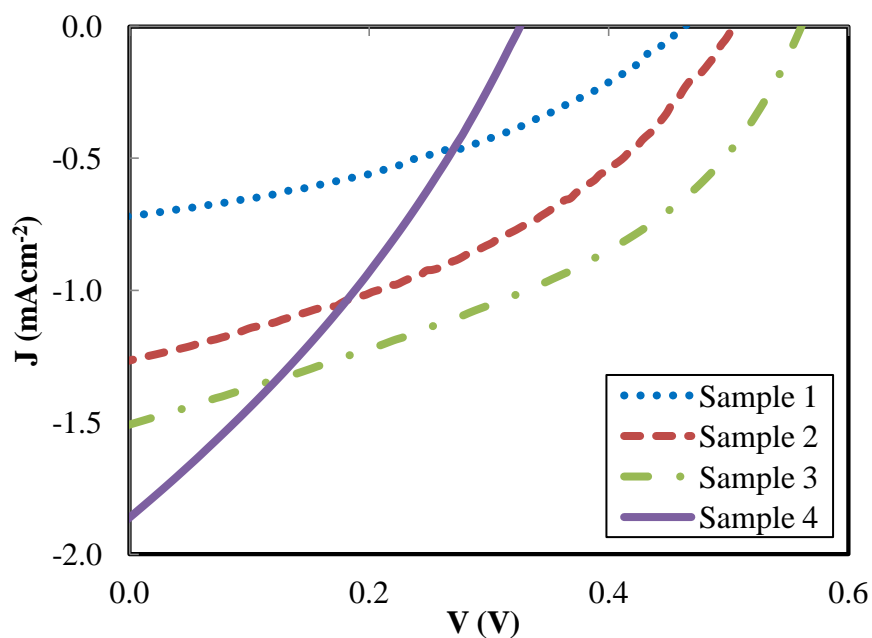
Figure 12. Current-voltage characteristics of FTO/ZnO/N3/P3HT/Au devices based on different ZnO photoanodes.

Table 3. Device parameters for solid-state DSSCs with different ZnO morphologies based on three batches of samples.

Sample	J_{sc} (mA cm^{-2})	V_{oc} (V)	FF	η (%)
1	0.72±0.12	0.46±0.06	0.38±0.02	0.13±0.02
2	1.27±0.16	0.50±0.07	0.39±0.01	0.25±0.01
3	1.52±0.04	0.56±0.01	0.40±0.01	0.34±0.02
4	1.86±0.11	0.32±0.03	0.31±0.03	0.19±0.01

J_{sc} is determined by the initial number of photogenerated carriers and the injection effectiveness of electrons from dye molecules to metal oxide [21]. Since the

devices are composed of the same materials, it is assumed that the electron injection efficiency from N3 dye to ZnO photoanode is the same for all morphologies. Thus, the differences in J_{sc} values from the devices are due to the initial number of photogenerated carriers, which is proportional to the light-harvesting capability of the dye-loaded ZnO electrode. Optical absorption spectra of dye-loaded ZnO photoanodes show the variation in light absorption capability of different ZnO structures. In **Figure 13**, all the samples exhibit an intrinsic absorption with similar absorption intensity below 380 nm, which is due to the band gap absorption in ZnO. On the other hand, significant variation in light absorption capability at wavelengths above 380 nm is mainly originated from the density of the dye molecules on the ZnO surfaces and is related to the photoanode morphology. It should be noted that the absorption peak of N3 dye is centered at around 520 nm. Among four different ZnO thin film morphologies, the device based on sample 4 has the highest absorption intensity, followed by sample 3, sample 2, and sample 1. This absorption intensity corresponds to the total internal surface area of the ZnO film. The optical spectra illustrate that more effective photon capturing is achieved in the visible light region with larger total surface area of the ZnO photoanode because more N3 dyes can be adsorbed onto the film. With the largest internal surface area and the highest amount of N3 dye, sample 4 has the highest J_{sc}, followed by the devices based on sample 3, 2, and 1. Their corresponding current densities are 1.86 mA cm^{-2}, 1.52 mA cm^{-2}, 1.27 mA cm^{-2}, and 0.72 mA cm^{-2}, respectively.
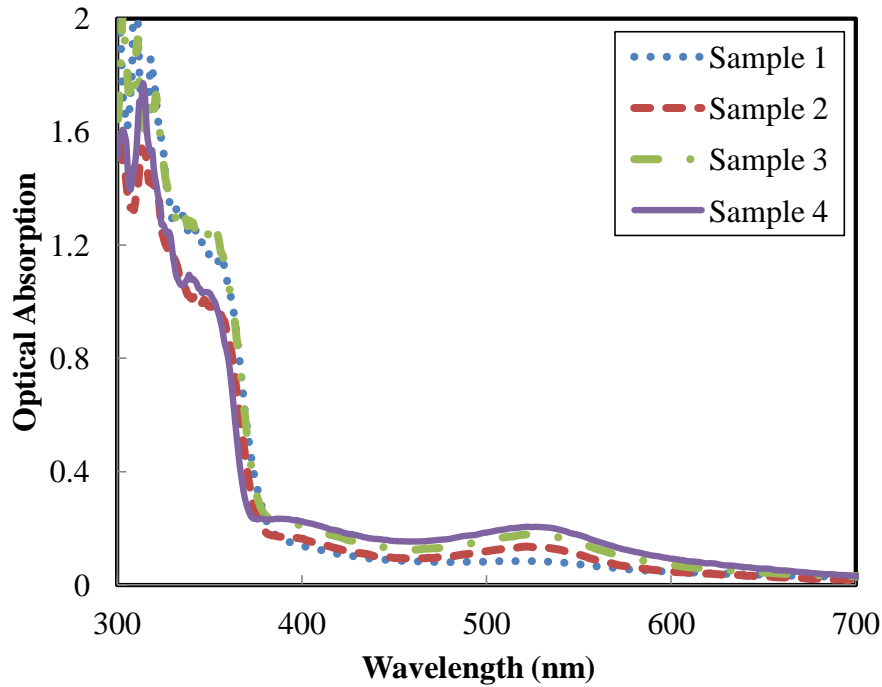
Figure 13. Optical absorption of ZnO photoanodes with 30 min dye loading.

Sample 1 has a V_{oc} of 0.46 V compared to 0.32 V for sample 4. The increase in the V_{oc} indicates that the electron-hole recombination rate is lower in sample 1 than in sample 4 [94]. This is possibly resulted from differences in electrical properties between ZnO nanoparticles and nanorods, and from the faster electron transport in nanorods. With even higher V_{oc} from sample 2 and sample 3, which are 0.50 V and 0.56 V, respectively, it is anticipated that nanorods do improve electron transport compared to porous films composed of nanoparticles. In sample 2 and sample 3, electrons generated from dye-coated nanoparticles adjacent to nanorods need only one single hop to reach nanorods. As for electrons generated from other dye-coated nanoparticles, the number of hops becomes more than one, but this number of hops is still much less than that in

sample 4. As a result, nonorods provide efficient transport pathways for electrons coming from surrounding nanoparticles, which reduces the total travel distance for electrons, and thus the chances of electron recombination during transport. Another possible reason is that by filling the voids between nanorods with nanoparticles, the amount of light absorption by P3HT is reduced. Light absorbed in P3HT generates excitons with short diffusion lengths, and most of the excitons will eventually recombine if they are not located very close to the P3HT-ZnO interface. In samples 2 and 3, fewer excitons are generated in P3HT because the P3HT layer is located behind the dye-loaded ZnO nanoparticles. This will generate more useful photo-carriers and increase V_{oc}.

The fill factors of samples 2 and 3 are 0.39 and 0.40, respectively, which are approximately the same as the FF of Sample 1. The FFs of the devices based on hybrid photoanodes are higher than that of the nanoparticle-based device, which is only 0.31. Again, this indicates that nanorod arrays serve as efficient transport pathways for electrons, and the parasitic losses in the devices containing nanorod arrays are lower than those containing nanoparticles only. As a result, sample 3 has the highest overall energy conversion efficiency, followed by sample 2, sample 4, and sample 1 with their respective efficiency of 0.34%, 0.25%, 0.19%, and 0.13%.

While J_{sc}, V_{oc}, FF, and η are well accepted indicators for solar cell performance, additional information can be obtained by analyzing the entire J-V curve. We analyzed the measured J-V characteristics using the lumped circuit model for solar cell and find the diode parameters following the approach described elsewhere [94, 95]. The current equation for a solar cell device under illumination can be expressed as:

$$J = J_o \exp\left[\frac{q}{AkT}(V-RJ)\right] + GV - J_L \qquad (1)$$

where J and V are the diode current density and voltage, J_o is the diode reverse saturation current density, q is the electron charge, A is the diode quality factor, k is the Boltzmann constant, T is temperature, R is the series resistance, G is the shunt conductance, and J_L is the photocurrent density. Diode parameters can be determined from the standard J-V curve shown in **Figure 12** along with plots shown in **Figure 14**.
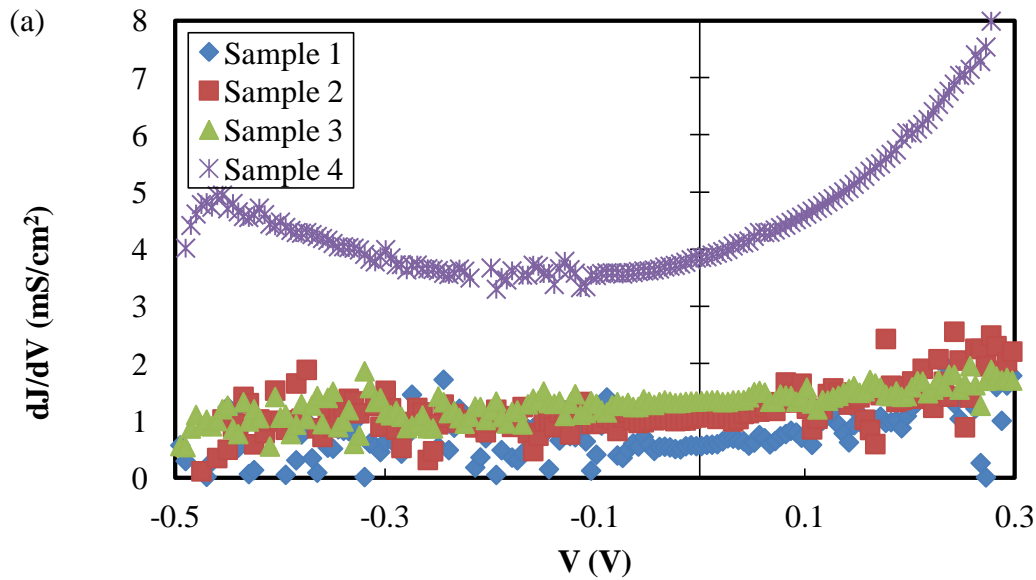
Figure 14. Diode parameters of FTO/ZnO/N3/P3HT/Au devices based on different ZnO photoanodes. (a) dJ/dV versus V for shunt conductance (G) characterization. (b) dV/dJ versus $(J+J_{sc})^{-1}$ for the determination of serious resistance(R) and diode ideality factor (A). (c) $J+J_{sc}-GV$ versus V-RJ for the determination of reverse saturation current (J_o).

(b) [graph with y-axis "dV/dJ (Ω cm^2)" ranging 0 to 20, x-axis "$(J+Jsc)^{-1}$ (mA^{-1}cm^2)" ranging 0 to 0.2, legend: Sample 1, Sample 2, Sample 3, Sample 4]

(c) [graph with y-axis "J+Jsc-GV (mA^{-1}cm^2)" ranging 0.01 to 100, x-axis "V-RJ (V)" ranging 0.4 to 1, legend: Sample 1, Sample 2, Sample 3, Sample 4]
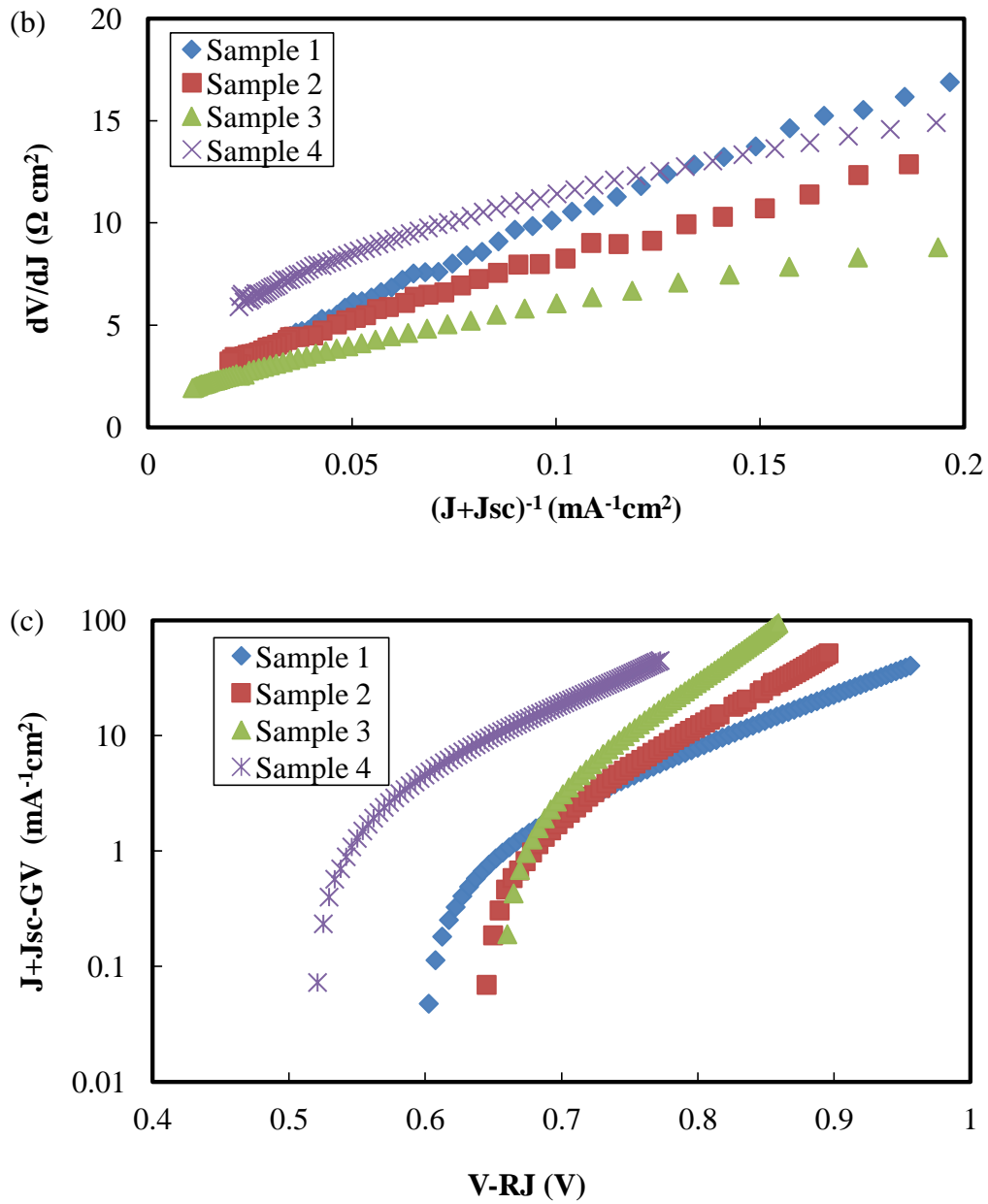
Figure 14. Continued.

The value of G can be extracted from **Figure 14(a)**, where dJ/dV versus V is plotted. For an efficient solar cell, the value G should be as small as possible to prevent internal leakage of current through the cell. This leakage limits the FF of the device.

Calculated values of G are listed in **Table 4**. Sample 1 has the lowest value of G, which equals to 0.5 mS/cm^2. With increasing amount of nanoparticles used in the device, the value of G increases. As a result, sample 4 gives the largest value of G, 3.8 mS/cm^2, and has the largest amount of leakage current through the cell.

By plotting dV/dJ vs $(J+J_{sc})^{-1}$ in **Figure 14(b)**, the value of series resistance can be obtained. Same as G, for an efficient solar cell, R should be as small as possible. From **Table 4**, sample 1 has the lowest value of R, 1.06 Ω cm^2, and sample 4 gives the largest value of R, 4.41 Ω cm^2.

Table 4. List of diode parameters for solid-state DSSCs with different ZnO morphologies.

Sample	G (mS cm^{-2})	A	R (Ω cm^2)	J_o (mA cm^{-2})
1	0.5	3.72	1.06	1.92x 10^{-3}
2	1.1	2.56	1.93	6.67x 10^{-5}
3	1.3	1.95	1.45	4.01x 10^{-6}
4	3.8	3.07	4.41	4.03x 10^{-3}

The ideality factor A and the reverse saturation current J_o can help understanding the recombination mechanism of the devices. When A is close to 1, the limiting recombination mechanism is the recombination in the charge neutral region. When A is close to 2, the limiting recombination mechanism is the recombination in the space-charge region. When A is larger than 2, additional recombination mechanisms are

incorporated [94]. If we consider values for A calculated from **Figure 14(b)**, as listed in

Table 4, samples 1, 2, and 4 all have the value of A larger than 2 and the ideality factor

is as high as 3.72 for sample 1. In devices based on these three photoanode morphologies,

tunneling recombination for trapped electrons and holes is a significant recombination

mechanism. ZnO nanoparticle surfaces and disordered P3HT thin film are full of defects

that behave as traps for charges. Trapped electrons have higher chances of geminate

recombination with trapped holes by tunneling back to the original molecules [96]. The

value of A for sample 3 is only 1.95, which suggests space-charge region recombination

is more significant than tunneling recombination in this sample. The fast removal of

electrons in ZnO nanoparticles through nanorod arrays may be the reason for low

tunneling recombination.

      Figure 14(c) shows a semi-logarithmic plot of $J+J_{sc}-GV$ against $V-RJ$. The value

of J_o is again calculated from the plot and is listed in **Table 4**. For sample 1 and sample 4,

$J_o = 1.92 \times 10^{-3}$ and 4.03×10^{-3}, respectively. For samples 2 and 3, J_o decreases by two to

three orders of magnitude to 6.67×10^{-5} and 4.01×10^{-6}, respectively. Overall J_o decrease is

due to decreased defect density and less carrier recombinations.

      Although the values of G and R from sample 3 are not the lowest ones, they are

in an acceptable range compared to the other three samples. Sample 3 has the lowest A

and J_o as a result of having the lowest carrier recombination rate in all samples. By

analyzing the values of G, R, A, and J_o, it is reasonable to state that sample 3 gives the

best performance and this agrees with the results from η. It is also reasonable to suggest

that by using nanorod arrays longer than 250 nm as scaffold for the device may bring

even higher efficiency. With longer nanorods, more interstitial space can be occupied by ZnO nanoparticles. Thus, more dyes can be loaded onto the ZnO surface. At the same time, though the length of the nanorod arrays is different, the distance between each ZnO nanorod is still in the similar range and charge recombination can be reduced efficiently.

Despite the efficiency improvement with the use of hybrid photoanodes, the solar cell efficiencies obtained in this work are still low compared to similar devices made of TiO_2. Lower efficiency is almost universally observed in ZnO-based solar cells in published work, so properties directly related to ZnO nanomaterials are most likely the efficiency-limiting factors. These could be high-density defects on the surfaces of ZnO nanomaterials, which trap charges and lead to step-wise electron-hole recombination through mid-bandgap defect energy levels. Additionally, oxygen molecules absorbed at the surface of ZnO nanomaterials can serve as efficient exciton quenching centers. Further experiments are needed to investigate those factors and to shed light on the root cause of lower efficiency in ZnO-based solar cells.

4.4 Conclusion

Solid-state DSSCs based on various morphologies of ZnO photoanodes with N3 dye as the light absorbing material and P3HT as the hole transport material have been fabricated. The effect of the morphology of the ZnO photoanodes has been investigated. Short-circuit current increases with the amount of ZnO nanoparticles in the photoanode due to large surface area for dye loading. Compared to pure nanoparticle photoanode, V_{oc} increases with the presence of ZnO nanorod arrays due to faster electron transport

and less charge recombination. The overall conversion efficiency of the solid-state DSSC based on ZnO nanorod arrays is 0.13%. By fully filling the interstitial voids of the nanorod arrays with 5 nm size ZnO nanoparticles, the device efficiency increases significantly to 0.34%. Analysis from diode parameters shows the values of A and J_o decrease in solid-state DSSCs based on the hybrid ZnO photoanodes. This suggests that devices based on hybrid ZnO photoanodes have lower charge recombination rate. To improve the efficiency of solid-state DSSCs based on hybrid ZnO photoanodes, further quantitative investigations on charge-trapping defects and carrier recombination rates from various mechanisms in ZnO nanoparticles and ZnO nanorod arrays are still needed.

5. SOLID-STATE DYE-SENSITIZED SOLAR CELLS FROM A LAYER-BY-LAYER DEPOSITION PROCESS

5.1 Introduction

Excitonic photovoltaic devices — including organic, hybrid organic/inorganic, and dye-sensitized solar cells (DSSCs) — are promising alternatives to conventional inorganic solar cells due to their potential for low cost and low temperature solution-based processing on flexible substrates in large scale. One of the major goals of current excitonic solar cell research and development is to improve the device's efficiency. By modifying the morphology of inorganic constituent in hybrid and dye-sensitized solar cells, the photovoltaic efficiency could be improved. As the key components, many inorganic semiconductors have been applied as nanostructured materials for these solar cells, such as TiO_2 [8, 11], ZnO [19-22], CdSe [23], PbS [24, 25], $CuInSe_2$ [26], and many others. Among these semiconducting nanomaterials, ZnO is an up-and-coming candidate because of its diverse morphologies by solution syntheses.

In DSSCs, the critical nanostructured component, photoanode, is usually composed of a porous nanoparticulate film which possesses a large surface area for dye molecules to adsorb onto its surface [8, 11]. Other than absorption, the photovoltaic performance is also determined by carrier transport capability in the device. In general, a thicker ZnO nanostructured film provides a larger surface area for dye attachment and thus more excitons can be generated; however, it is more difficult for electrons to reach the bottom electrode due to a longer pathway for them to hop across adjacent nanoparticles. Although nanoparticulate films provide enough surface area for dye

adsorption, one major drawback coming from the nanoparticle thin films themselves is that semiconducting particle surfaces have a tendency to form defects which operate as electron trapping centers. Since trapping/detrapping events are inevitable when electrons diffuse through the disordered nanoparticle network [86-88], it is necessary to alter the morphology of the photoanode and design a relatively direct electron transport pathway to improve electron collection. One of the promising structures is vertically oriented nanorod arrays. Single crystalline ZnO nanorods could be beneficial for direct electron transport for collecting charges. It has been revealed that ZnO nanorod array photoanodes transport electrons two magnitude faster than ZnO nanoparticle photoanodes, at the same time, maintaining a similar electron recombination time [77]. Liquid electrolyte-based DSSCs with ZnO nanowire/nanorod array photoanodes have been reported to demonstrate superior electron transport efficiency [30]. Several groups of researchers also reported successful fabrication of solid-state DSSCs or hybrid solar cells based on vertically aligned ZnO nanorods as electron acceptor and transporter. Efficiencies of the reported solid-state devices range from 0.2% to 0.6% and the length of nanorod arrays are from 180 nm to 550 nm [22, 54, 58, 59]. Though nanorod arrays perform good electrical properties, the photocurrents of the DSSCs with nanorod array photoanodes are restricted by the total ZnO surface area for dye loading [30]. In addition, the spacing between ZnO nanorods is on the order of 100 nm and is larger than the typical exciton diffusion length, 4-20 nm, of conjugated polymers [4]. This large spacing leads to a high spontaneous recombination rate for excitons generated in the hole-transporting conjugated polymers. In order to balance the trade-off between light

absorption and electron transport, various ZnO structures other than pure nanoparticulate films and pure nanorod arrays have been employed in liquid-electrolyte based DSSCs, such as branch structure [20], nanoflower [36], a hybrid nanowire/nanoparticles [20, 89, 90].

In this work, we propose to fabricate solid-state DSSCs with hybrid ZnO nanoparticle/nanorod array photoanodes and investigate the influence of the length of ZnO nanorods on the photovoltaic performance. ZnO nanoparticles are filled into the interstitial space between nanorod arrays by a novel layer-by-layer deposition method. The layer-by-layer deposition technique solves the issue of incomplete filling of deep ZnO nanorod arrays with random orientations, while at the same time provides uniform dye loading throughout the ZnO nanoparticle film. The nanoparticles in the interstitial space between nanorod arrays provide large surface areas for the loading of dye molecules, while nanorod arrays collect electrons from nanoparticles and serve as efficient pathways to transport electrons to the electrode.

5.2 Experimental methods

5.2.1 Device fabrication

Fluorine-doped tin oxide glass substrates (FTO, 15 Ω/square) were cleaned by acetone and isopropyl alcohol and then coated with a thin layer of ZnO nanoparticles by drop-casting in methanol and annealed at 300°C for 10 min. Colloidal ZnO nanoparticles with nearly uniform diameters of 5 nm were prepared by hydrolyzation process. This method has been previously reported elsewhere [85]. ZnO nanorods were grown by

immersing seeded substrates in aqueous solutions containing 0.05 M zinc nitrate hexahydrate ($Zn(NO_3)_2 \cdot 6H_2O$) and 0.05 M methenamine ($C_6H_{12}N_4$) at 90°C for a certain time depends on the desired nanorods length [29]. Subsequently, the nanorod array thin films were rinsed with deionized water and dried in air at the same temperature. Formation of the ZnO nanoparticles in the interstices of the ZnO nanorod arrays was carried out by a layer-by-layer process (**Figure 15**).

The substrates with nanorod arrays were first immersed in a dye solution which was mixed with 0.5 mM mercurochrome ($C_{20}H_8Br_2HgNa_2O$) and 0.5 mM N3 ($RuL_2(NCS)_2$, L=2,2'-bibyridyl-4,4'-dicarboxylic acid) in ethanol in a 3:1 volume ratio. After 2 min of dye loading, the samples were rinsed by ethanol to remove excess dye molecules and heated on a hot plate at 70°C for another 2 min to remove solvent. Then samples were immersed in a 20 mg ml^{-1} ZnO solution in methanol with sonication for another 2 min, rinsed by methanol to remove loosely-attached ZnO nanoparticles, and heated on a hot plate at 70°C for 2 min. This completed the first cycle of the process by having one layer of dyes and one layer of ZnO nanoparticles. The layer-by-layer process was repeated for a few cycles until the interstitial voids between ZnO nanorod arrays were fully filled by nanoparticles.

After layer-by-layer process, zinc oxide photoanodes were sensitized in a 0.5 mM solution of mercurochrome in ethanol at room temperature for 30 min and then rinsed by ethanol to remove excess dyes. Regioregular poly(3-hexylthiophene) (P3HT) was dissolved in 1,2-dichlorobenzene and utilized as hole transport material. Two layers of P3HT were spin-coated onto dye-loaded photoanodes. The first layer of P3HT was

spin-coated with a concentration of 0.2 mg ml^{-1} at 200 rpm. The second layer of P3HT was then spin-coated onto the films with a concentration of 20 mg ml^{-1} at 800 rpm. After two spin-coatings, devices were annealed in a vacuum oven at 150°C for 30 min. To complete the fabrication, 100 nm thick gold were thermally evaporated through a shadow mask and employed as top electrode. The active area of the devices was 2.25 mm^{2}.
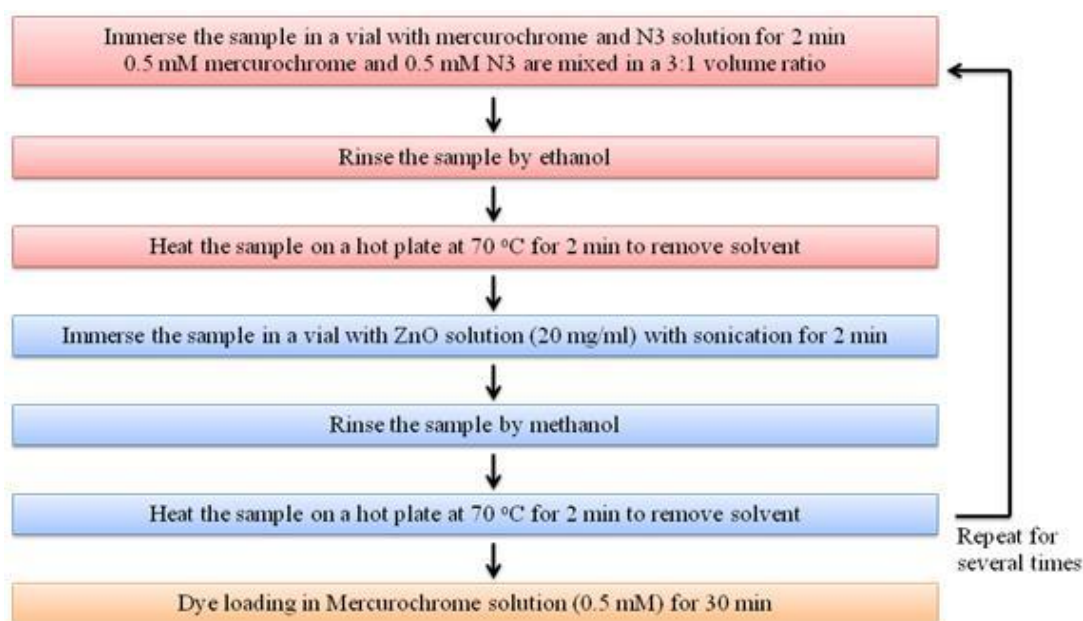
Figure 15. Flow chart of layer-by-layer method to fill nanoparticles into interstitial space between nanorod arrays.

5.2.2 Solar cell characterization

The morphologies of the ZnO photoanodes were characterized using field emission scanning electron microscopy (FE-SEM) (JEOL JSM-7500F operated at 15

KeV). To evaluate the light absorption of the dye-loaded ZnO photoanodes, UV-vis-NIR (Hitachi U-4100 UV-vis-NIR spectrophotometer) spectra were acquired in absorption mode. Photovoltaic performance of the fabricated devices was measured when illuminated under a standard solar simulator at AM 1.5 condition (100 mW cm^{-2}) with current density-voltage (J-V) characteristics acquired by a Keithley 2400 sourcemeter.
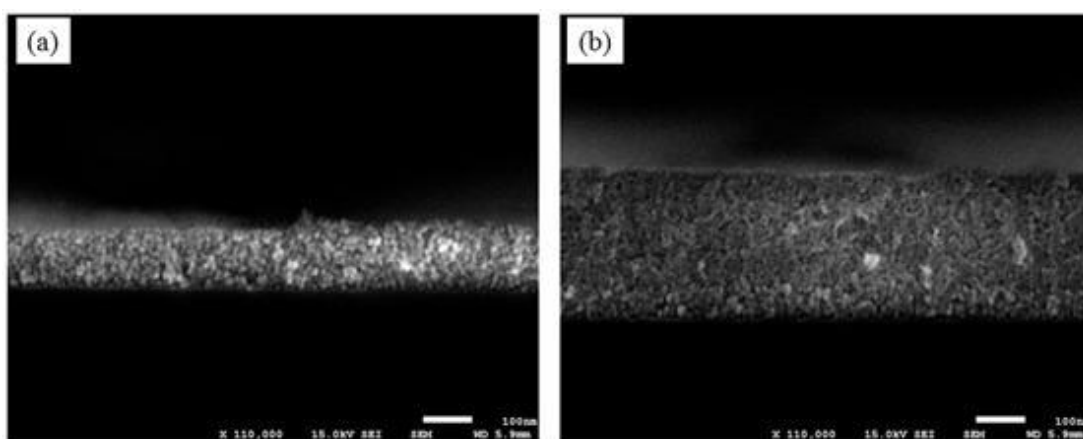
Figure 16. SEM images of a ZnO nanoparticle film (a) before and (b) after 6 cycles of layer-by-layer deposition. Scale bar: 100 nm.

5.3 Results and discussion

5.3.1 Layer-by-layer process for ZnO deposition and dye loading

Layer-by-layer deposition is a technique used for well-controlled deposition of thin films from solution. The interaction mechanisms that provide coupling between two adjacent layers can be Coulomb attraction, covalent bonding or hydrogen bonding. ZnO nanoparticles in colloidal solution and dissolved mixtures of dye molecules of mercurochrome ($C_{20}H_8Br_2HgNa_2O$) and N3 ($RuL_2(NCS)_2$,

L=2,2'-bibyridyl-4,4'-dicarboxylic acid) are charged, which presents possibility to form layer-by-layer thin film through electrostatic interaction. The mixture of dyes (mercurochrome: N3 = 3:1) are used in this work because it provides good process repeatability and good device efficiency. Layer-by-layer deposition of ZnO and dye molecules can be performed by immersing the substrate in ZnO colloidal solution and dye solution alternatively, with thorough rinsing steps to avoid cross contamination of solutions between two soaking steps. To investigate the characteristics of this new deposition method, layer-by-layer deposition of bilayers of ZnO nanoparticles and dye molecules was first performed on a flat substrate. **Figure 16(a)** shows the SEM image of the initial 120 nm thick nanoparticle film composed of 5 nm ZnO nanoparticles. **Figure 16(b)** presents the image after six cycles of layer-by-layer deposition. The thickness of the film increased from 120 nm to 290 nm, corresponding to an average bilayer thickness of about 30 nm. This thickness is much greater than the diameter of the ZnO nanoparticles, indicating the ZnO nanoparticles are not close-packed. Despite of irregular packing, the average film thickness in each bilayer is quite consistent. The repeatability of the process is corroborated by optical absorption spectra (**Figure 17(a)**) of the thin films with different cycles of layer-by-layer process, which show increasing light absorption of the films with more deposited layers in approximately linear scale. Due to the 3.2 eV bandgap of ZnO, all the samples exhibit an intrinsic absorption below 380 nm as shown in **Figure 17(b)**. Obviously, with more layers of dyes and nanoparticles deposited onto the original nanoparticulate film, the absorption intensity below 380 nm increases as a result of the increasing amount of ZnO nanoparticles in the

system. It is also reasonable to compare the absorption intensity and the thickness of the films from **Figure 16**. The initial film thickness is 120 nm with absorption intensity lies around 0.25; after six cycles of deposition, the film thickness grows to 290 nm while absorption intensity is around 0.6. The ratio between the increased film thickness and absorption intensity is very close to each other. On the other hand, the variation in light absorption intensity at wavelength above 380 nm is mostly resulted from the dye molecules loaded on ZnO nanoparticle surface and is related to the amount of both mercurochrome dye and N3 dye. The absorption peak is at around 517 nm for mercurochrome dye and at about 520 nm for N3 dye. Among seven samples with different deposition cycles, the initial film without dye deposition shows no peak at 520 nm. With increasing number of deposition cycles, the absorption intensity also increases correspondingly (**Figure 17(c)**). From SEM images and light absorption spectra, the layer-by-layer deposition has been confirmed to be a reliable and controllable technique to deposit ZnO nanoparticle thin film with uniform dye loading.
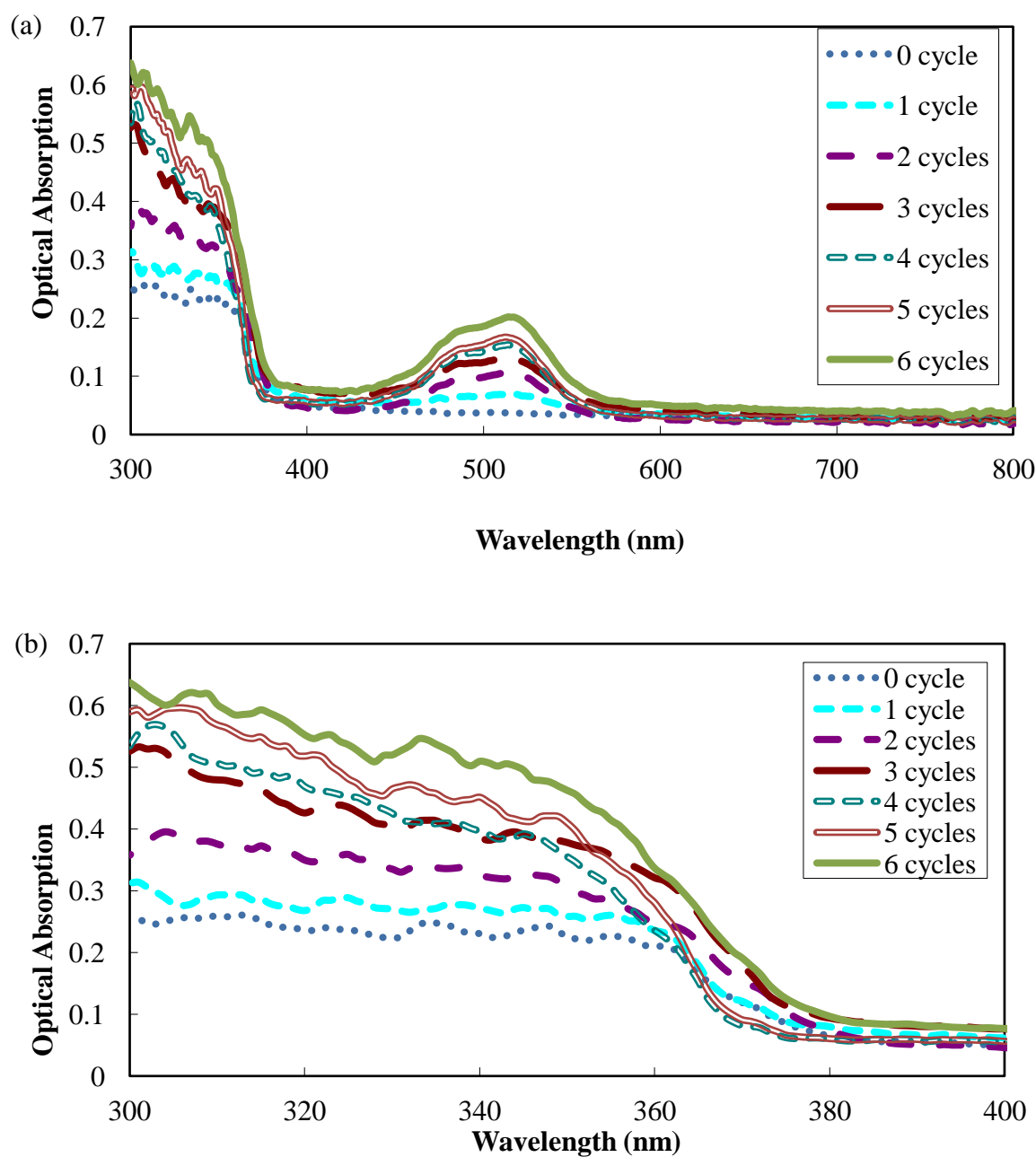
Figure 17. (a) Optical absorption of ZnO nanoparticulate films with 0 to 6 deposited dye and ZnO nanoparticle bilayers. (b) Enlarged absorption spectrum for ZnO absorption. (c) Enlarged absorption spectrum for mixed N3 and mercurochrome.
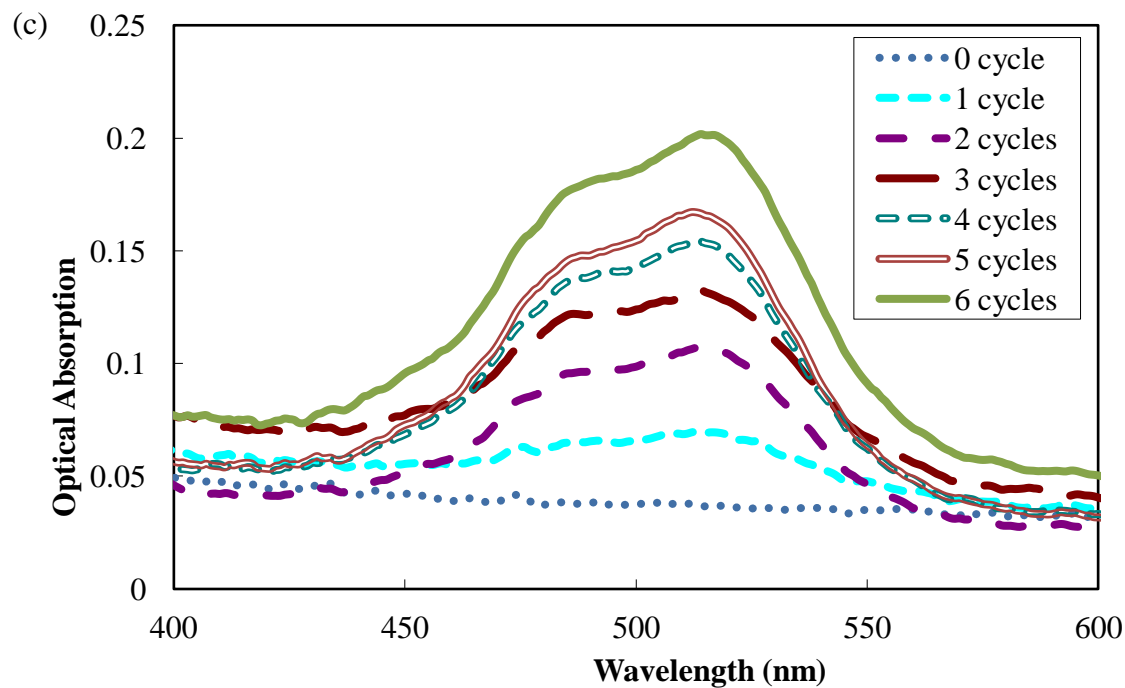
Figure 17. Continued.

5.3.2 Layer-by-layer process on ZnO nanorod array photoanode

The schematic of the hybrid nanoparticle/nanorod array photoanodes at several different stages during the layer-by-layer process are shown in **Figure 18**. The initial photoanode (**Figure 18(a)**) is composed of a ZnO nanoparticle seed layer on the bottom and ZnO nanorod arrays grown from the seed layer. After immersing the photoanode in the dye solution with 3:1 mercurochrome dye to N3 dye, a thin layer of the photo-sensitizers attach to the surface of ZnO nanorods (**Figure 18(b)**). Followed by immersing the dye-attached photoanode into ZnO nanoparticle solution with sonication, ZnO nanoparticles bind with the carboxyl group of the N3 dye[97-99], which is already attached to the ZnO nanorod, and start to form ZnO aggregates (**Figure 18(c)**). **Figure**

18(d) and **Figure 18(e)** show another cycle of the deposition for ZnO nanoparticles to fill the interstitial space between nanorod arrays. **Figure 18(f)** presents the final structure in which the interstitial space between nanorod arrays is completely filled with nanoparticles. Thus the hybrid nanoparticle/nanorod array photoanode is formed with a thickness being the same as the length of the nanorod arrays. During deposition process, dye molecules also adsorb onto the ZnO surface and are well-distributed in the device because they only need to diffuse into a 20 nm to 30 nm ZnO thin film each time. Depends on the length of the nanorods and particularly the spacing between them, the number of cycles needs to be applied on the photoanode is different.

FE-SEM images of hybrid nanoparticle/nanorod array photoanodes with three different lengths are shown in **Figure 19**. **Figure 19(a)** shows the FE-SEM image of averagely 500 nm long nanorod arrays after the first cycle of layer-by-layer deposition of ZnO nanoparticles. **Figure 19(b)** and **Figure 19(c)** show the same nanorod arrays after the fourth and the sixth cycle of processing, respectively. For 500 nm long ZnO nanorods that is grown in 105 minutes, their diameter is in the range of 35-45 nm, and the average spacing between nanorods is on the order of 100 nm. With more and more cycles of layer-by-layer processing, gaps between nanorods are gradually filled by ZnO nanoparticles loaded with dye molecules. After six cycles of depositions, all the voids between the nanorods are filled. **Figure 19(d)(e)(f)** show the same processing on nanorod arrays with around 1200 nm in length and 70-80 nm in diameter. **Figure 19(g)(h)(i)** show the results on 2600 nm long nanorod arrays with 95-105 nm in

diameter. Growth time for 1200 nm long nanorod arrays was 3 h, and that for 2600 nm long nanorod arrays was 6 h.

Since the layer-by-layer deposition occurs on the sidewalls of the nanorod arrays, the total number of deposition needed to completely fill the nanorod arrays is determined by the average distance between the nanorods, not their height. For all three selected lengths of nanorod arrays in this work, six cycles of processing are required to fill the spacing between nanorods. It should be noted that though ZnO nanoparticles are deposited layer-by-layer for several times, there is no distinct boundary between each layer in FE-SEM images. The same procedure was also applied on samples by using N3 dye only or mercurochrome dye only instead of the 3:1 mixture of both dye molecules. With N3 dye only, four cycles of processing is enough for nanoparticles to completely occupy the space between nanorods.

However, there is always a distinct area between neighboring ZnO nanoparticle layers with a thickness of around 6 nm. One of the possible explanations is that N3 dyes dissolve the ZnO thin film and form Zn^{2+}-N3 dye agglomerates [97-100]. Oppositely, for samples with mercurochrome dyes only, the space between nanorod arrays is not filled after six cycles of deposition due to no aggregation formed between mercurochrome and ZnO.
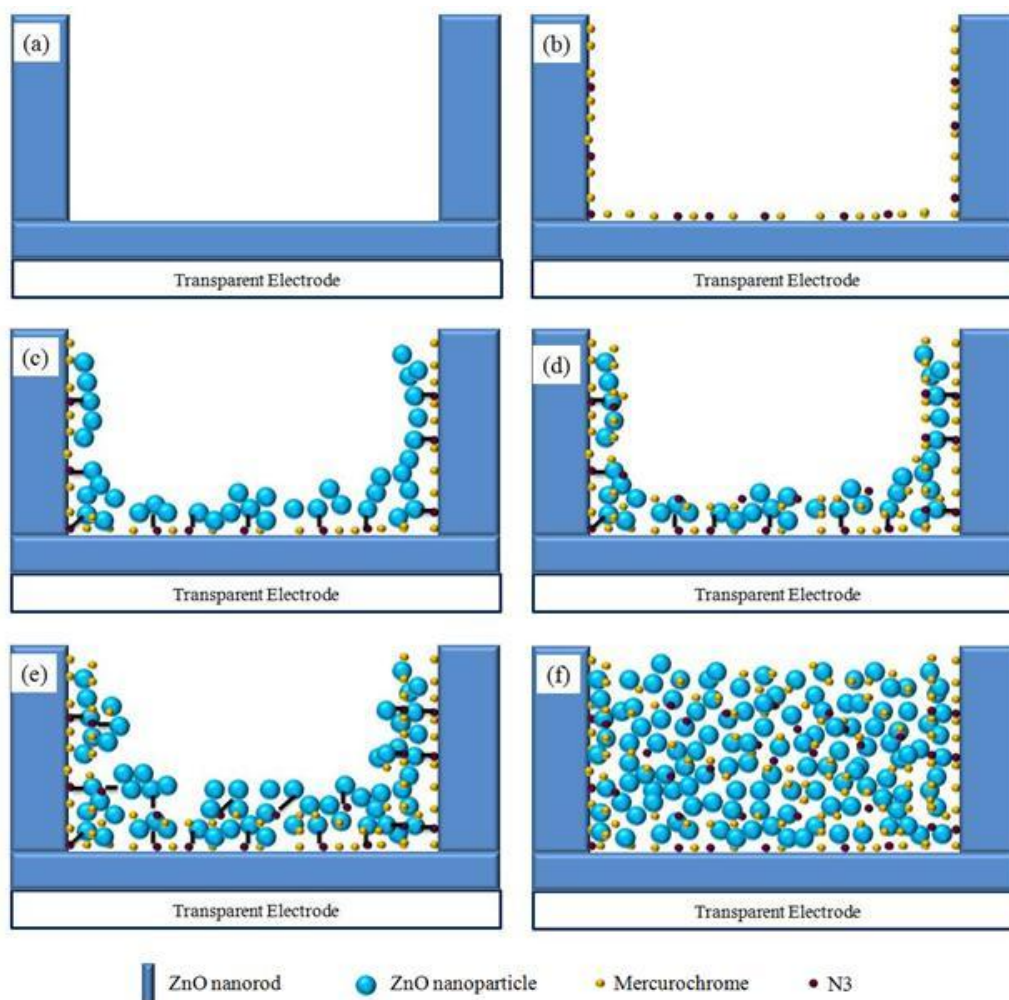
Figure 18. Schematics of layer-by-layer method to fill nanoparticles into interstitial space between nanorod arrays: (a) ZnO nanorod array photoanode. (b) ZnO nanorod array photoanode with first layer of dye molecules. (c) ZnO nanorod array photoanode with first layer of ZnO nanoparticles in the interstitial space. (d) ZnO nanorod array photoanode with second layer of dyes attach on the ZnO nanoparticles from the first cycle of deposition. (e) ZnO nanorod array photoanode after second cycle of deposition. (f) Final structure with complete filling of interstitial space between nanorods. Figures are not drawn in scale.
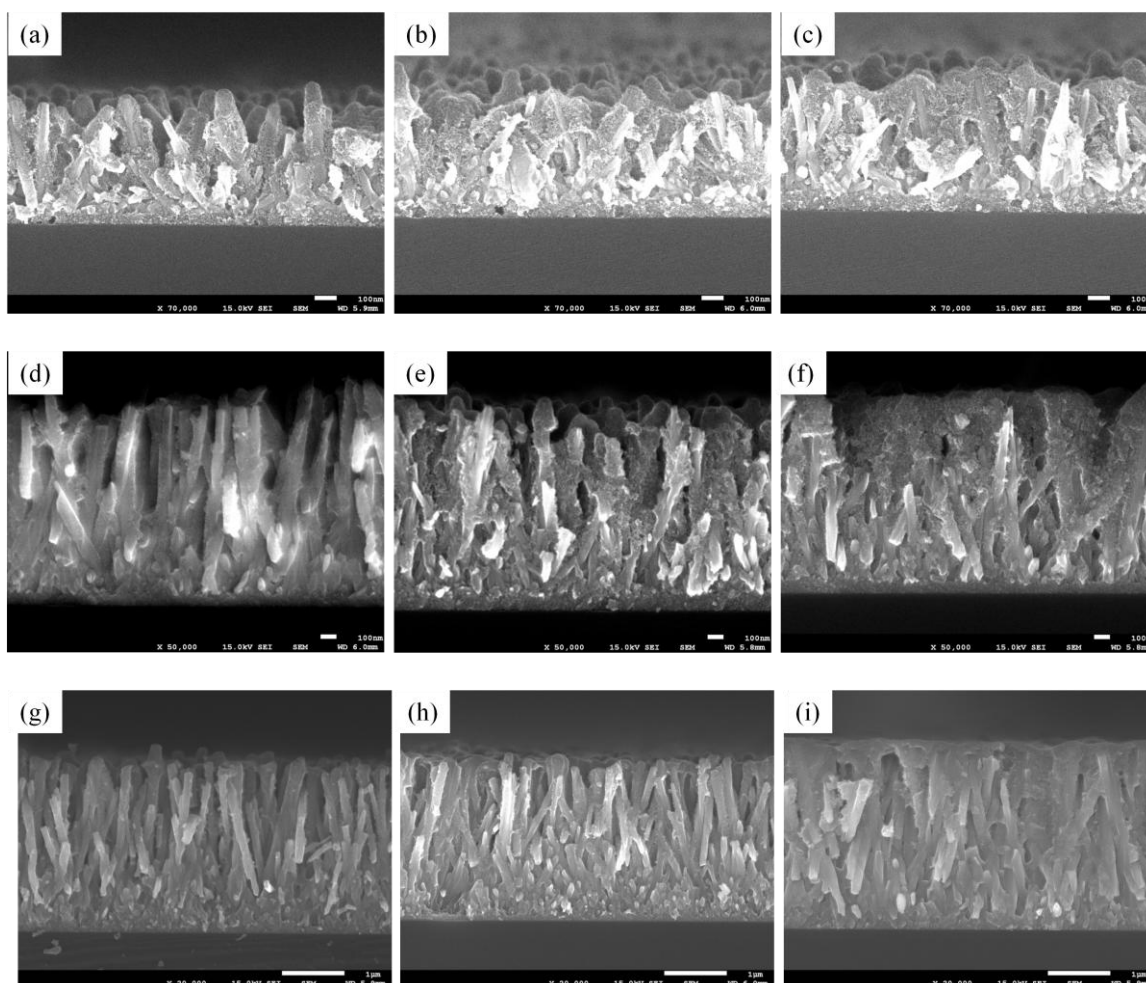
Figure 19. SEM image of ZnO nanorod arrays after different cycle of layer-by-layer deposition: 500 nm long ZnO nanorod arrays (a) after 1 cycle, (b) after 4 cycles, and (c) after 6 cycles of layer-by-layer deposition of ZnO nanoparticles. 1200 nm long ZnO nanorod arrays (d) after 1 cycle, (e) after 4 cycles, and (f) after 6 cycles of layer-by-layer deposition of ZnO nanoparticles. 2600 nm long ZnO nanorod arrays (g) after 1 cycle, (h) after 4 cycles, and (i) after 6 cycles of layer-by-layer deposition of ZnO nanoparticles.

Figure 20 shows the light absorption spectra for three nanorod arrays after six cycles of layer by layer processing. Absorption capability of the three photoanodes is directly related to the length of nanorod arrays, or in other words, the thickness of the hybrid nanoparticle/nanorod array thin film. The spacing between nanorods is within similar range because all three samples with different nanorod length need six cycles of processing to fill the gap between nanorod arrays, so the overall space that can be occupied by dye-attached ZnO nanoparticles should be related to the length of nanorods. Transmittance of three samples was also measured. For 500 nm thick photoanode, the transmittance at 520 nm is 56%. For 1200 nm one, the transmittance at the same wavelength is 27%. And for 2600 nm thick sample, the transmittance at 520 nm is 15%. The excellent light absorption capability also illustrates that although the dye loading time is short at each cycle, there are still considerable amount of dye molecules loaded in the system because the required penetration depth is thin for each run. In order to further enhance light absorption capability, a 30 min dye mercurochrome dye loading was performed after six cycles of layer by layer process.

Single crystal nanorods offer a direct pathway for electron transport. Due to their smaller surface-to-volume ratio compared to nanoparticles, nanorods possess fewer surface defect states. As a result, electron mobility in nanorods is much higher than that in nanoparticulate thin films and electron transport through nanorods is tens to hundreds faster than through nanoparticles [30, 39, 77]. This efficient electron transport lowers the probability of the recombination loss of electrons. However, nanorod array photoanodes also suffer from the limited surface-to-volume ratio for the inadequate number of dyes

loaded into the system. Oppositely, photoanodes based on nanoparticulate films possess better light absorption capability for its large enough surface area for dye attachment, while electrons injected from dye molecules to nanoparticles need to hop to adjacent nanoparticles for more than thousand times before they can reach bottom electrode and thus recombination rate in nanoparticulate photoanodes is high [20, 91]. It is rationale to retain advantages from both kinds of photoanodes if both nanorods arrays and nanoparticles are utilized in the device. By filling the space between nanorod arrays with 5 nm nanoparticles, the photoanodes now can benefit from large surface area from nanoparticles and thus light absorption capability is promoted significantly. At the same time, electrons injected from dyes to nanoparticles can reach nearby ZnO nanorods with reduced number of hopping and profit from fast electron transport.
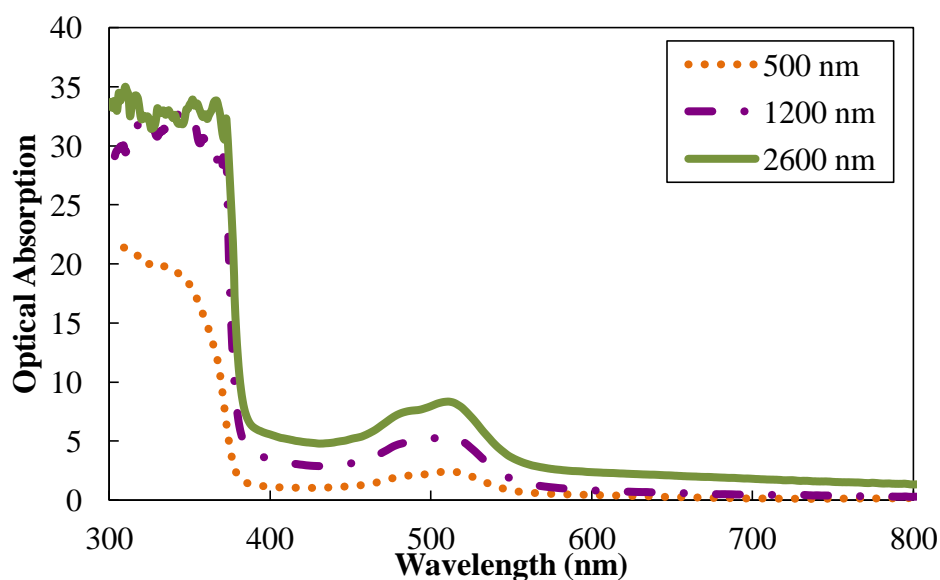
Figure 20. Optical absorption of ZnO nanorod array photoanodes after 6 cycles of layer-by-layer processing.

As mentioned, both mercurochrome dye and N3 dye are used as light-absorbing material for the device. P3HT functions as hole-transporting material due to the structural design of the cell. It has to be noted that two layers of P3HT were spin-coated onto the dye-loaded ZnO photoanodes. The first layer of P3HT was spin-coated with diluted concentration in order to provide good wetting of the photoanode for the upcoming second spin-coating. Expected energy level of the materials is presented in **Figure 21** [19, 92, 93, 101]. The conduction band of ZnO is lower than lowest unoccupied molecular orbital (LUMO) level of mercurochrome and N3 dyes, allowing electron transfer from both dyes to ZnO.
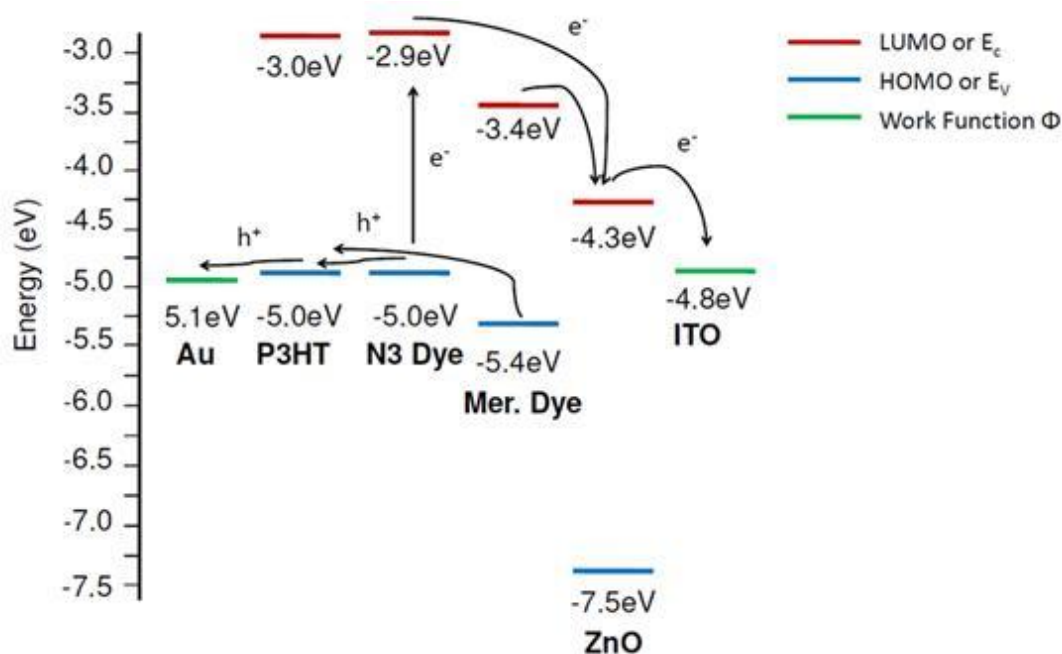
Figure 21. A schematic of the energy level diagram of the FTO/ZnO/mercurochrome: N3/ P3HT/Au device.

5.3.3 Current density-voltage characteristics

Solid-state DSSCs with structures described in **Figure 18(f)** have been fabricated with three different nanorod length as shown in **Figure 19(c)**, **Figure 19(f)**, and **Figure 19(i)**. Current density-voltage (J-V) behavior were measured under AM 1.5 condition. **Figure 22** gives typical J-V curves of the photovoltaic cells based on hybrid nanoparticle/nanorod array photoanode with different thickness. It should be noted that the curves were plotted based on the best performance cells. **Table 5** summarized short-circuit currents (J_{sc}), open-circuit voltages (V_{oc}), fill factors (FF), and overall power conversion efficiencies (η) for the three devices. For each device, at least seven samples were fabricated and measured.

Figure 22. Current-voltage characteristics of FTO/ZnO/mercurochrome:N3/ P3HT/Au devices based on ZnO photoanodes with three different thicknesses: 500 nm, 1200 nm, and 2600 nm. The curves were plotted based on the best performance cells.

Table 5. List of device parameters for hybrid nanoparticle/nanorod array based solid-state DSSCs with different nanorod lengths.

500 nm		
	Best performance	Average
V_{oc} (V)	0.54	0.60 $\pm$0.07
J_{sc} (mA cm^{-2})	2.02	1.30 $\pm$0.45
FF	0.38	0.40 $\pm$0.02
η (%)	0.41	0.30 $\pm$0.07

1200 nm		
	Best performance	Average
V_{oc} (V)	0.45	0.43 $\pm$0.05
J_{sc} (mA cm^{-2})	3.97	3.53 $\pm$0.57
FF	0.44	0.43 $\pm$0.04
η (%)	0.79	0.64 $\pm$0.06

2600 nm		
	Best performance	Average
V_{oc} (V)	0.27	0.33 $\pm$0.07
J_{sc} (mA cm^{-2})	2.38	1.86 $\pm$0.57
FF	0.32	0.32 $\pm$0.03
η (%)	0.21	0.18 $\pm$0.02

When comparing the performance of three devices, it is reasonable to find that J_{sc} increases significantly from 1.30 mA cm^{-2} to 3.53 mA cm^{-2} as the thickness of photoanode increases from 500 nm to 1200 nm. But when the thickness of photoanode

further increases to 2600 nm, J_{sc} drops to 1.86 mA cm^{-2}. Higher light absorption of the 2600 nm sample doesn't result in a higher current density. One possible explanation is the filtering effect [59, 67]. With longer nanorod arrays and thicker photoanodes, the depth that P3HT infiltrates is deeper. It is difficult for P3HT to penetrate into the mesoporous part of the devices if it is too thick. Even P3HT penetrates into mesoporous film, it becomes poorly ordered when near to the bottom of the film and exhibits inefficient hole transport ability. Thus excitons generated close to the bottom electrode are not converted into photocurrent. As a result, the tradeoff between light absorption and hole transport attributes to the relatively large J_{sc} in 1200 nm devices. Due to similar reason, V_{oc} of three devices decreases from 0.60 V to 0.33 V when the thickness of the photoanodes increases. The drop of V_{oc} is attributed to the increasing charge recombination rate arising from unbalanced electron and hole transport capability in the mesoporous films. The fill factors of 500 nm and 1200 nm thick devices are 0.40 and 0.43, respectively, while the fill factor of 2600 nm thick devices is only 0.32. Again, this indicates that 2600 nm nanorods could be too long for this application and lead to parasitic losses due to high level of charge recombination. As a result, devices based on 1200 nm hybrid nanoparticle/nanorod array photoanodes have the highest overall energy conversion efficiency, followed by devices based on 500 nm and 2600 nm thick photoanodes with their average efficiency of 0.64%, 0.30%, and 0.18%, respectively.

5.3.4 Diode parameters

Other than the well accepted indicators, J_{sc}, V_{oc}, FF, and η, additional information can be extracted by analyzing J-V characteristics using the lumped circuit model for solar cell. Detailed procedure to find the diode parameters from measured J-V curve is described elsewhere [94, 95]. The current equation for a solar cell device under illumination can be expressed as:

$$J=J_o \exp\left[\frac{q}{AkT}(V-RJ)\right]+GV-J_L \tag{1}$$

where J and V are the diode current density and voltage, J_o is the diode reverse saturation current density, q is the electron charge, A is the diode quality factor, k is the Boltzmann constant, T is temperature, R is the series resistance, G is the shunt conductance, and J_L is the photocurrent density. Diode parameters can be determined from the standard J-V curve shown in **Figure 22** along with plots shown in **Figure 23**.

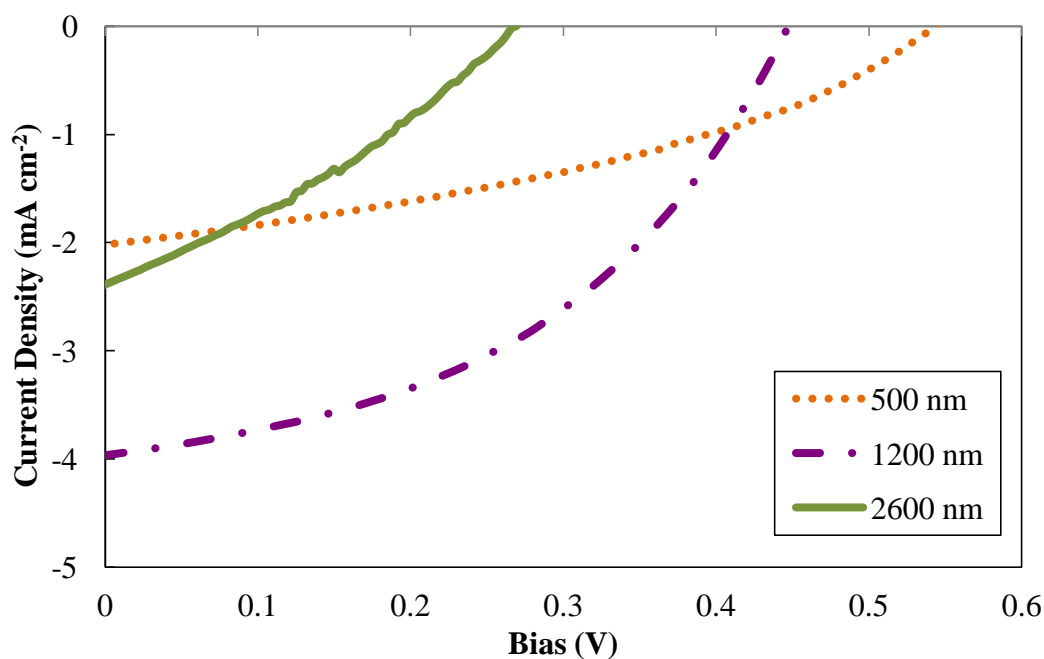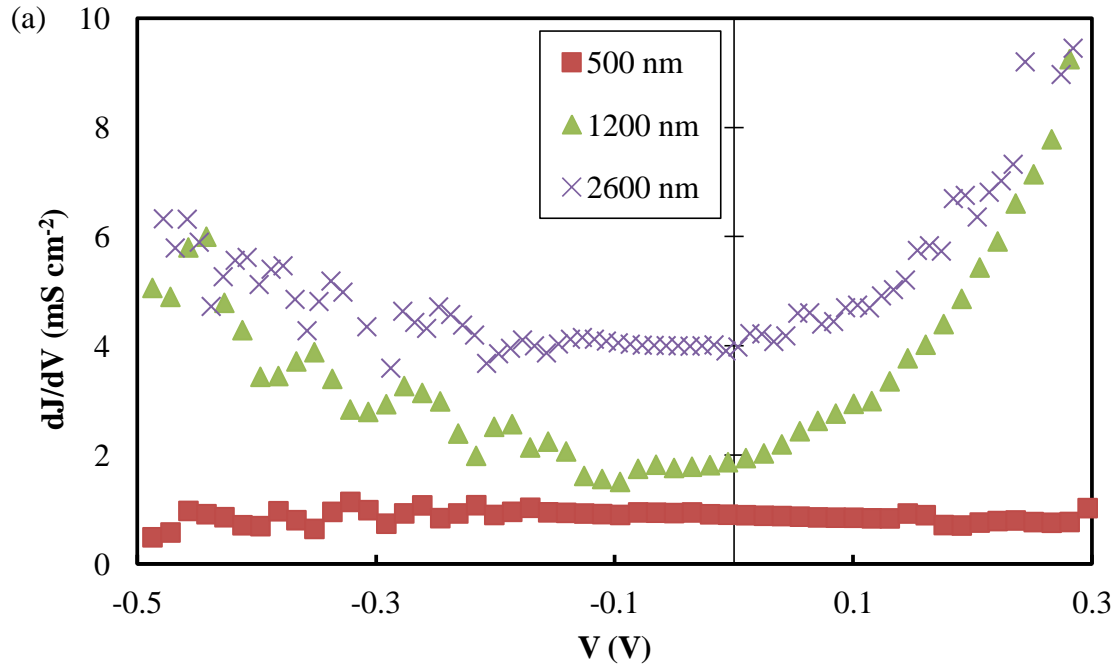**Figure 23.** Diode parameters of FTO/ZnO/mercurochrome:N3/P3HT/Au devices based on ZnO photoanodes with three different thicknesses: 500 nm, 1200 nm, and 2600 nm: (a) dJ/dV versus V for shunt conductance (G) characterization. (b) dV/dJ versus $(J+J_{sc})^{-1}$ for the determination of serious resistance(R) and diode ideality factor (A). (c) $J+J_{sc}$-GV versus V-RJ for the determination of reverse saturation current (J_o).

(b)

(c)
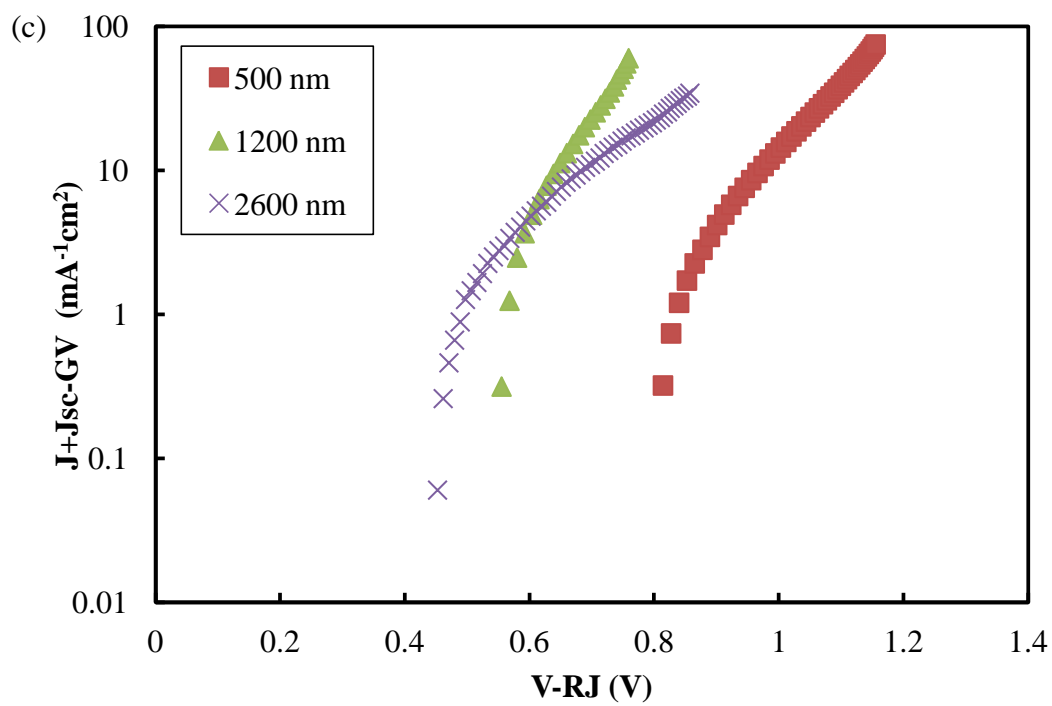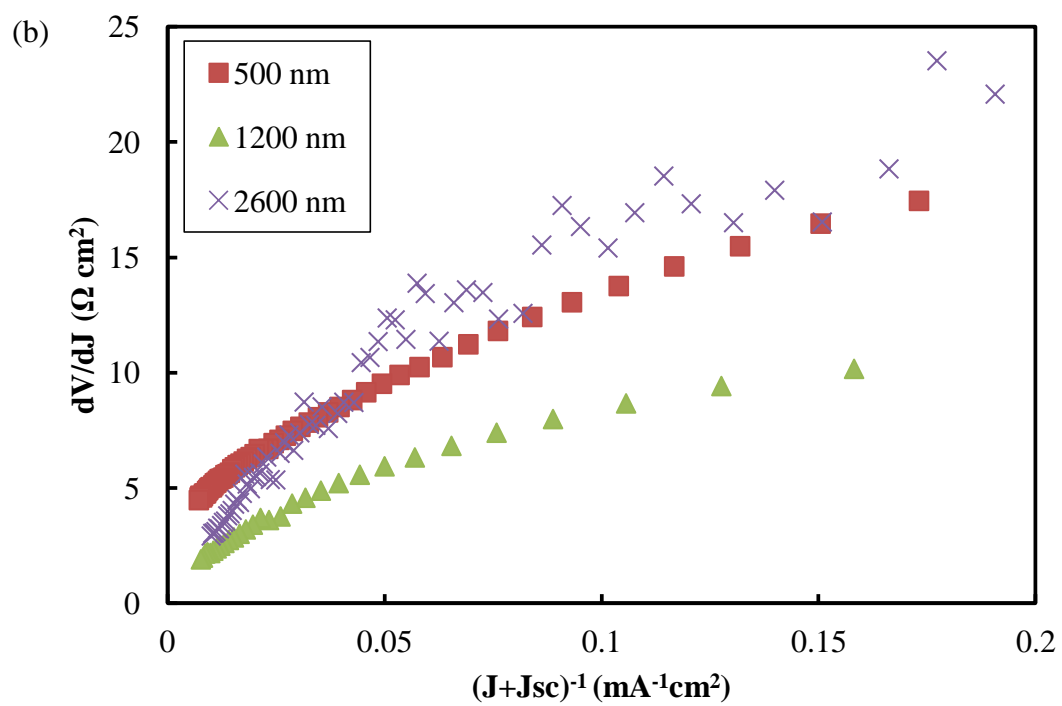
Figure 23. Continued.

For an efficient photovoltaic device, shunt conductance should be kept as small as possible. The smaller the G value, the smaller the internal leakage of current through the cell. This internal leakage limits the FF of the cell. The value of G was extracted by plotting dJ/dV versus V in **Figure 23(a)** and the calculated values are listed in **Table 6**. Shunt conductance increases from 0.9 to as high as 4.0 with increasing hybrid photoanode thickness. And the large shunt conductance value, 4.0, corresponds to low FF from 2600 nm devices, which is 0.32 in **Table 5**. By plotting dV/dJ vs $(J+J_{sc})^{-1}$ in **Figure 23(b)**, the value of series resistance can be obtained. Similar to G, for an efficient solar cell, R should be as small as possible. From **Table 6**, devices with 1200 nm thick photoanodes have the lowest value of R, 2.36 Ω cm^2, and the devices with thinnest photoanodes give the largest value of R, 4.68 Ω cm^2. The ideality factor A and the reverse saturation current J_o can facilitate the understanding of the charge recombination mechanism in the devices. When A is close to 1, the limiting recombination mechanism is the recombination in the charge neutral region. When A is close to 2, the limiting mechanism is the recombination in the space-charge region. Additional recombination mechanisms are incorporated when A is larger than 2 [94]. By considering ideality factor calculated from **Figure 23(b)**, as listed in **Table 6**, all three devices with different photoanode thickness have the value of A larger than 2 and the ideality factor is as high as 4.68 for the cell with 500 nm thick photoanode. The high diode quality factors illustrate that tunneling recombination for trapped charges is the significant recombination mechanism in the devices with hybrid nanoparticle/nanorod array photoanodes at selected thickness. ZnO nanoparticle surfaces and disordered P3HT

infiltrated into the mesoporous structure between nanorod arrays are full of defects that behave as traps for charges. Trapped electrons have higher chances of geminate recombination with trapped holes by tunneling back to the original molecules [96]. The value of A for the cells with 1200 nm nanorod arrays is relatively low among the three. The value of 2.04 is nearly to 2 and which suggests space-charge region recombination might be more significant than tunneling recombination in these devices. The balanced tradeoff relationship between light absorption capability and P3HT infiltrated depth might be the reason for low tunneling recombination. **Figure 23(c)** shows a semi-logarithmic plot of $J+J_{sc}$-GV against V-RJ. The value of J_o is again extracted from the plot and listed in **Table 6**. For the cells with shorter nanorod array length, 500 nm and 1200 nm, J_o is almost the same. While for the samples with 2600 nm nanorod arrays, J_o increases significantly by two orders of magnitude to 4.94×10^{-2} mA cm^{-2}. Overall J_o decrease is due to increased defect density and more carrier recombinations. Though the value of G from the devices based on 1200 nm nanorod arrays is not the lowest among the three cells, J_o is relatively low, and A and R are the lowest among three devices. It is rational to state that devices based on 1200 nm thick nanoparticle/nanorod array photoanodes gives the best performance, while the performance from 2600 nm thick cells are far behind the other two kinds of devices. And the analysis from diode parameters agrees with the results from J-V characteristics.

Table 6. List of diode parameters for hybrid nanoparticle/nanorod array based solid-state DSSCs with different nanorod lengths.

	G (mS cm^{-2})	A	R (Ω cm^2)	J$_o$ (mA cm^{-2})
500 nm	0.9	3.11	4.68	1.06x 10^{-4}
1200 nm	1.8	2.04	2.36	1.07x 10^{-4}
2400 nm	4.0	4.22	3.75	4.94x 10^{-2}

5.4 Conclusion

Solid-state DSSCs based on hybrid ZnO nanoparticle/nanorod array photoanodes with a mixture of mercurochrome and N3 dyes as the light absorbing material and P3HT as the hole transport material have been fabricated with the novel layer-by-layer process. The effect of the thickness of the hybrid ZnO photoanodes on device efficiency has been investigated. Devices based on 1200 nm thick hybrid photoanodes have the highest overall energy conversion efficiency: 0.64% in average, and 0.79% for the single best cell. It is believed that the tradeoff between light absorption and efficient charge (both electrons and holes) transport attributes to the relatively high efficiency for 1200 nm devices. Further investigation to find the optimized parameters for layer-by-layer deposition process could be beneficial to improve the efficiency of solid-state DSSCs based on hybrid ZnO photoanodes. Layer-by-layer deposition of ZnO nanoparticles and dye molecules is a reliable technique for conformal filling of ZnO nanorod arrays and for uniformly loading dye molecules throughout ZnO nanoparticle thin films. The technique described here can be easily extended to other semiconducting nanomaterials for solar cell applications.

6. ZNO AND CONJUGATED POLYMER BULK HETEROJUNCTION SOLAR CELLS CONTAINING ZNO NANOROD PHOTOANODE

6.1 Introduction

Organic solar cells are attractive alternatives to conventional inorganic photovoltaic devices because they can be fabricated on flexible substrates at low cost by solution processing. To overcome the short exciton diffusion length in most organic semiconductors, a bulk heterojunction (BHJ) structure has is widely used in organic solar cells. In BHJ cells, poly(3-hexylthiophene) (P3HT) and (6,6)-phenyl C_{61} butyric acid methyl ester (PCBM) are the most commonly used materials for electron donor and acceptor with a high power conversion efficiency of 5% [15-17]. Many inorganic semiconductors, such as TiO_2 [74, 102], ZnO [19, 51], and CdSe [23], have also been applied as electron acceptors. Although efficient charge separation is achieved by a large interfacial area between electron donor and acceptor, BHJ devices usually suffer from meandering or even discontinuous charge transport pathways [49]. In addition, the percolation network is susceptible to experimental processes and material properties, and thus difficult to achieve a reliable performance.

Creation of vertically aligned inorganic nanostructures with respect to the substrate is considered to be a potential approach to overcome the above problems. Ideally, vertically aligned nanostructures can be synthesized with an optimized dimension that is small enough for most of the excitons to diffuse through the interface between the inorganic and organic components. By controlling the dimension of the

vertically aligned nanostructure, polymer chains are also allowed to align themselves perpendicular to the substrate. The interchain coupling is thus improved, leading to better exciton diffusion and charge transport in conjugated polymer [72, 75, 76]. As for electrons, there is also a direct pathway to reach the electrode in vertically aligned nanostructures. Several groups have investigated hybrid solar cells with vertically aligned ZnO nanorod arrays (NRAs) as an efficient electron transport path, but the efficiencies are not comparable to P3HT and PCBM blends [22, 54-56]. One possible reason could be due to the spacing between ZnO NRAs being significantly larger than the exciton diffusion length of the conjugated polymer, which is reported to be 4-20 nm [4]. In order to overcome the large spacing between ZnO nanorods and dissociation of more photogenerated excitons, Olson *et al.* combined ZnO NRAs and BHJ thin films by blending PCBM into P3HT and utilized the BHJ thin film on top of the ZnO NRAs [22]. J_{sc} is thus increased significantly as compared to the device with ZnO NRAs/neat P3HT since excitons can be dissociated not only at the interface between P3HT and ZnO but also at the interface between P3HT and PCBM.

In this study, we report the preparation and characterization of ZnO NRA/BHJ solar cells at two different nanorod array lengths. Our strategy is to use ZnO nanoparticles (NPs) instead of PCBM due to the ease of ZnO synthesis and also its flexibility in morphology control [103]. The current density will be shown to have significantly increased by using ZnO NRAs and P3HT: ZnO NPs BHJ together. Furthermore, it will be shown that, with longer ZnO nanorods, the current density is also enhanced.

6.2 Experimental methods

6.2.1 Device fabrication

Cleaned fluorine-doped tin oxide glass substrates (FTO, 15 Ω/square) were coated with a thin layer of 5 nm ZnO NPs by drop-casting in methanol and annealed at 300°C for 10 min. Colloidal ZnO nanoparticles with a nearly uniform diameter of 5 nm were prepared by hydrolyzation process and the synthesis method has been previously reported elsewhere [85]. ZnO NRAs were grown by immersing seeded substrates in aqueous solution containing 0.05 M zinc nitrate hexahydrate ($Zn(NO_3)_2 \cdot 6H_2O$) and 0.05 M methenamine ($C_6H_{12}N_4$) at 90°C [29]. For 300 nm long NRAs, the growth time was 90 min. For 625 nm long nanorod arrays, the growth time was 120 min. After growth, the NRA thin films were rinsed with deionized water and dried in air at 90°C. ZnO NRAs were then sensitized in a 0.5 mM solution of mercurochrome in ethanol at room temperature for 30 min and then rinsed by ethanol to remove excess dyes. Regioregular P3HT was dissolved in 1,2-dichlorobenzene. A solution of P3HT: ZnO NP was prepared by equally mixing 40 mg ml^{-1} ZnO NPs in ethanol/1,2-dichlorobenzene (v/v=5:45) and 40 mg ml^{-1} P3HT in 1,2-dichlorobenzene. Mercurochrome-coated ZnO NPs were prepared by adding excess mercurochrome dyes to the ZnO colloidal solution. After overhight dye coating, the supernatant solution is removed with centrifugation, and precipitated mercurochrome-coated ZnO NPs were redispersed in ethanol/1,2-dichlorobenzene (v/v=5:45) with a concentration of 40 mg ml^{-1} in ethanol/1,2-dichlorobenzene. P3HT:mercurochrome:ZnO NP solution was prepared by blending 40 mg ml^{-1} mercurochrome and ZnO NP in ethanol/1,2-dichlorobenzene

(v/v=5:45) with 40 mg ml^{-1} P3HT in 1,2-dichlorobenzene. Two layers of P3HT were spin-coated onto mercurochrome-coated ZnO NRAs. Diluted P3HT with a concentration of 0.5 mg ml^{-1} in 1,2-dichlorobenzene was first pin-coated onto NRAs at 200 rpm, followed by the second spin-coating of P3HT onto the films with a concentration of 20 mg ml^{-1} at 800 rpm. P3HT: ZnO NP and P3HT: mercurochrome: ZnO NP solution were spin-coated on samples following the same procedure. After two spin-coatings, photovoltaic cells were annealed in a vacuum oven at 150°C for 30 min. Thermal evaporation of 100 nm thick gold was carried out in the last step to complete the device fabrication. The active area of the devices was 2.25 mm^{2}.

6.2.2 Solar cell characterization

The morphologies of the ZnO nanorod array NRAs were characterized by using field emission scanning electron microscopy (FE-SEM; JEOL JSM-7500F operated at 15 KeV). The photovoltaic performance of the fabricated devices was acquired when illuminated under a standard solar simulator at AM 1.5 condition (100 mW cm^{-2}).

6.3 Results and discussion

FE-SEM images of ZnO NRAs are shown in **Figure 24**. The thickness of the ZnO particulate seed layer for nanorod growth is about 100 nm. In **Figure 24(a)**, ZnO NRAs with 90 min growth have a diameter in the range of 40-50 nm, and are about 300 nm long. In **Figure 24(b)**, the diameters of the ZnO NRAs after 120 min growth are in the range of 45-55 nm, and the lengths of nanorods are about 625 nm. **Figure 25(a)**

presents the schematic of the hybrid solar cells. ZnO NRAs function as the electron acceptor and electron transporter. Mercurochrome dyes also serve dual functions: they enhance the wettability of the surface of ZnO NRs and thus improve the infiltration of P3HT into ZnO NRs. P3HT in this device architecture is the main light-absorbing material and the electron donor [54]. Other than P3HT, P3HT:ZnO NP BHJ and P3HT:mercurochrome:ZnO NP blends were also applied on top of the 300 nm and 625 nm long ZnO NRs. The energy band diagram of the FTO/ZnO/mercurochrome/ P3HT:ZnO/Au configuration is shown in **Figure 25(b)**.
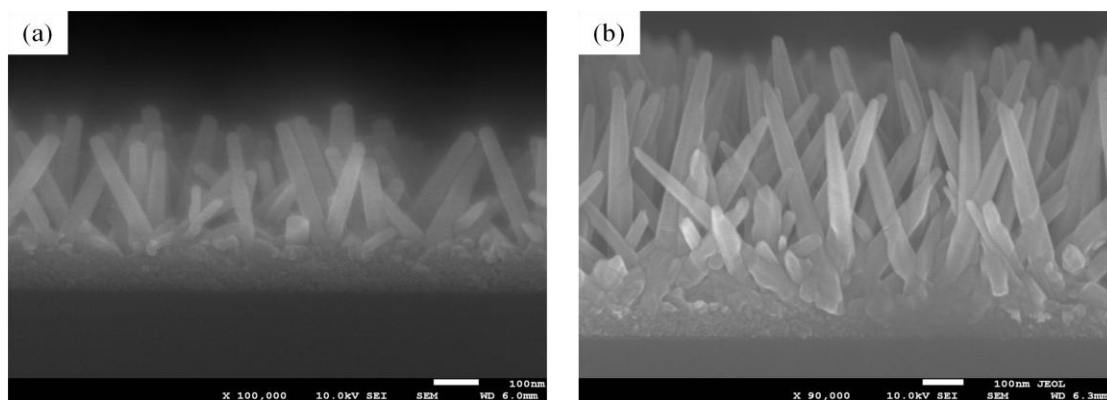
Figure 24. Cross-sectional FE-SEM images of (a) 300 nm and (b) 625 nm long ZnO nanorod arrays. (Scale bar: 100 nm.)
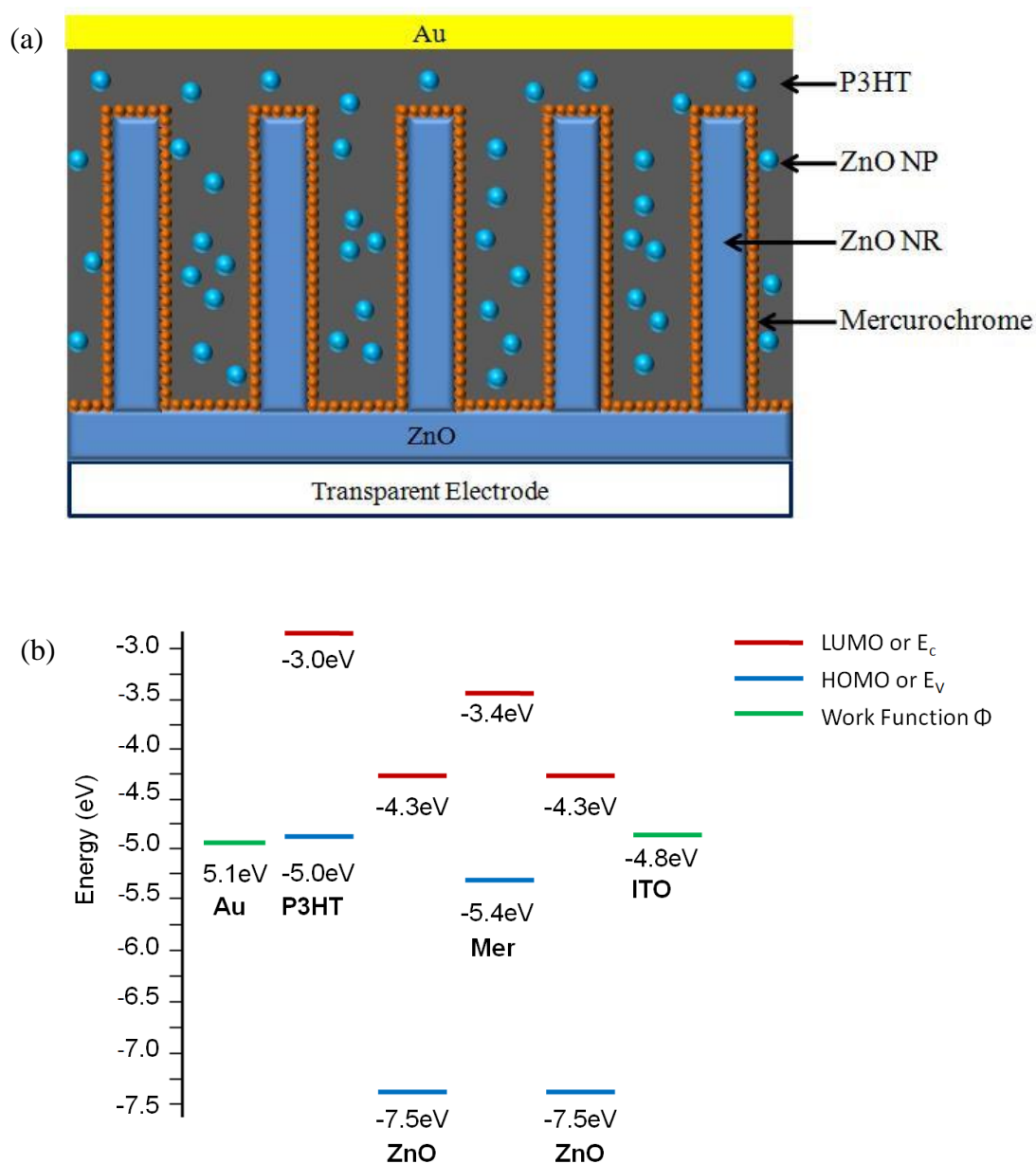
Figure 25. (a) Schematic of the proposed hybrid solar cell based on ZnO nanorod arrays. (b) Energy level diagram of the FTO/ZnO/mercurochrome/P3HT:ZnO/Au device.

Typical current density-voltage (J-V) curves of the hybrid photovoltaic devices were measured and plotted in **Figure 26**. **Table 7** summarizes the short-circuit current

densities (J_{sc}), the open-circuit voltages (V_{oc}), the fill factors (FF) and the power conversion efficiencies (η) for the devices prepared. When comparing the performance of the three cells based on 300 nm ZnO NRAs, J_{sc} increases significantly from 0.91 mA cm^{-2} to 2.20 mA cm^{-2} as the thin film changes from pure P3HT to P3HT:ZnO NP BHJ. The enhanced J_{sc} is attributed to a large interfacial area between P3HT and ZnO NPs, which results in the more photogenerated carriers. Thus, the large distance between the NRAs is overcome by using P3HT:ZnO BHJ instead of pure P3HT.
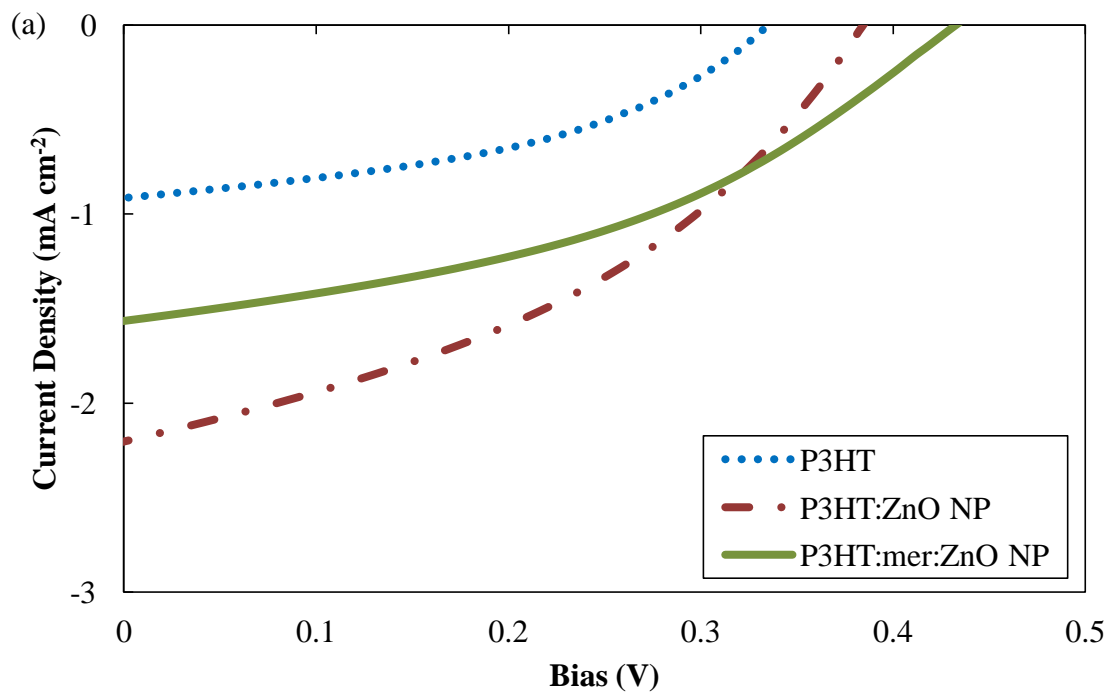
Figure 26. Current-voltage characteristics of devices based on (a) 300 nm and (b) 625 nm long ZnO nanorod arrays.
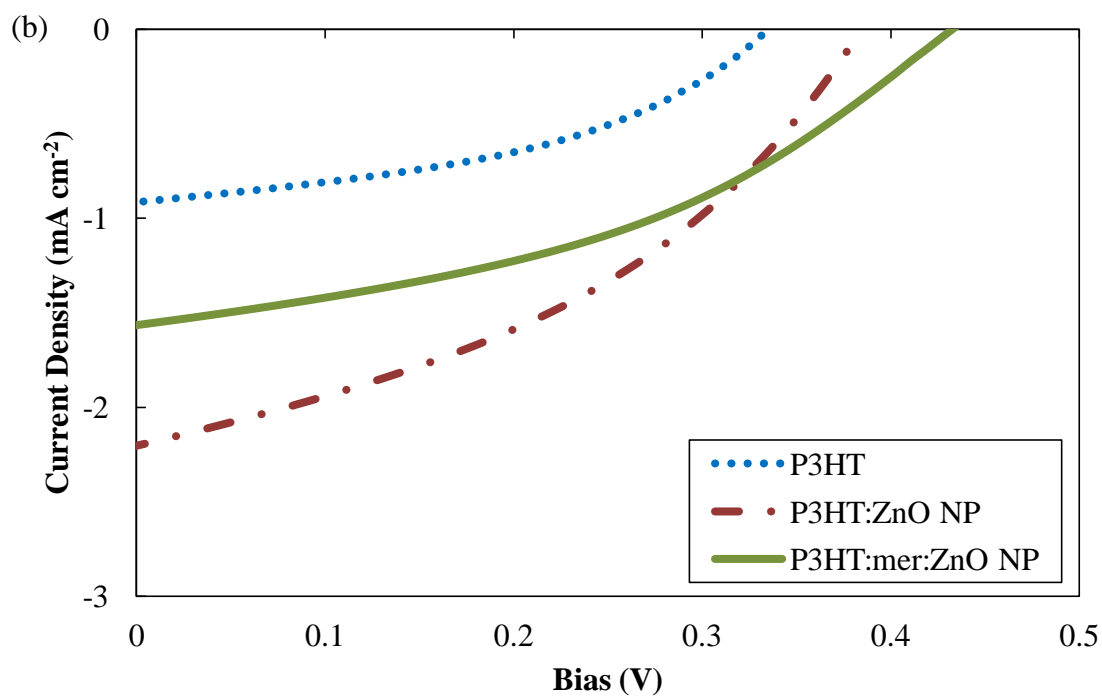
Figure 26. Continued.

Table 7. Device parameters of ZnO NR-based hybrid solar cells with different configurations.

Configuration	J_{sc} (mA cm^{-2})	V_{oc} (V)	FF	η (%)
300 nm ZnO NRAs/mer/P3HT	0.91	0.34	0.43	0.13
300 nm ZnO NRAs/mer/P3HT:ZnO NP	2.20	0.38	0.40	0.33
300 nm ZnO NRAs/mer/P3HT:mer:ZnO NP	1.56	0.43	0.41	0.27
625 nm ZnO NRAs/mer/P3HT	1.36	0.30	0.44	0.18
625 nm ZnO NRAs/mer/P3HT:ZnO NP	2.51	0.44	0.41	0.45
625 nm ZnO NRAs/mer/P3HT:mer:ZnO NP	1.56	0.40	0.46	0.28

It is noted that, when the composition of the thin film changes from P3HT:ZnO NP BHJ to P3HT:mercurochrome:ZnO NP, J_{sc} decreases from 2.20 mA cm^{-2} to 1.56 mA cm^{-2}. Even though the current density of P3HT: mercurochrome: ZnO NP is still higher than that of pure P3HT, it was expected that J_{sc} should be further enhanced with the addition of the dye molecules as compared to P3HT: ZnO NP BHJ. With mercurochrome dyes, the compatibility of P3HT and ZnO NPs should be improved [104]. The reason that leads to the drop of J_{sc} is still unknown. One of the possible explanations is that there might be phase segregation in P3HT:ZnO NP BHJ, while phase segregation is absent in P3HT:mercurochrome:ZnO NP BHJ due to the surfactant effect of the dye molecules. A certain level of phase segregation is generally regarded as beneficial to form a percolated network for charge transport in P3HT:PCBM solar cells. The same trend can be observed from the three devices with 625 nm long ZnO NRAs. When the composition of the thin film is P3HT, J_{sc} is enhanced from 0.91 mA cm^{-2} to 1.36 mA cm^{-2} with 49% improvement as the length of ZnO NRAs increases from 300 nm to 625 nm. In the case of P3HT:ZnO NP BHJ, J_{sc} is only improved by 14%. Finally, there is no current enhancement in the case of P3HT: mercurochrome: ZnO NP BHJ.

In general, with longer ZnO NRAs, more light can be absorbed by P3HT because each ZnO nanorod can function as an optical wvaguide to channel light deep into the device. When the thin film composition changes from P3HT to P3HT: ZnO NP BHJ, the major contributor of interfacial area between P3HT and ZnO changes from ZnO NRA/P3HT to P3HT/ZnO NP. By increasing the length of ZnO NRAs, the interfacial area between ZnO NRAs and P3HT can be increased. However, once the number of

excitons separated at the interface between ZnO NPs and P3HT is large enough, the length of ZnO NRAs is no longer a key factor in photocurrent generation. For both 300 nm and 625 nm ZnO NRAs, the lowest V_{oc} comes from the cell with pure P3HT due to a higher recombination rate resulting from the much larger spacing between ZnO NRAs as compared to the exciton diffusion length in P3HT. There is no obvious trend for V_{oc} observed in BHJ devices. The fill factors of all the devices lie between 0.40 and 0.46 without any significant variation among the devices. As a result, the device based on 625 nm ZnO NRAs and P3HT: ZnO NP BHJ has the highest energy conversion efficiency of 0.45%, followed by the device based on 300 nm ZnO NRAs and P3HT:ZnO NP BHJ with an efficiency of 0.33%.

Other than the well-accepted performance indicators, such as J_{sc}, V_{oc}, FF, and η, additional information about device characteristics can be extracted by analyzing J-V characteristics using the lumped circuit model for solar cells. A detailed procedure to find the diode parameters from measured J-V curve is described elsewhere.[94, 95] For a photovoltaic device under illumination, the current equation can be expressed as:

$$J=J_o \exp\left[\frac{q}{AkT}(V\text{-}RJ)\right]+GV\text{-}J_L \qquad (1)$$

where J and V are the diode current density and voltage, J_o is the diode reverse saturation current density, q is the electron charge, A is the diode quality factor, k is the Boltzmann constant, T is temperature, R is the series resistance, G is the shunt conductance, and J_L

is the photocurrent density. Diode parameters can be determined from the standard J-V curves shown in **Figure 26** and their values are shown in **Figure 27**.

For an efficient photovoltaic device, shunt conductance should be kept as small as possible. A smaller G corresponds to a smaller internal leakage of current through the cell. This internal leakage limits the FF of the cell. The value of G was extracted by plotting dJ/dV versus V in **Figure 27(a)** and the calculated values are listed in **Table 8**. Shunt conductance of the fabricated devices lies within 0.95 mS cm^{-2} to 2.30 mS cm^{-2}. The value of series resistance can be acquired by plotting dV/dJ vs $(J+J_{sc})^{-1}$ (**Figure 27(b)**). Similar to G, R should be as small as possible for an efficient device. From **Table 8**, both devices with ZnO NRAs/P3HT have lower series resistance.

The ideality factor A and the reverse saturation current J_o can facilitate the understanding of the charge recombination mechanism in the photovoltaic cells. As plotted in **Figure 27(b)** and listed in **Table 8**, the value of A increases with increasing NRA length and increases when the composition of the spin-coated thin film changed from P3HT, P3HT:ZnO NP, to P3HT:mercurochrome:ZnO NP. For all the cells, the ideality factor is larger than two. This means that, other than recombination in the charge neutral region and space-charge region, there are additional recombination mechanisms, such as geminate recombination, incorporated in the systems investigated [94]. The high ideality factor illustrates that geminate recombination for trapped charges is a significant recombination mechanism in the above devices.
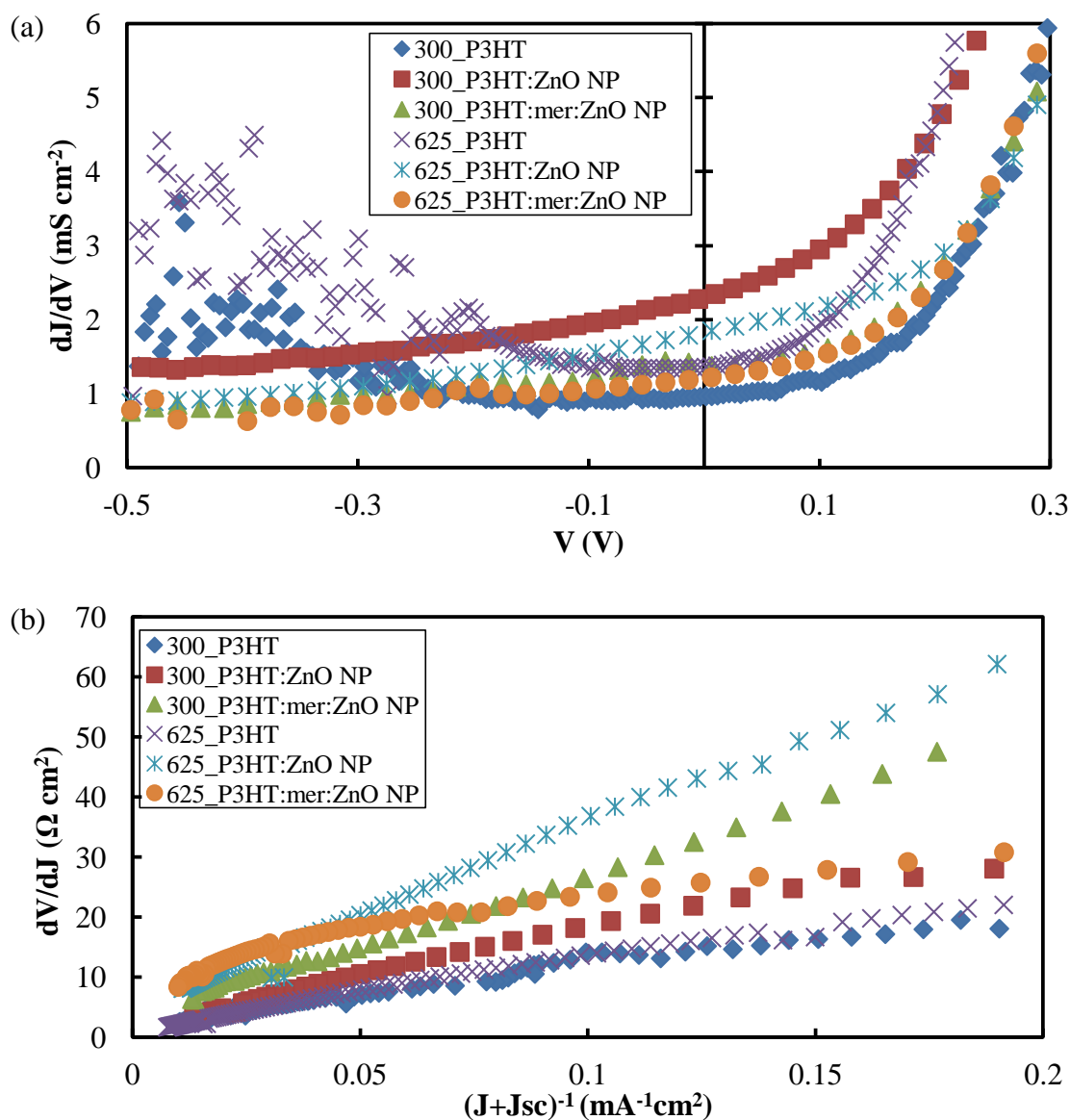
Figure 27. Diode parameters of hybrid solar cell based on 300 nm and 625 nm long ZnO nanorod arrays: (a) dJ/dV versus V for shunt conductance (G) characterization. (b) dV/dJ versus $(J+J_{sc})^{-1}$ for the determination of serious resistance(R) and diode ideality factor (A). (c) $J+J_{sc}$-GV versus V-RJ for the determination of reverse saturation current (J_o).
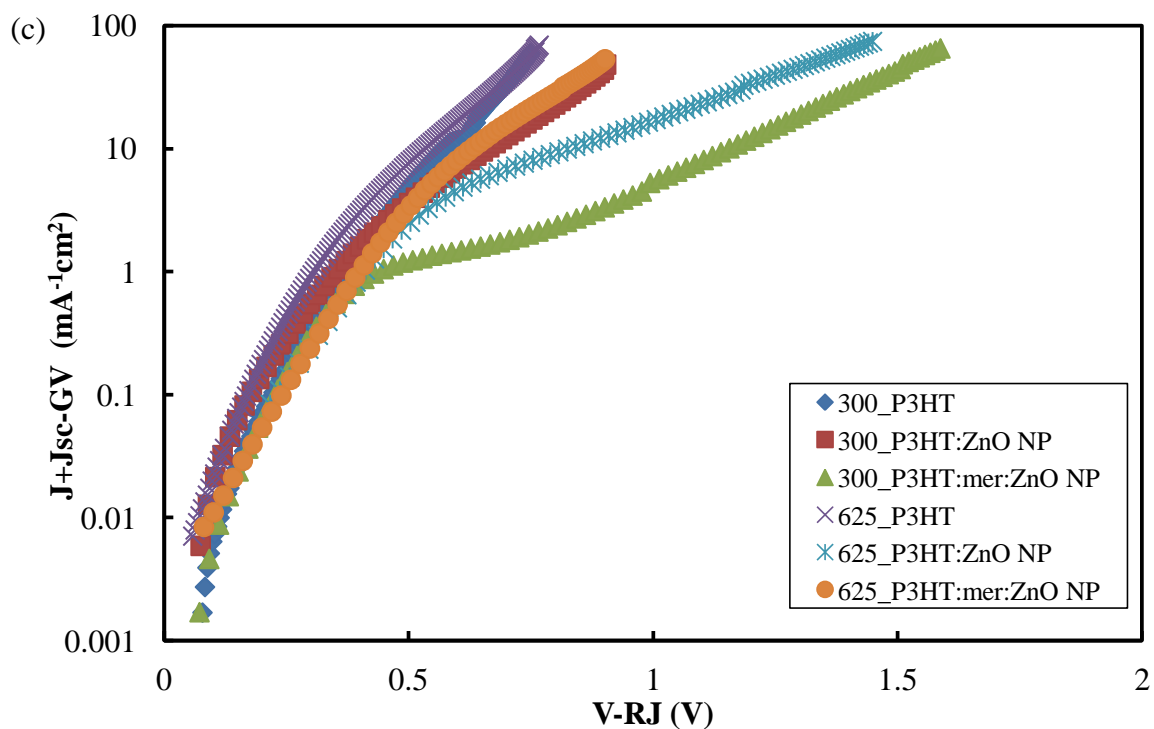
Figure 27. Continued.

Table 8. Diode parameters of ZnO NR-based hybrid solar cells with different configurations.

Configuration	G (mS cm^{-2})	A	R (Ω cm^2)	J$_o$ (mA cm^{-2})
300 nm ZnO NRAs/mer/P3HT	0.95	3.77	2.06	1.17x 10^{-2}
300 nm ZnO NRAs/mer/P3HT:ZnO NP	2.30	5.79	2.39	1.56x 10^{-1}
300 nm ZnO NRAs/mer/P3HT:mer:ZnO NP	1.36	9.07	3.78	8.19x 10^{-2}
625 nm ZnO NRAs/mer/P3HT	1.36	4.48	1.40	1.17x 10^{-1}
625 nm ZnO NRAs/mer/P3HT:ZnO NP	1.83	11.62	5.15	7.18x 10^{-1}
625 nm ZnO NRAs/mer/P3HT:mer:ZnO NP	1.20	13.56	5.52	5.36x 10^{-1}

ZnO surfaces and disordered P3HT are full of defects that behave as traps for charges. Trapped electrons have higher chances of geminate recombination with trapped holes by tunneling back to the original molecules [96]. In BHJ structures, the formation of ZnO enclaves that are completely surrounded by P3HT exacerbates the geminate recombination issue because electrons trapped on ZnO cannot be transported to the electrode and eventually lost by recombination. Similar to P3HT: PCBM BHJs, some level of phase segregation is highly desirable for improving device efficiency. The mercurochrome-coated ZnO NPs can be well dispersed in P3HT, but the inability to form phase-segregated structures results in all ZnO NPs being well dispersed in P3HT. This yields a much higher level of charge recombination, and hence exceptionally high diode ideality factor. The increase of the ideality factor with the length of the ZnO NRAs and with the better dispersion of ZnO in P3HT, as shown in **Table 8**, agrees well with the increased charge recombinations in those devices. The device's reverse saturation current can be extracted from **Figure 27(c)**, a semi-logarithmic plot of $J + J_{sc}$–GV against V–RJ. For all devices, J_o is of the order of 10^{-1}–10^{-2}. These values are quite large due to a very high level of carrier recombination. From the analysis of the diode parameters, it is suggested that the major causes of low energy efficiency in those solar cells are due to the high level of exciton and carrier recombinations, which comes from the short exciton diffusion length, the surface defects of ZnO and the formation of ZnO enclaves in P3HT. In order to achieve better efficiency using ZnO BHJs, a certain degree of phase segregation is preferred to form a percolated network, which can potentially be achieved by several techniques. For example, synthesizing branched ZnO nanorods can

improve interconnectivity and ball milling of ZnO nanoparticles can form small irregularly shaped aggregates. Balancing between the dispersion of ZnO in P3HT and the formation of a percolation pathway may eventually yield efficient and stable BHJ solar cells.

6.4 Conclusion

Bulk heterojunction hybrid solar cells based on ZnO and P3HT in conjunction with two different lengths of the ZnO NRA photoanode have been fabricated. The effects of the length of the ZnO NRAs and the composition of the spin-coated thin films have been investigated. In general, the short-circuit current increases with the length of the ZnO NRAs due to increased light absorption through the waveguide effect from nanowires and an increased interfacial area between ZnO and P3HT. By adding ZnO NPs into P3HT to form BHJs, the effect of the length of the ZnO NRAs on the device performance decreases. The short-circuit current is higher in the P3HT: ZnO NP BHJ device than the pure P3HT device. The highest η achieved in this study is 0.45% based on 625 nm ZnO NRAs/mercurochrome/P3HT: ZnO NP BHJ. Coating ZnO NPs with mercurochrome can improve the mixing of ZnO and P3HT, but the inability to form a phase segregated structure leads to high geminate recombination of photogenerated carriers. Analysis from diode parameters shows the values of A and Jo in all devices are too high due to the high level of carrier recombination. This suggests that further quantitative investigation is needed on charge trapping surface defects from the ZnO

surface and high carrier recombination rates from various mechanisms in the proposed device.

7. CONCLUSION

Excitonic solar cells are up-and-coming alternatives to conventional inorganic photovoltaic devices due to its potential to be fabricated on flexible substrates at extremely low cost. In XSCs, polymers, small molecules, or quantum dots are utilized as the light absorbing materials. Upon light absorption, excitons are generated in the material, but only those excitons generated within the order of the exciton diffusion length (4-20 nm) from the interface have chances to reach the interface and separate into free charges. In other words, it is beneficial to fabricate excitonic devices with interface everywhere in the material. Many approaches have been explored to investigate and promote the device performance of the solid-state XSCs. Most of these aim to create a large interfacial area between p-type and n-type materials by creating a bulk heterojunction structure. In addition, bulk heterojunction structure ensures short exciton diffusion ranges and offers percolated pathways for both electrons and holes to reach relevant electrodes. Morphologies of active layers can be divided into four categories: 1. planar metal oxide and conjugated polymer bilayer; 2. filling nanoporous metal oxides with conjugated polymers; 3. metal oxide nanoparticles and conjugated polymer hybrid solar cells, including in-situ growth of metal oxides; 4. vertically-aligned metal oxide nanostructures with conjugated polymers. By modifying the morphology of the inorganic constituent in HSCs and DSSCs, the photovoltaic efficiency could be improved. As the key components, many inorganic semiconductors have been applied as nanostructured materials for XSCs. Among those electron transport materials, ZnO is a

competitive candidate because it can be synthesized into all the needed morphologies by solution process.

First of all, covering a compact and planar layer of semiconductor oxide such as ZnO with a thin layer of polymer is the most direct and the simplest method to fabricate HSCs. The advantage of the device architecture is that photogenerated charges can be collected by the electrodes easily due to direct pathways. Oppositely, the relatively small interfacial area between metal oxide and polymer limits the charge carrier generation. The interfacial surface area between the p-type and n-type materials can be increased by replacing the compact metal film with a nanoporous one. By filling these interstitial voids of the porous film with a conjugated polymer, exciton harvesting is improved as more excitons are generated within 4-20 nm of the ZnO/polymer interface. In this dissertation, in order to not only overcome the short exciton diffusion length of conjugated polymer, but also improve the hole transport capability in the system, solid-state DSSCs consisting of dye-coated ZnO nanoparticle photoanode and P3HT thin film were fabricated with the addition of XDSWNT into P3HT. The amount of the XDSWNT in P3HT and the device performance of the cells were investigated. The overall energy conversion efficiency achieved in this work was 0.023% with pristine P3HT. With the addition of XDSWNT into P3HT, though open-circuit voltage dropped slightly, short-circuit current increased by several times. By having a weight ratio of XDSWNT and P3HT at 0.1:1, the short-circuit current was quadrupled and the device efficiency was tripled to reach 0.07%, compared to devices without the addition of XDSWNT. However, the efficiency of these ZnO-based solid-state DSSCs was still low.

One of the possible reasons is poor infiltration of P3HT into ZnO nanoparticle thin films. Another major drawback is that semiconducting particle surfaces have a tendency to form defects which operate as electron trapping centers. Since trapping/detrapping events are inevitable when electrons diffuse through the disordered nanoparticle network,[86-88] it is necessary to alter the morphology of the photoanode and design a relatively direct electron transport pathway to improve electron collection.

Creating vertically-aligned metal oxide nanostructures with respect to the substrate is considered to be a potential approach to overcome the problems encountered in the nanoparticle-based devices. Ideally, vertically-aligned metal oxide nanostructures can be synthesized with optimized dimension that is small enough for most of the excitons to reach the junction between inorganic and organic components; at the same time, this small enough dimension does not hinder the filling of the polymer into the nanostructures. By controlling the dimension of the vertically-aligned nanostructure, polymer chains are also allowed to align themselves perpendicular to the substrate. The interchain coupling is thus improved and leads to better exciton diffusion and charge transport in polymer. As for electrons, there is a more direct pathway to reach the electrode in nanorods than in porous nanoparticle thin films; in addition, nanorods provide fewer defect sites to trap electrons as compared to nanoparticles. With a more direct pathway and fewer trapping sites, electron transport in nanorods is tens to hundreds of times faster than that in the nanoparticle thin films. Efficient electron transport helps minimize electron transit time from the point of generation to the electrode, thus lowering the recombination loss of the electrons. However, ZnO

photoanodes based on nanorod arrays suffer from limited surface area that can absorb dye molecules for efficient light harvesting when compared to the electrodes based on nanoparticles.

In this dissertation research, we fabricated solid-state DSSCs with hybrid ZnO nanoparticle/nanorod array photoanodes and investigated the influence of the morphology of ZnO nanorods to the photovoltaic performance. By filling the interstitial space between nanorods with 5 nm size ZnO nanoparticles, the total surface area of ZnO photoanodes can be greatly increased. Light absorption of the device can thus be increased without compromising efficient electron transport of ZnO nanorod arrays. Furthermore, compared to more than thousand times of hopping in a particulate thin film, electrons injected from dye molecules into nanoparticles can reach ZnO nanorods, and then the electrode, just by hopping across a few nanoparticles. By minimizing the number of interparticle hoppings, the carrier recombination can be greatly reduced. As expected, short-circuit current increased with the amount of ZnO nanoparticles in the photoanode due to the large surface area for dye loading. Compared to pure nanoparticle photoanode, V_{oc} increased with the presence of ZnO nanorod arrays due to faster electron transport and less charge recombination. The overall conversion efficiency of the solid-state DSSC based on ZnO nanorod arrays was 0.13%. By fully filling the interstitial voids of the nanorod arrays with nanoparticles, the device efficiency increased significantly to 0.34%. Analysis from diode parameters shows the values of the diode ideality factor and the J_o decreased in devices based on the hybrid ZnO

photoanodes. This suggests that devices based on hybrid ZnO photoanodes have lower charge recombinations.

After the study of morphology of hybrid nanoparticle/nanorod array photoanode and the corresponding device performance, the influence of the length of nanorod arrays was also investigated. ZnO nanoparticles were still filled into the interstitial space between nanorod arrays, but by a novel layer-by-layer deposition method. Devices based on 1200 nm thick hybrid photoanodes had the highest overall energy conversion efficiency, 0.64 % in average, and 0.79 % for the single best cell. It is believed that the tradeoff relationship between the light absorption capability and the efficient hole transport ability attributes to the relatively large η for 1200 nm devices. Analysis from diode parameters also agrees that among 500 nm, 1200 nm, and 2600 nm devices, photovoltaic devices based on 1200 nm thick photoanodes have the best properties. Other than efficiency, the novel layer-by-layer deposition of ZnO nanoparticles and dye molecules is a reliable technique for conformal filling of ZnO nanorod arrays and for uniformly loading dye molecules throughout ZnO nanoparticle thin films. The technique described here can be easily extended to other semiconducting nanomaterials for solar cell applications.

Another approach utilized in this dissertation to promote the cell efficiency from device performance was to for a bulk heterojuction structure by blending ZnO nanoparticles with P3HT. Several groups have investigated the devices with vertically aligned ZnO nanorod arrays as efficient electron transport path while the efficiencies are not competitive to OSCs based on P3HT: PCBM thin film. One possible reason could be

due to the spacing between ZnO nanorod arrays is larger than the exciton diffusion length of the conjugated polymer. In order to overcome the large spacing between ZnO nanorods and dissociate more photogenerated excitons, HSCs based on two different lengths of ZnO nanorod arrays with mercurochrome as surface modifier and P3HT as light absorbing and hole transporting material have been fabricated. In general, short-circuit current increases with the length of ZnO nanorod arrays due to increased interfacial area between ZnO and P3HT, though by adding ZnO nanoparticles into P3HT, the effect of the length of ZnO nanorod arrays on the device performance decreases. Short-circuit current also increases when the spin-coated thin film is composed of P3HT: ZnO nanoparticle bulk hetorejunction instead of pure P3HT due to enhanced interfacial area. The highest η achieved in this dissertation is 0.45 % based on 625 nm ZnO nanorod arrays/mercurochrome/P3HT: ZnO nanoparticle bulk heterojunction.

As a summary, several approaches have been explored to investigate and enhance device performance of solid-state XSCs. The photovoltaic efficiency has been significantly improved by modifying the morphology of the device. In addition, the novel layer-by-layer deposition of ZnO nanoparticles and dye molecules is a reliable technique which can be easily extended to other semiconducting nanomaterials for solar cell applications. The approaches developed in this thesis work can be easily extended to other semiconducting nanomaterials and organic semiconductors for further efficiency improvement.

REFERENCES

[1]   Hochbaum A I and Yang P D 2010 Semiconductor nanowires for energy

        conversion *Chem. Rev.* **110** 527-46

[2]   Gregg B A 2003 Excitonic solar cells *J. Phys. Chem. B* **107** 4688-98

[3]   Gledhill S E, Scott B and Gregg B A 2005 Organic and nano-structured

        composite photovoltaics: an overview *J. Mater. Res.* **20** 3167-79

[4]   Coakley K M and McGehee M D 2004 Conjugated polymer photovoltaic cells

        Chem. Mat. **16** 4533-42

[5]   Peumans P, Yakimov A and Forrest S R 2003 Small molecular weight organic

        thin-film photodetectors and solar cells *J. Appl. Phys.* **93** 3693-723

[6]   Gratzel M 2000 Perspectives for dye-sensitized nanocrystalline solar cells *Prog.*

        Photovoltaics **8** 171-85

[7]   Nazeeruddin M K, Kay A, Rodicio I, Humphrybaker R, Muller E, Liska P,

        Vlachopoulos N and Gratzel M 1993 Conversion of light to electricity by

        cis-X_2bis(2,2'-bipyridyl-4,4'-dicarboxylate)ruthenium(II) charge-transfer

        sensitizers (X = Cl$^-$, Br$^-$, I$^-$, CN$^-$, and SCN$^-$) on nanocrystalline TiO_2 electrodes

        J. Am. Chem. Soc. **115** 6382-90

[8]   Oregan B and Gratzel M 1991 A low-cost, high-efficiency solar-cell based on

        dye-sensitized colloidal TiO_2 films *Nature* **353** 737-40

[9]   Gratzel M 2003 Dye-sensitized solar cells *J. Photochem. Photobiol.*

        C-Photochem. Rev. **4** 145-53

[10]   Sinke W C and Wienk M M 1998 Photochemistry - solid-state organic solar

         cells *Nature* **395** 544-5

[11]   Bach U, Lupo D, Comte P, Moser J E, Weissortel F, Salbeck J, Spreitzer H and

         Gratzel M 1998 Solid-state dye-sensitized mesoporous TiO$_2$ solar cells with

         high photon-to-electron conversion efficiencies *Nature* **395** 583-5

[12]   Kruger J, Plass R, Cevey L, Piccirelli M, Gratzel M and Bach U 2001 High

         efficiency solid-state photovoltaic device due to inhibition of interface charge

         recombination *Appl. Phys. Lett.* **79** 2085-7

[13]   Lee T H, Sun D Z, Zhang X, Sue H J and Cheng X 2009 Solid-state

         dye-sensitized solar cell based on semiconducting nanomaterials *J. Vac. Sci.*

         Technol. B **27** 3073-7

[14]   Schmidt-Mende L, Zakeeruddin S M and Gratzel M 2005 Efficiency

         improvement in solid-state-dye-sensitized photovoltaics with an amphiphilic

         ruthenium-dye *Appl. Phys. Lett.* **86** 013504

[15]   Li G, Shrotriya V, Huang J S, Yao Y, Moriarty T, Emery K and Yang Y 2005

         High-efficiency solution processable polymer photovoltaic cells by

         self-organization of polymer blends *Nat. Mater.* **4** 864-8

[16]   Padinger F, Rittberger R S and Sariciftci N S 2003 Effects of postproduction

         treatment on plastic solar cells *Adv. Funct. Mater.* **13** 85-8

[17]   Reyes-Reyes M, Kim K and Carroll D L 2005 High-efficiency photovoltaic

         devices based on annealed poly(3-hexylthiophene) and

1-(3-methoxycarbonyl)-propyl-1-phenyl-(6,6)C-61 blends *Appl. Phys. Lett.* **87** 083506

[18]   Liang Y Y, Xu Z, Xia J B, Tsai S T, Wu Y, Li G, Ray C and Yu L P 2010 For the bright future-bulk heterojunction polymer solar cells with power conversion efficiency of 7.4% *Adv. Mater.* **22** E135-8

[19]   Beek W J E, Wienk M M and Janssen R A J 2004 Efficient hybrid solar cells from zinc oxide nanoparticles and a conjugated polymer *Adv. Mater.* **16** 1009-13

[20]   Baxter J B and Aydil E S 2006 Dye-sensitized solar cells based on semiconductor morphologies with ZnO nanowires *Sol. Energy Mater. Sol. Cells* **90** 607-22

[21]   Zhang Q F, Chou T R, Russo B, Jenekhe S A and Cao G Z 2008 Aggregation of ZnO nanocrystallites for high conversion efficiency in dye-sensitized solar cells *Angew. Chem.-Int. Edit.* **47** 2402-6

[22]   Olson D C, Piris J, Collins R T, Shaheen S E and Ginley D S 2006 Hybrid photovoltaic devices of polymer and ZnO nanofiber composites *Thin Solid Films* **496** 26-9

[23]   Huynh W U, Dittmer J J and Alivisatos A P 2002 Hybrid nanorod-polymer solar cells *Science* **295** 2425-7

[24]   Watt A A R, Blake D, Warner J H, Thomsen E A, Tavenner E L, Rubinsztein-Dunlop H and Meredith P 2005 Lead sulfide nanocrystal: conducting polymer solar cells *J. Phys. D-Appl. Phys.* **38** 2006-12

[25]   McDonald S A, Konstantatos G, Zhang S G, Cyr P W, Klem E J D, Levina L

         and Sargent E H 2005 Solution-processed PbS quantum dot infrared

         photodetectors and photovoltaics *Nat. Mater.* **4** 138-42

[26]   Panthani M G, Akhavan V, Goodfellow B, Schmidtke J P, Dunn L,

         Dodabalapur A, Barbara P F and Korgel B A 2008 Synthesis of $CuInS_2$,

         $CuInSe_2$, and $Cu(In_xGa_{1-x})Se_2$ (CIGS) nanocrystal "inks" for printable

         photovoltaics *J. Am. Chem. Soc.* **130** 16770-7

[27]   Haase M, Weller H and Henglein A 1988 Photochemistry and radiation

         chemistry of colloidal semiconductors. 23. Electron storage on ZnO particles

         and size quantization *J. Phys. Chem.* **92** 482-7

[28]   Pacholski C, Kornowski A and Weller H 2002 Self-assembly of ZnO: from

         nanodots, to nanorods *Angew. Chem.-Int. Edit.* **41** 1188-91

[29]   Guo M, Diao P and Cai S M 2005 Hydrothermal growth of well-aligned ZnO

         nanorod arrays: dependence of morphology and alignment ordering upon

         preparing conditions *J. Solid State Chem.* **178** 1864-73

[30]   Law M, Greene L E, Johnson J C, Saykally R and Yang P D 2005 Nanowire

         dye-sensitized solar cells *Nat. Mater.* **4** 455-9

[31]   Greene L E, Law M, Yuhas B D and Yang P D 2007 ZnO-TiO_2 core-shell

         nanorod/P3HT solar cells *J. Phys. Chem. C* **111** 18451-6

[32]   Yu X L, Song J G, Fu Y S, Xie Y, Song X, Sun J and Du X W 2010 ZnS/ZnO

         heteronanostructure as photoanode to enhance the conversion efficiency of

         dye-sensitized solar cells *J. Phys. Chem. C* **114** 2380-4

[33]   Yu H D, Zhang Z P, Han M Y, Hao X T and Zhu F R 2005 A general

         low-temperature route for large-scale fabrication of highly oriented ZnO

         nanorod/nanotube arrays *J. Am. Chem. Soc.* **127** 2378-9

[34]   Wang X D, Ding Y, Summers C J and Wang Z L 2004 Large-scale synthesis of

         six-nanometer-wide ZnO nanobelts *J. Phys. Chem. B* **108** 8773-7

[35]   Hosono E, Fujihara S, Honna I and Zhou H S 2005 The fabrication of an

         upright-standing zinc oxide nanosheet for use in dye-sensitized solar cells *Adv.*

         Mater. **17** 2091-4

[36]   Jiang C Y, Sun X W, Lo G Q, Kwong D L and Wang J X 2007 Improved

         dye-sensitized solar cells with a ZnO-nanoflower photoanode *Appl. Phys. Lett.*

         90 263501

[37]   Wang Z L 2004 Zinc oxide nanostructures: growth, properties and applications

         J. Phys.-Condes. Matter **16** R829-58

[38]   Quintana M, Edvinsson T, Hagfeldt A and Boschloo G 2007 Comparison of

         dye-sensitized ZnO and TiO2 solar cells: studies of charge transport and carrier

         lifetime *J. Phys. Chem. C* **111** 1035-41

[39]   Martinson A B F, Goes M S, Fabregat-Santiago F, Bisquert J, Pellin M J and

         Hupp J T 2009 Electron transport in dye-sensitized solar cells based on ZnO

         nanotubes: evidence for highly efficient charge collection and exceptionally

         rapid dynamics *J. Phys. Chem. A* **113** 4015-21

[40]   Lira-Cantu M and Krebs F C 2006 Hybrid solar cells based on MEH-PPV and

         thin film semiconductor oxides (TiO_2, Nb_2O_5, ZnO, CeO_2 and CeO_2-TiO_2):

performance improvement during long-time irradiation *Sol. Energy Mater. Sol. Cells* **90** 2076-86

[41]   Olson D C, Shaheen S E, White M S, Mitchell W J, van Hest M, Collins R T and Ginley D S 2007 Band-offset engineering for enhanced open-circuit voltage in polymer-oxide hybrid solar cells *Adv. Funct. Mater.* **17** 264-9

[42]   Monson T C, Lloyd M T, Olson D C, Lee Y J and Hsu J W P 2008 Photocurrent enhancement in polythiophene- and alkanethiol-modified ZnO solar cells *Adv. Mater.* **20** 4755-9

[43]   Boucle J, Snaith H J and Greenham N C 2010 Simple approach to hybrid polymer/porous metal oxide solar cells from solution-processed ZnO nanocrystals *J. Phys. Chem. C* **114** 3664-74

[44]   Boucharef M, Di Bin C, Boumaza M S, Colas M, Snaith H J, Ratier B and Boucle J 2010 Solid-state dye-sensitized solar cells based on ZnO nanocrystals *Nanotechnology* **21** 205203

[45]   Beek W J E, Wienk M M, Kemerink M, Yang X N and Janssen R A J 2005 Hybrid zinc oxide conjugated polymer bulk heterojunction solar cells *J. Phys. Chem. B* **109** 9505-16

[46]   Beek W J E, Wienk M M and Janssen R A J 2006 Hybrid solar cells from regioregular polythiophene and ZnO nanoparticles *Adv. Funct. Mater.* **16** 1112-6

[47]   Wong H M P, Wang P, Abrusci A, Svensson M, Andersson M R and
        Greenham N C 2007 Donor and acceptor behavior in a polyfluorene for
        photovoltaics *J. Phys. Chem. C* **111** 5244-9

[48]   Han Z Y, Zhang J C, Yang X Y, Zhu H and Cao W L 2010 Synthesis and
        photoelectric property of poly (3-octylthiophene)/zinc oxide complexes *Sol.
        Energy Mater. Sol. Cells* **94** 194-200

[49]   Oosterhout S D, Wienk M M, van Bavel S S, Thiedmann R, Koster L J A,
        Gilot J, Loos J, Schmidt V and Janssen R A J 2009 The effect of
        three-dimensional morphology on the efficiency of hybrid polymer solar cells
        Nat. Mater. **8** 818-24

[50]   Ji L W, Shih W S, Fang T H, Wu C Z, Peng S M and Meen T H 2010
        Preparation and characteristics of hybrid ZnO-polymer solar cells *J. Mater. Sci.*
        45 3266-9

[51]   Beek W J E, Slooff L H, Wienk M M, Kroon J M and Janssen R A J 2005
        Hybrid solar cells using a zinc oxide precursor and a conjugated polymer *Adv.
        Funct. Mater.* **15** 1703-7

[52]   Moet D J D, Koster L J A, de Boer B and Blom P W M 2007 Hybrid polymer
        solar cells from highly reactive diethylzinc: MDMO-PPV versus P3HT *Chem.
        Mat.* **19** 5856-61

[53]   Lin Y Y, Lee Y Y, Chang L W, Wu J J and Chen C W 2009 The influence of
        interface modifier on the performance of nanostructured ZnO/polymer hybrid
        solar cells *Appl. Phys. Lett.* **94** 063308

[54]   Ravirajan P, Peiro A M, Nazeeruddin M K, Graetzel M, Bradley D D C,
         Durrant J R and Nelson J 2006 Hybrid polymer/zinc oxide photovoltaic devices
         with vertically oriented ZnO nanorods and an amphiphilic molecular interface
         layer *J. Phys. Chem. B* **110** 7635-9

[55]   Peiro A M, Ravirajan P, Govender K, Boyle D S, O'Brien P, Bradley D D C,
         Nelson J and Durrant J R 2006 Hybrid polymer/metal oxide solar cells based
         on ZnO columnar structures *J. Mater. Chem.* **16** 2088-96

[56]   Olson D C, Lee Y J, White M S, Kopidakis N, Shaheen S E, Ginley D S, Voigt
         J A and Hsu J W P 2007 Effect of polymer processing on the performance of
         poly(3-hexylthiophene)/ZnO nanorod photovoltaic devices *J. Phys. Chem. C*
         111 16640-5

[57]   Olson D C, Lee Y J, White M S, Kopidakis N, Shaheen S E, Ginley D S, Voigt
         J A and Hsu J W P 2008 Effect of ZnO processing on the photovoltage of
         ZnO/poly(3-hexylthiophene) solar cells *J. Phys. Chem. C* **112** 9544-7

[58]   Unalan H E, Hiralal P, Kuo D, Parekh B, Amaratunga G and Chhowalla M
         2008 Flexible organic photovoltaics from zinc oxide nanowires grown on
         transparent and conducting single walled carbon nanotube thin films *J. Mater.
         Chem.* **18** 5909-12

[59]   Lee Y-J, Lloyd M T, Olson D C, Grubbs R K, Lu P, Davis R J, Voigt J A and
         Hsu J W P 2009 Optimization of ZnO Nanorod Array Morphology for Hybrid
         Photovoltaic Devices *The Journal of Physical Chemistry C* **113** 15778-82

[60]   Briseno A L, Holcombe T W, Boukai A I, Garnett E C, Shelton S W, Frechet J

J M and Yang P D 2010 Oligo- and polythiophene/ZnO hybrid nanowire solar

cells *Nano Lett.* **10** 334-40

[61]   Takanezawa K, Hirota K, Wei Q S, Tajima K and Hashimoto K 2007 Efficient

charge collection with ZnO nanorod array in hybrid photovoltaic devices *J.*

Phys. Chem. C **111** 7218-23

[62]   Takanezawa K, Tajima K and Hashimoto K 2008 Efficiency enhancement of

polymer photovoltaic devices hybridized with ZnO nanorod arrays by the

introduction of a vanadium oxide buffer layer *Appl. Phys. Lett.* **93** 063308

[63]   Kline R J, McGehee M D and Toney M F 2006 Highly oriented crystals at the

buried interface in polythiophene thin-film transistors *Nat. Mater.* **5** 222-8

[64]   Gratzel M 2001 Photoelectrochemical cells *Nature* **414** 338-44

[65]   Keis K, Magnusson E, Lindstrom H, Lindquist S E and Hagfeldt A 2002 A 5%

efficient photo electrochemical solar cell based on nanostructured ZnO

electrodes *Sol. Energy Mater. Sol. Cells* **73** 51-8

[66]   Keis K, Vayssieres L, Rensmo H, Lindquist S E and Hagfeldt A 2001

Photoelectrochemical properties of nano- to microstructured ZnO electrodes *J.*

Electrochem. Soc. **148** A149-55

[67]   Coakley K M and McGehee M D 2003 Photovoltaic cells made from

conjugated polymers infiltrated into mesoporous titania *Appl. Phys. Lett.* **83**

3380-2

[68]   Bartholomew G P and Heeger A J 2005 Infiltration of regioregular poly 2,2

'-(3-hexylthiopene) into random nanocrystalline TiO$_2$ networks *Adv. Funct.*

Mater. **15** 677-82

[69]   Snaith H J, Humphry-Baker R, Chen P, Cesar I, Zakeeruddin S M and Gratzel

M 2008 Charge collection and pore filling in solid-state dye-sensitized solar

cells *Nanotechnology* **19** 424003

[70]   Milliron D J, Gur I and Alivisatos A P 2005 Hybrid organic - nanocrystal solar

cells *MRS Bull.* **30** 41-4

[71]   Yang X N, Loos J, Veenstra S C, Verhees W J H, Wienk M M, Kroon J M,

Michels M A J and Janssen R A J 2005 Nanoscale morphology of

high-performance polymer solar cells *Nano Lett.* **5** 579-83

[72]   Sirringhaus H, Brown P J, Friend R H, Nielsen M M, Bechgaard K,

Langeveld-Voss B M W, Spiering A J H, Janssen R A J, Meijer E W, Herwig P

and de Leeuw D M 1999 Two-dimensional charge transport in self-organized,

high-mobility conjugated polymers *Nature* **401** 685-8

[73]   Rhodes R, Horie M, Chen H, Wang Z, Turner M L and Saunders B R 2010

Aggregation of zinc oxide nanoparticles: from non-aqueous dispersions to

composites used as photoactive layers in hybrid solar cells *J. Colloid Interface*

Sci. **344** 261-71

[74]   van Hal P A, Wienk M M, Kroon J M, Verhees W J H, Slooff L H, van Gennip

W J H, Jonkheijm P and Janssen R A J 2003 Photoinduced electron transfer

and photovoltaic response of a MDMO-PPV : TiO_2 bulk-heterojunction *Adv. Mater.* **15** 118-21

[75]   Coakley K M, Liu Y X, McGehee M D, Frindell K L and Stucky G D 2003 Infiltrating semiconducting polymers into self-assembled mesoporous titania films for photovoltaic applications *Adv. Funct. Mater.* **13** 301-6

[76]   Coakley K M, Srinivasan B S, Ziebarth J M, Goh C, Liu Y X and McGehee M D 2005 Enhanced hole mobility in regioregular polythiophene infiltrated in straight nanopores *Adv. Funct. Mater.* **15** 1927-32

[77]   Martinson A B F, McGarrah J E, Parpia M O K and Hupp J T 2006 Dynamics of charge transport and recombination in ZnO nanorod array dye-sensitized solar cells *Phys. Chem. Chem. Phys.* **8** 4655-9

[78]   Nazeeruddin M K, De Angelis F, Fantacci S, Selloni A, Viscardi G, Liska P, Ito S, Bessho T and Gratzel M 2005 Combined experimental and DFT-TDDFT computational study of photoelectrochemical cell ruthenium sensitizers *J. Am. Chem. Soc.* **127** 16835-47

[79]   Nazeeruddin M K, Pechy P, Renouard T, Zakeeruddin S M, Humphry-Baker R, Comte P, Liska P, Cevey L, Costa E, Shklover V, Spiccia L, Deacon G B, Bignozzi C A and Gratzel M 2001 Engineering of efficient panchromatic sensitizers for nanocrystalline TiO_2-based solar cells *J. Am. Chem. Soc.* **123** 1613-24

[80]   Senadeera G K R, Jayaweera P V V, Perera V P S and Tennakone K 2002 Solid-state dye-sensitized photocell based on pentacene as a hole collector *Sol. Energy Mater. Sol. Cells* **73** 103-8

[81]   Jager C, Bilke R, Heim M, Haarer D, Karickal H and Thelakkat M 2001 Hybrid solar cells with novel hole transporting poly (triphenyldiamine)s *Synth. Met.* **121** 1543-4

[82]   Gebeyehu D, Brabec C J, Sariciftci N S, Vangeneugden D, Kiebooms R, Vanderzande D, Kienberger F and Schindler H 2001 Hybrid solar cells based on dye-sensitized nanoporous TiO_2 electrodes and conjugated polymers as hole transport materials *Synth. Met.* **125** 279-87

[83]   Tan S X, Zhai J, Wan M X, Meng Q B, Li Y L, Jiang L and Zhu D B 2004 Influence of small molecules in conducting polyaniline on the photovoltaic properties of solid-state dye-sensitized solar cells *J. Phys. Chem. B* **108** 18693-7

[84]   Saito Y, Kitamura T, Wada Y and Yanagida S 2002 Poly(3,4-ethylenedioxythiophene) as a hole conductor in solid state dye sensitized solar cells *Synth. Met.* **131** 185-7

[85]   Sun D, Sue H J and Miyatake N 2008 Optical properties of ZnO quantum dots in epoxy with controlled dispersion *J. Phys. Chem. C* **112** 16002-10

[86]   Fisher A C, Peter L M, Ponomarev E A, Walker A B and Wijayantha K G U 2000 Intensity dependence of the back reaction and transport of electrons in dye-sensitized nanacrystalline TiO_2 solar cells *J. Phys. Chem. B* **104** 949-58

[87]   Turner G M, Beard M C and Schmuttenmaer C A 2002 Carrier localization and cooling in dye-sensitized nanocrystalline titanium dioxide *J. Phys. Chem. B* **106** 11716-9

[88]   van de Lagemaat J and Frank A J 2001 Nonthermalized electron transport in dye-sensitized nanocrystalline TiO$_2$ films: transient photocurrent and random-walk modeling studies *J. Phys. Chem. B* **105** 11194-205

[89]   Ku C H and Wu J J 2007 Chemical bath deposition of ZnO nanowire-nanoparticle composite electrodes for use in dye-sensitized solar cells *Nanotechnology* **18** 505706

[90]   Yodyingyong S, Zhang Q F, Park K, Dandeneau C S, Zhou X Y, Triampo D and Cao G Z 2010 ZnO nanoparticles and nanowire array hybrid photoanodes for dye-sensitized solar cells *Appl. Phys. Lett.* **96** 073115

[91]   Benkstein K D, Kopidakis N, van de Lagemaat J and Frank A J 2003 Influence of the percolation network geometry on electron transport in dye-sensitized titanium dioxide solar cells *J. Phys. Chem. B* **107** 7759-67

[92]   Jose R, Kumar A, Thavasi V and Ramakrishna S 2008 Conversion efficiency versus sensitizer for electrospun TiO$_2$ nanorod electrodes in dye-sensitized solar cells *Nanotechnology* **19** 424004

[93]   Saunders B R and Turner M L 2008 Nanoparticle-polymer photovoltaic cells *Adv. Colloid Interface Sci.* **138** 1-23

[94]   Hegedus S S and Shafarman W N 2004 Thin-film solar cells: device measurements and analysis *Prog. Photovoltaics* **12** 155-76

[95]   Contreras M A, Ramanathan K, AbuShama J, Hasoon F, Young D L, Egaas B

        and Noufi R 2005 Diode characteristics in state-of-the-art

        ZnO/CdS/Cu(In$_{1-x}$Ga$_x$)Se$_2$ solar cells *Prog. Photovoltaics* **13** 209-16

[96]   Mora-Sero I, Dittrich T, Belaidi A, Garcia-Belmonte G and Bisquert J 2005

        Observation of diffusion and tunneling recombination of dye-photoinjected

        electrons in ultrathin TiO$_2$ layers by surface photovoltage transients *J. Phys.*

        Chem. B **109** 14932-8

[97]   Horiuchi H, Katoh R, Hara K, Yanagida M, Murata S, Arakawa H and Tachiya

        M 2003 Electron injection efficiency from excited N3 into nanocrystalline ZnO

        films: effect of (N3-Zn^{2+}) aggregate formation *J. Phys. Chem. B* **107** 2570-4

[98]   Keis K, Lindgren J, Lindquist S E and Hagfeldt A 2000 Studies of the

        adsorption process of Ru complexes in nanoporous ZnO electrodes *Langmuir*

        16 4688-94

[99]   Westermark K, Rensmo H, Siegbahn H, Keis K, Hagfeldt A, Ojamae L and

        Persson P 2002 PES studies of Ru(dcbpyH$_2$)$_2$(NCS)$_2$ adsorption on

        nanostructured ZnO for solar cell applications *J. Phys. Chem. B* **106** 10102-7

[100]   Yan F P, Huang L H, Zheng J S, Huang J, Lin Z, Huang F and Wei M D 2010

        Effect of surface etching on the efficiency of ZnO-based dye-sensitized solar

        cells *Langmuir* **26** 7153-6

[101]   Hara K, Horiguchi T, Kinoshita T, Sayama K, Sugihara H and Arakawa H

        2000 Highly efficient photon-to-electron conversion with

mercurochrome-sensitized nanoporous oxide semiconductor solar cells *Sol. Energy Mater. Sol. Cells* **64** 115-34

[102]   Kwong C Y, Djurisic A B, Chui P C, Cheng K W and Chan W K 2004 Influence of solvent on film morphology and device performance of poly(3-hexylthiophene): TiO_2 nanocomposite solar cells *Chem. Phys. Lett.* **384** 372-5

[103]   Zhang Q F, Dandeneau C S, Zhou X Y and Cao G Z 2009 ZnO nanostructures for dye-sensitized solar cells *Adv. Mater.* **21** 4087-108

[104]   Lin Y Y, Chu T H, Li S S, Chuang C H, Chang C H, Su W F, Chang C P, Chu M W and Chen C W 2009 Interfacial nanostructuring on the performance of polymer/TiO_2 nanorod bulk heterojunction solar cells *J. Am. Chem. Soc.* **131** 3644-9

VITA

Name:	Tao-Hua Lee
Address:	11F-2. 214, HePing E. Rd., Sec. 1, Taipei City 106, Taiwan
Email Address:	taohualee@gmail.com
Education:	B.S., Mechanical Engineering, Iowa State University, 2005 M.S., Mechanical Engineering, Iowa State University, 2006